R-115

PROJECT LOCOST

(Laser Or Chemical hybrid Orbital Space Transport)

June 19, 1990

VPI & SU Aerospace Senior Design Team

Department of Aerospace and Ocean Engineering
Virginia Polytechnic Institute & State University

Abstract

Project LOCOST

A potential mission in the late 1990s is the servicing of spacecraft assets located in GEO. The Geosynchronous Operations Support Center (GeoShack) will be supported by a space transfer vehicle based at the Space Station (SS). The vehicle will transport cargo between the SS and the GeoShack. A proposed unmanned, Laser Or Chemical hybrid Orbital Space Transfer vehicle (LOCOST) can be used to efficiently transfer cargo between the two orbits.

A preliminary design shows that an unmanned, laser/chemical hybrid vehicle results in the fuel savings needed while still providing fast trip times. The LOCOST vehicle receives a 12 MW laser beam from one earth orbiting, solar pumped, iodide Laser Power Station (LPS). Two Energy Relay Units (ERU) provide laser beam support during periods of line-of-sight blockage by the earth. The baseline mission specifies a 13 day round trip transfer time. The ship's configuration consist of an optical train, one hydrogen laser engine, two chemical engines, a 18 m by 29 m box truss, a mission-flexible payload module, and propellant tanks. Overall vehicle dry mass is 8,000 kg. Outbound cargo mass is 20,000 kg, and inbound cargo mass is 6,000 kg. The baseline mission needs 93,000 kg of propellants to complete the scenario. Fully fueled, outbound mission mass is 121,000 kg.

A regeneratively cooled, single plasma, laser engine design producing a maximum of 768 N of thrust is utilized along with two traditional chemical engines. The laser and chemical engines fire independently, though not simultaneously, to allow the vehicle to make an in-plane spiral trajectory to the desired destination. The chemical engine is primarily used for maneuvers such as plane changes and recircularizations. Collection and transmission of the laser beam to the single laser engine is accomplished via a 14 m diameter, primary collection mirror, a secondary convex parabolic refocusing mirror, two redirection mirrors, and a final, focusing fifth mirror.

The payload module is designed to hold 40,000 kg of cargo, though the baseline mission specifies less. The payload module is supported by a space truss--either the truss or the payload module is capable of detaching independently, adding greater cargo flexibility. The chemical rockets are gimballed about their supports through +/- 7° while the laser rocket is attached to a rocket basket which moves perpendicular to the long axis of the main truss. By moving the rocket basket, the line of thrust can be made to pass thru the instantaneous center of mass.

The maximum cargo mass that can be transferred is 40,000 kg. A 40,000 out/40,000 back cargo transfer scenario is considered. For this scenario, round trip time is 23 days and total propellants used is 220,00 kg.

A proposed design of a laser/chemical hybrid vehicle provides a trip time and propellant efficient means to transport cargo from the SS to a GeoShack. Its unique, hybrid propulsion system provides safety through redundancy, allows baseline missions to be efficiently executed, while still allowing for the possibility of larger cargo transfers.

Preface

This report was prepared by the Virginia Tech aerospace senior design team to fulfill their senior design project requirement (AOE Design 4066). Dr. Jakubowski was the coordinating and guiding faculty member who oversaw the entire project. The team members included

Alan Dixon
Alicia Kost
Gregory Lampshire
Rob Larsen
Bob Monahan
Geoff Wright

Because of the small size of the design group, many subsystems were not fully explored. This report gives details for the key subsystems but only attempts to discuss some specifications and ordinary choices for other subsystems.

Special thanks to Dr. John Costain for letting the group utilize his computer resources, and to Scott Frame for CAD help.

Table of Contents

List of Illustrations

List of Tables

Introduction

Background

One of the NASA goals is to establish a low earth orbiting space station. Establishing this station provides an excellent foothold for further space exploration and industrialization. However, to provide the longterm logistical support for such an endeavor, instruments and equipment will need to be provided to the station in a cost efficient manner. Also, it is likely that a significant amount of scientific and engineering activities performed in the geosynchronous orbit (GEO) will lead to an increase in Low Earth Orbit (LEO) to GEO traffic.

An attractive location to store valuable assets and to service a wide range of spacecraft and platform designs is a depot situated in a geosynchronous orbit. A Geosynchronous Operations Support Center (GeoShack) orbiting at GEO would require less orbit maintenance and provide an ideal storage environment.

To provide logistical support for the GeoShack, it will be necessary to ferry cargo from the Space Station (SS) to the GeoShack. Manned flights will be made, but a large percentage of the cargo can be moved by an unmanned space transfer vehicle.

Project Objectives

Specifically, the project objective is an efficient two-way transfer of cargo between LEO and GEO. By "efficient", it is meant that the mission:

- Minimizes propellant usage
- Minimizes round trip time
- Maximizes cargo mass transfer capability
- Insures adequate safety through redundancy

The type of propulsion for the vehicle greatly influences the characteristics of a mission. The propulsion for an orbital transfer vehicle can be either low thrust or high thrust. Possible high thrust propulsion devices are:

1. Nuclear
2. Chemical

Possible low thrust propulsion devices are:

1. Electrical
2. Laser

The high thrust propulsion devices give quick trip times but require high propellant usage. Low thrust devices provide propellant efficiency but result in long trip times. These two types of propulsion devices have strengths and weaknesses. In order to capture the strengths of each, a *hybrid vehicle* can be designed. This vehicle would exhibit efficient propellant usage due to its low thrust propulsion system. The vehicle would also utilize a high thrust propulsion system which would fire opportunistically to yield shorter trip times than would be possible with a completely low thrust vehicle. The design of a hybrid vehicle presents several design challenges-- many of which will be met with the design presented in this report.

Among the high thrust propulsion devices, only the chemical rocket provides any possibility of utilization. Nuclear propulsion units will not be sufficiently developed for use by the year of technology assumed by this report.

Electric propulsion is conceivable but a large mass penalty is imposed because an electric propulsion vehicle must carry its own electrical power generation equipment. Laser propulsion, however, does not suffer from this drawback. With a laser propulsion unit, a continuously tracked laser power beam is received by the vehicle. The laser beam is converted into thrust by heating a propellant. The propellant heats and expands, then exits a nozzle providing thrust. Laser propulsion has been sufficiently studied so its utilization is feasible.

The hybrid laser-chemical concept does not imply that the two systems are coupled together physically. They are instead used opportunistically whenever one device offers substantial advantages over the other for a given orbital maneuver. The two types of propulsion devices can be fired independently, although not simultaneously.

Basic requirements and assumptions for the LOCOST vehicle are listed in Table 1.

Table 1. Basic Requirements and Assumptions

Orbit Transfer Time	2-3 weeks
Cargo Mass	20,000 - 40,000 kg
Laser Type	Direct Solar Pumped Iodide
Laser Wavelength	~1.315 micrometers
Laser Power	10-12 MW
Isp Chemical Rocket	480 seconds
Isp Laser Rocket	1500 seconds
Level of Technology	2010

It is assumed that the SS is capable of assembling the LOCOST vehicle after it is lifted from earth. It is to be lifted to orbit with no more than four (4) shuttle sized launches. Also, it is assumed that the Laser Power Station (LPS) and the Energy Relay Units (ERU) will be firmly established in their orbits ready for operation.

The single LPS will provide all of the laser power for the LOCOST vehicle during the duration of a mission. There are two ERUs; one each positioned 120° lead and 120° lag. The vehicle can operate without the ERUs, but the ERUs provide a substantial improvement in propellant usage and trip time if used because they eliminate the line-of-sight problem between the vehicle and the LPS (see "Orbital Mechanics" on page 17).

The General Mission Scenario

The general mission begins in LEO plane with orbital inclination of 28.6°. It is assumed that a cargo booster or the space shuttle has lifted a payload from earth, or that the space station has payload intended for GEO. The cargo will be transported to the GeoShack. The outbound mission will assume a cargo mass of 20,000 kg. The LOCOST vehicle loads the cargo and initiates an outbound, spiral trajectory characteristic of a low thrust propulsion device. The laser rocket will be the only propulsion device in operation during the entire orbit transfer. Once the orbit transfer is complete, the vehicle will recircularize using the chemical rocket at GEO, then instigate a plane change. The plane change will use the chemical rocket. The plane change is performed at GEO because the ΔV requirement for the vehicle will be smaller than that needed at LEO, realizing significant propellant savings. After docking with the GeoShack and depositing the payload,

the vehicle will reload with 6,000 kg of cargo. The vehicle will initiate another plane change, followed by the orbit transfer, and finally end the trip with another recircularization at LEO.

As mentioned in the scenario above, the outbound cargo is half the maximum the LOCOST vehicle is designed to handle. It is important to analyze the scenario where the maximum cargo out and back is transported. As seen in the trajectroy analysis chapter, this mission scenario requires a modification of the truss to accomodate the propellant increase.

Redundancy of the Propulsion System

Because of the redundant propulsion system, the LOCOST vehicle can suffer the loss of one type of propulsion device and still complete the mission. For example, it is conceivable that the LPS, which is susceptible to failure from dangers that the vehicle might not experience, could fail during the mission. The loss of access to the LPS will cause the vehicle's laser propulsion to become useless. At this point, the chemical propulsion can activate and provide a safe return trip. The ability to recall the vehicle in the event of a single propulsion failure is important when the payload *must* be recovered within a given time constraint.

The redundant propulsion system increases the reliability. Although a reliability analysis is beyond the scope of this report, it is clear that the hybrid vehicle is more reliable than a vehicle with a single type of propulsion.

Extended Mission Capability

A hybrid vehicle provides extended mission capability. There are certain missions that a dedicated propulsion device vehicle can perform with better performance than a hybrid vehicle. If there are no time constraints on the completion of a payload transfer, a completely low thrust vehicle can perform the mission with greater propellant efficiency. If, however, the payload transfer time is critical, a high thrust propulsion device is best suited for the transfer.

Vehicle Configuration

This section describes the overall LOCOST vehicle configuration. It also presents a design rationale, a short description of the configuration evolution, and a configuration component summary.

Design Rationale

The design of an aerospace vehicle must consider the traditional design criteria. Special features of a vehicle merit additional study. Traditional design criteria are listed below.

- Low mass
- Low moments of inertia
- Simplicity in design
- Ease of integration of configuration components
- Efficiency in execution of mission
- Reliability

The above criteria must be balanced by a vehicle's special needs. For example, a technologically advanced propulsion system can increase the vehicle mass and increase the complexity of design. These concerns are balanced by the increase in overall performance of the vehicle. The advanced propulsion system could also reduce overall propellant consumption making the previous objections moot. Such is the case with the LOCOST vehicle.

The components of the vehicle which will provide the greatest design challenge are also the components which bend the traditional design criteria. Because the final design will contain both a laser propulsion device and a chemical propulsion device, several issues arise. These issues are summarized in Table 2.

Table 2. Important Design Issues for the LOCOST Vehicle

- Placement of the laser engines
- Placement of the chemical engines
- Elimination of the interference between the two systems
- Collection of the laser beam for rocket use
- Line of thrust through the center of mass
- Placement of the cargo
- Placement of the fuel tanks

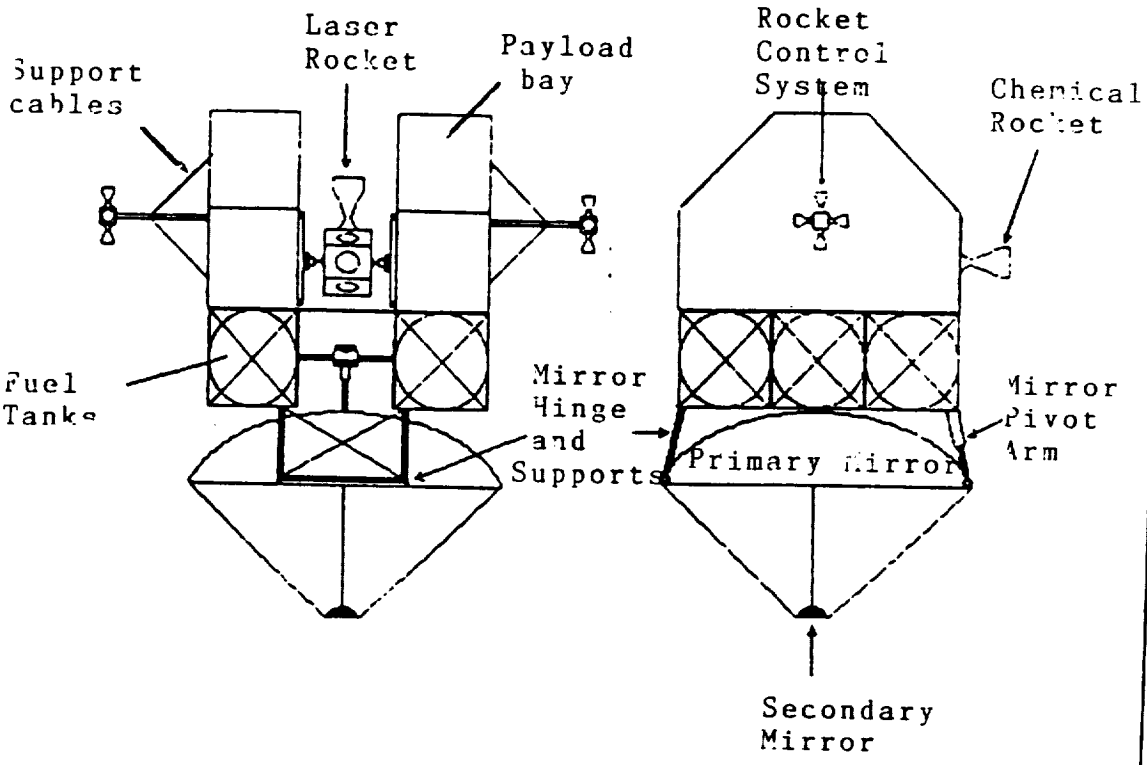

Figure 1. Configuration 1

Configuration Evolution

Configuration 1

This configuration can be viewed in Figure 1. It featured one laser rocket and one chemical rocket in a symmetrical design. The laser rocket engine housing was composed of a multi-faceted lens. This allowed the laser rocket to rotate through various angles but still capture the incident power beam. Propellant storage was accomplished through six spherical tanks located near the primary mirror. The primary mirror could rotate about a hinge support by extending a pivot arm. This design was rejected for two reasons. First, there was not sufficient evidence that a multi facetted lens configuration on the laser rocket housing would support the high incident power transfers. Second, as the propellant tanks reduced their mass through propellant consumption, the center of mass changes. The fixed position of the laser rocket did not allow for any variation of the line-of-thrust.

Configuration 2

The second configuration featured a large rectangular space truss and a non-symmetrical placement of the primary dish. The primary mirror was mounted on top of the truss with two retractable poles. Movement of the poles away or towards the main truss moved the primary mirror. The

mirror was also mounted on two gimbals which allowed the mirror to rotate. Two chemical rockets were mounted symmetrically about the longitudinal axis of symmetry while a single laser engine was mounted through the center. The most notable feature of this design was that the laser and chemical rockets were mounted in a rocket basket. The entire rocket basket moved to compensate for the change in the center of mass. The laser rocket face was changed to a plano-convex lens. A multi-facet design was not needed.

This design was rejected for two reasons. First, the movement of the rocket basket (containing all three rockets) was deemed inefficient and unnecessary. Second, the motion of the primary mirror created innumerable difficulties with designing an optical system capable of transmitting the beam to the laser rocket housing.

Selected Configuration

The selected configuration eliminated many of the problems associated with configuration 2. The primary mirror is fixed and the chemical rockets are gimballed. The laser rocket, however, continues to move in a rocket basket for reasons which will be discussed. Figure 2, Figure 3, and Figure 4 show the selected configuration for the LOCOST vehicle.

Discussion of the Selected Configuration

The following sections will discuss the main components of the selected configuration. Figure 2 and Figure 3 point out the main features of the final configuration.

Main Truss

The main truss is 29.11 m in length, 6.3 m deep, and 18.9 m wide. It is a rectangular frame and it is constructed with 6.3 m truss boxes. The mirror support structure extends 9.0 m up from the top plane of the vehicle. Individual truss members range in length from under 1.0 meters to over 9.0 meters. The struts are made from graphite epoxy with a cylindrical shell design. The outer diameters are 5.4 cm and they have a wall thickness of 0.16 cm. The members are assembled using titanium joint fittings. The total dry-mass which excludes all components except the struts and nodes is 1730 kg.

Propulsion

Chemical Propulsion

A bi-propellant chemical rocket is used with hydrogen as the fuel and oxygen as the oxidizer. The final configuration uses two rockets. Each chemical rocket is capable of delivering 25,000 N of thrust. A rocket analysis program NOTS was used to calculate the flow in the chamber, throat and nozzle. The rocket has an area ratio of 800 and a throat diameter of .04 m. The rocket has a chamber pressure of 10 MPa and a mixture of 6:1. The maximum temperature occurs in the throat--3380 K. The rocket was designed to have a specific impulse of 480 seconds. The chemical rockets are regeneratively cooled with hydrogen fuel. Each rocket has a mass of 427 kg.

Laser Propulsion

The laser energy will be coupled to the thermal energy of the hydrogen propellant via the inverse Bremsstrahlung process. Particulate absorption by carbon particles will be used to initiate the plasma upon which the inverse Bremsstrahlung process will operate. The laser engine is 56 cm in diameter and 1.25 m long. It will consist of a plano-convex sapphire window lens which will converge the laser beam within the engine chamber. Another main feature of the laser engine is the mounting collar that allows the engine to be mounted inside the mobile rocket basket by graphite-epoxy struts.

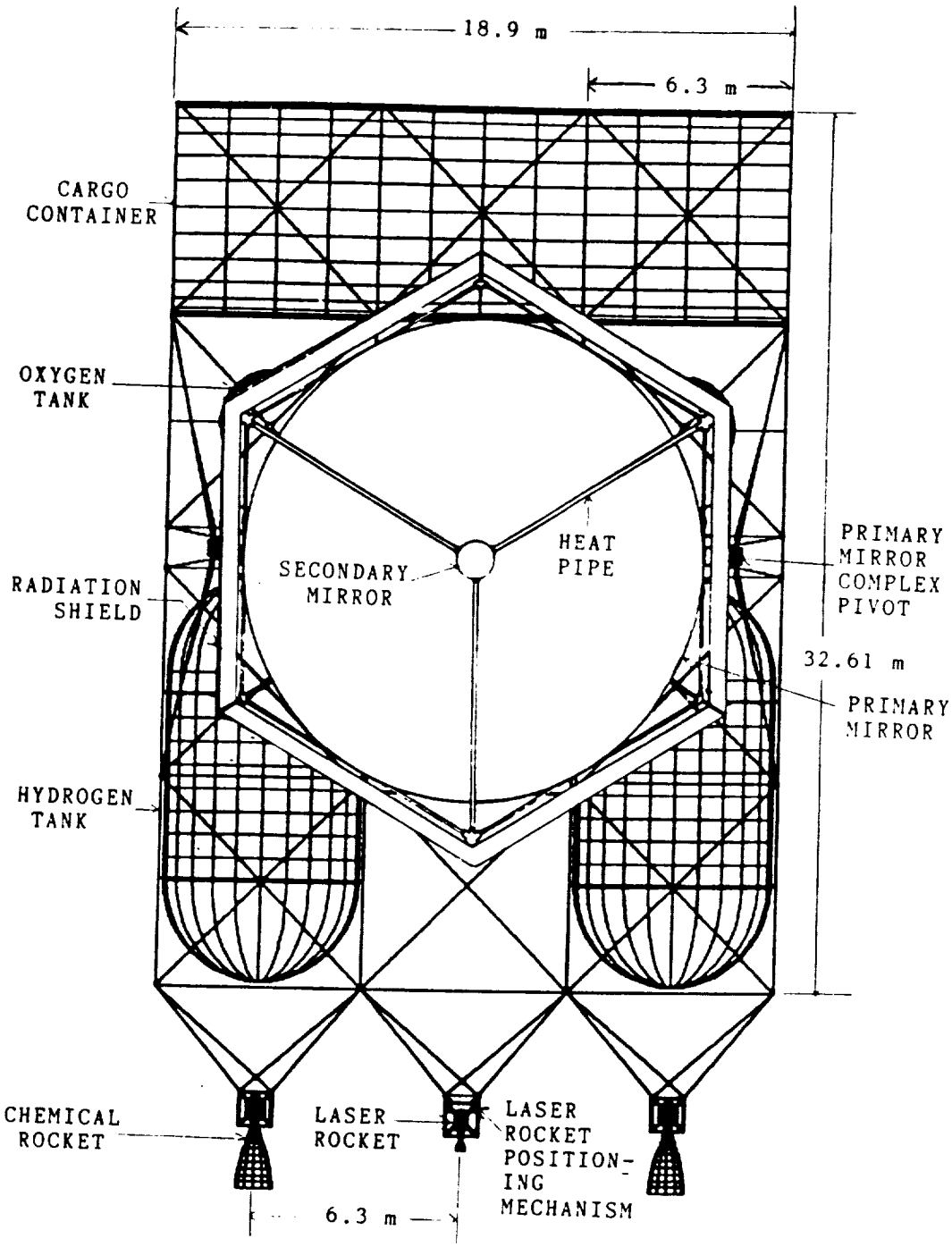

Figure 2. Selected Configuration–Top View

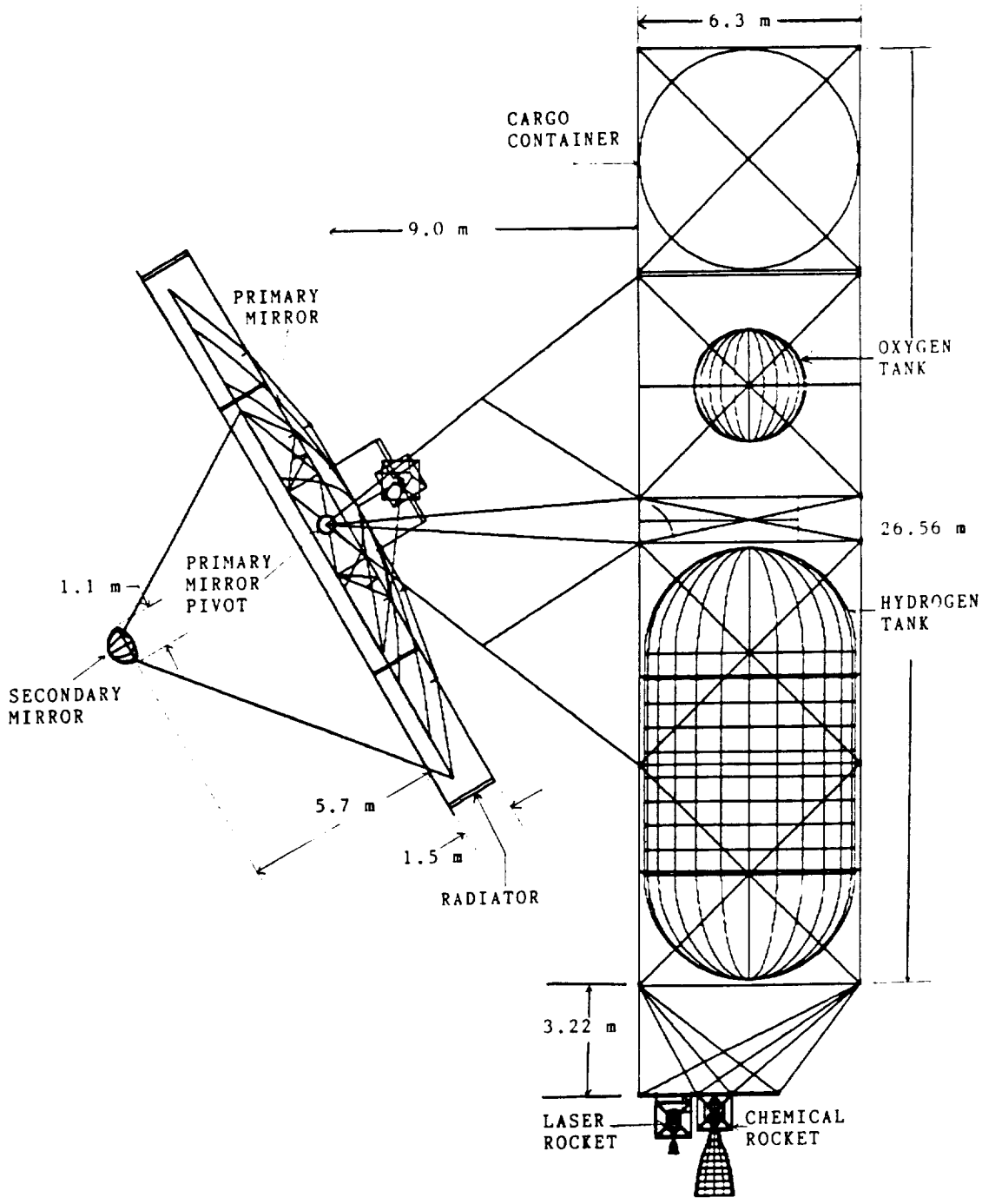

Figure 3. Selected Configuration–Side View

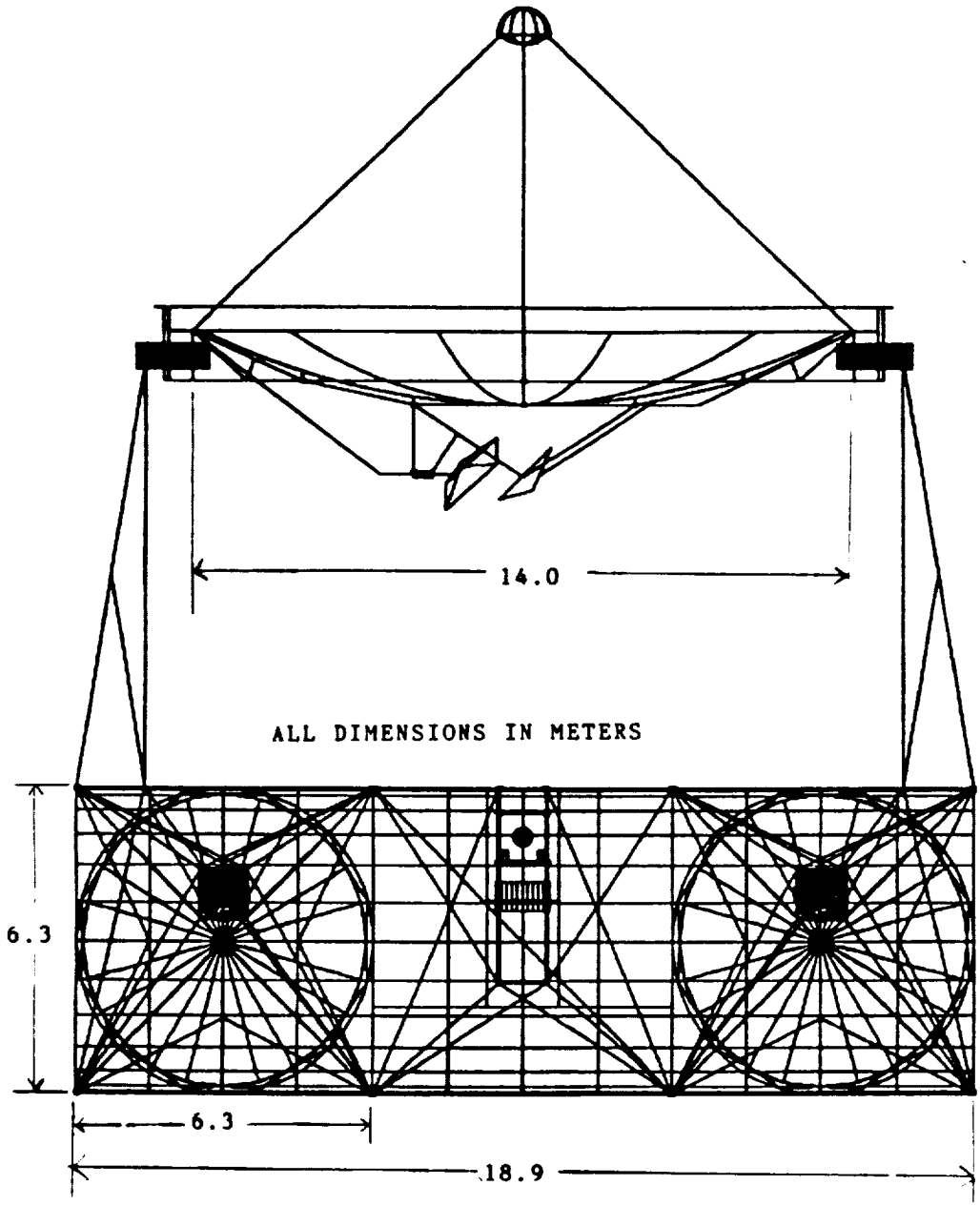

Figure 4. Selected Configuration–Rear View

The rocket basket moves to adjust the line-of-thrust so that it always passes through the center of mass. The laser rocket is situated along the longitudinal plane of symmetry of the vehicle.

Propellant Storage

The oxidizer is stored in two spherical tanks and the hydrogen fuel is stored in two cylindrical tanks. The tanks are symmetrically placed.

The tank skins are made out of an aluminum alloy. The mass of the tank skins are 6 and 129 kg respectively for the liquid oxygen and the liquid hydrogen. Internal pressure is maintained at 35 kPa. The tank interior supports slosh baffles and a "flow channel" type liquid acquisition device. The tanks are covered with two types of insulation. Thin, alternating layers of metallized Kapton film and Dacron net spacers (MLI) are used and an outer coating of Rohacell 31 foam is applied. A thin layer of reflective paint, YB-71, is applied to the foam. The mass of the insulation for each type of tank is 47 and 571 kg respectively for the liquid oxygen and hydrogen tanks.

Optical System

The optical system is composed of five mirrors, a cooling system and an opto-electronic feedback system. The optical system will be described in detail in a later chapter. The following discussion offers an overview of the optical system components.

Optical Train

The optical train is composed of five mirrors: a primary mirror, a secondary mirror, a third and fourth mirror, and a final fifth mirror. The purpose of these mirrors is to collect the incident laser beam and direct it to the laser rocket. The mirrors are labelled in the order that they are used. The primary mirror is the largest mirror, 14 m diameter, and collects the beam slightly off-center. The primary mirror is mounted on two gimbals. These gimbals allow the mirror to rotate. The primary mirror focuses the beam to the secondary mirror. The secondary mirror colimates the beam (to a diameter of 1.1 m) and directs the beam towards a hole in the primary mirror. After passing through this hole, the beam strikes a fixed elliptical third mirror and immediately reflects the beam onto a fourth mirror. The fourth mirror can rotate about its axis. This feature gives the primary mirror the ability to swivel about its gimbals and still direct the beam to the laser rocket. After striking the fourth mirror, the beam strikes the fifth mirror. The fifth mirror moves along a track in concert with the rocket basket.

The secondary, third, fourth, and fifth mirrors require cooling due to the intensity of the power beam. The primary mirror has a low incident intensity therefore does not require cooling. The secondary, third, and fourth mirrors are cooled using a heat-pipe system. The heat pipes connect to a primary radiator located around the edge of the primary mirror behind a radiation shield. The fifth mirror is cooled with hydrogen fuel during operation of the laser rocket.

Opto-Electronic Feedback System

Continuous, precise alignment of the optical train during powered flight is difficult to achieve. An opto-electronic feedback system has been designed to fine tune the optical system. The system is primarily composed of a laser tracking communications system and optical feedback sensors. The laser tracking communications system, dubbed the ATP (Acquisition, Tracking and Pointing system), uses a lasercom-like system to continuously track the incident laser beam. The lasercom equipment is mounted on a boom located at one of the gimbal mounts of the primary mirror. A laser system must be used in order to achieve precision tracking.

Avalanche photodiodes (APD) with dielectric filters have been placed around the periphery of most components of the optical train. These APDs provide the feedback sensor capability required for the close-looped system.

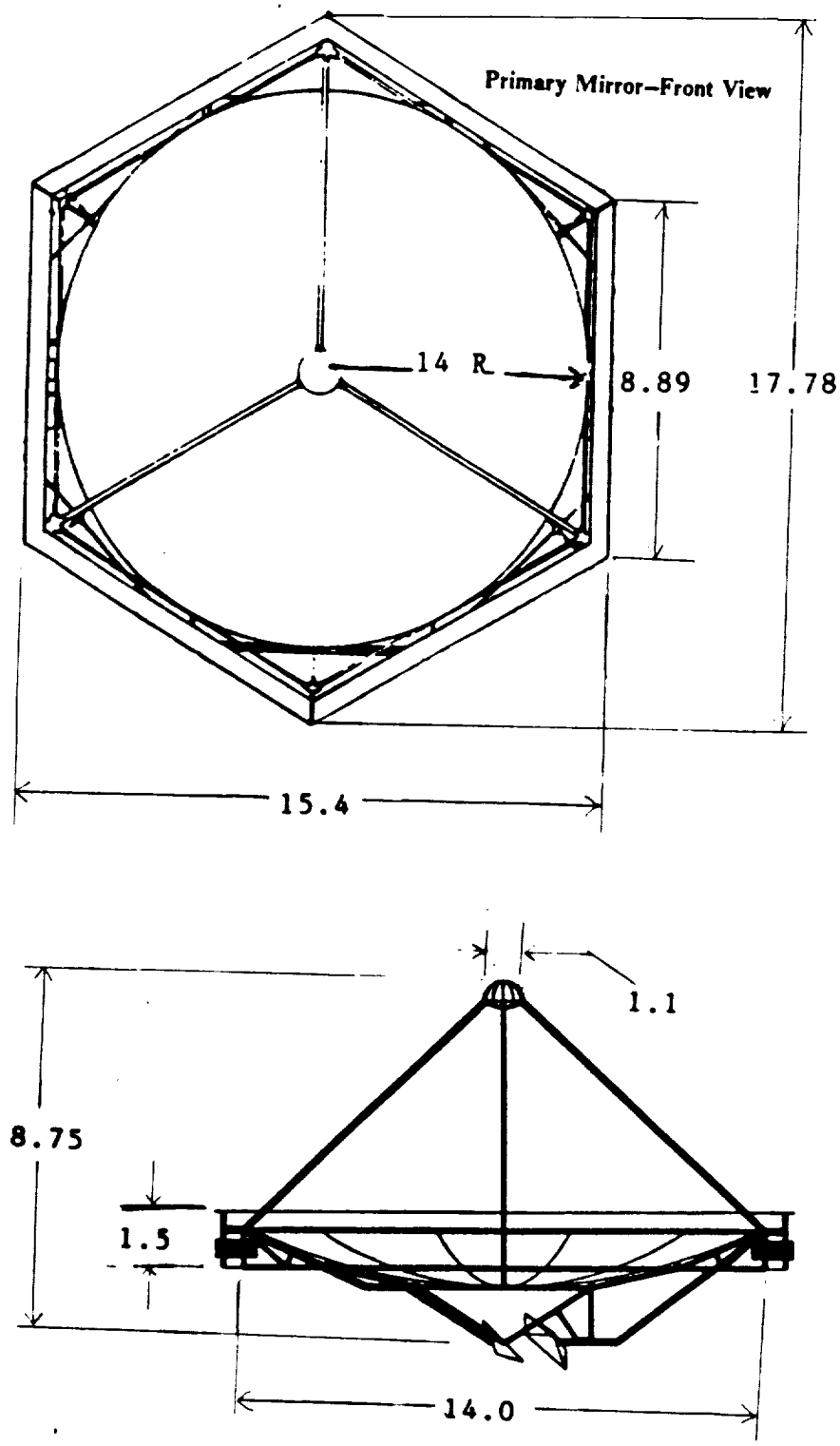

Figure 5. Primary Collection Dish-Side View

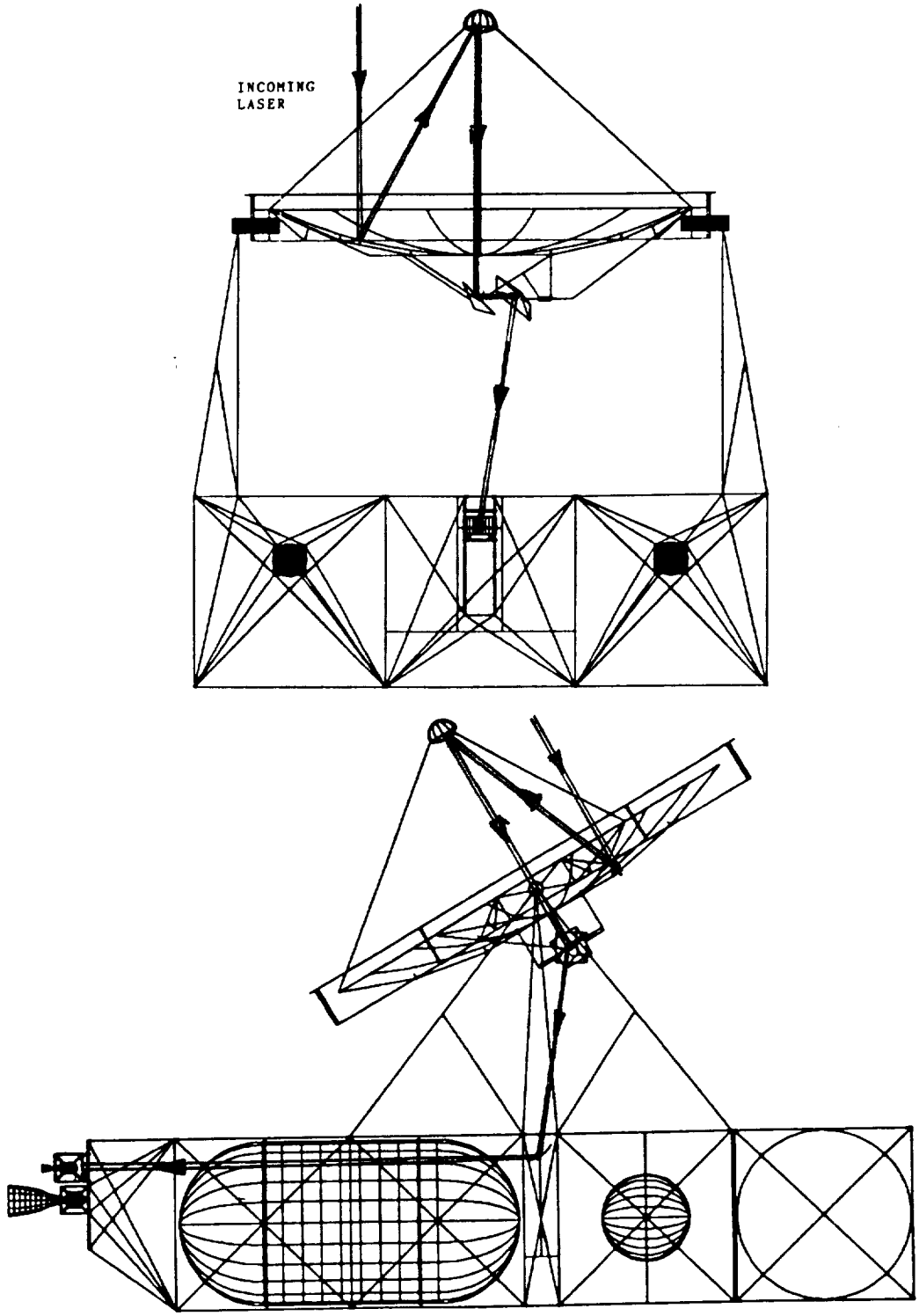

Figure 6. Incident Laser Beam Path

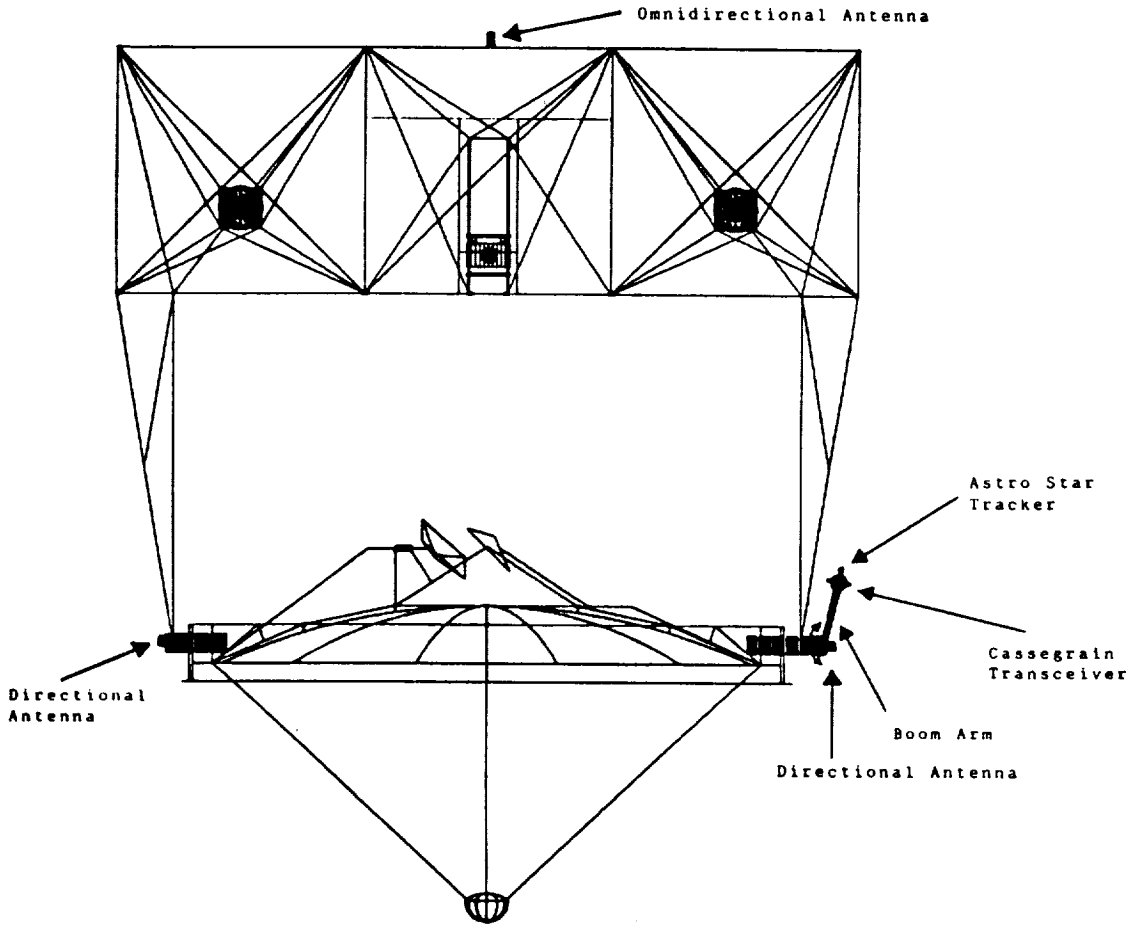

Figure 7. Location of LaserCom Equipment

Payload Module

The payload module is composed of a magnesium alloy cylinder which holds the payload during the duration of the trip and a supporting space truss. The payload module is mission flexible. Either the payload canister or the space truss may detach from the main truss. Special node connectors were designed to allow the space truss to snap together. This makes removing the payload truss simple, and allows for tele-robotic operators to remove the payload at the GeoShack. The mass of the entire payload module, including the space truss is 1550 kg.

Attitude Control

Attitude control is partially accomplished by four advanced control moment gyroscopes (CMG). Attitude determination is achieved by fiber optic gyroscopes and charge-coupled star trackers.

Rocket Control System (RCS)

The rocket control system is used for desaturization of the CMGs, attitude and docking maneuvers. The RCS system is composed of eight sets of three nozzles located at the corners of the main truss.

The RCS rockets are hydrazine/oxygen powered chemical rockets. Storage of the hydrazine will be accomplished by locating small tanks near each RCS cluster. The mass for the total system is 1600 kg.

Communications System

The communications system is used for telemetry, control, and data acquisition. The main communications system uses a RF wavelength transmitter and receiver. One omni-directional antenna and two directional antennas are required to start the power beam acquisition sequence. The mass of the total system is 200 kg.

Electrical Power

Electrical power is provided by fuel cells which use oxygen and hydrogen in a chemical reaction to produce electrical energy. The oxygen/hydrogen fuel scheme was selected because of the availability of those elements aboard the LOCOST vehicle. The power system is composed of four fuel cells. Each fuel cell has a mass of 100 kg. The undesirable by-product of the fuel cell chemical reaction, water, will be vented into space.

Configuration Analysis and Mass Breakdown

Table 3 summarizes the mass breakdown for a vehicle satisfying the baseline mission.

Table 3. Mass Breakdown

	Kgs
Structures	
Main truss	423
Total	423
Propulsion	
Chemical rockets	422
Fuel Lines (Chemical)	150
Chemical mounting	4
Laser Rocket	75
Fuel Lines	75
Total	726
Optical System	
Primary mirror	2,075
Support for primary	35
Secondary mirror	90
Mirrors 3,4,5	300
Total	2,522
RCSs & CMGs	1,100
Docking	50
Communications	110
Payload Module	1,100
Vehicle Dry Mass	6,682
Outbound (with cargo)	26,605
Inbound (with cargo)	12,605
Propellant usage for baseline mission.	
Propellant	
O_2	38,300
H_2	53,928
Total	92,228
Outbound Total	118,833

Table 4 presents key characteristics of the propulsion system.

Table 4. Main Engines

Laser Rocket
- Isp 1500 seconds
- T_{max} 768 N
- $mdot_{max}$ .0522 kg/s

Chemical Rocket
- Isp 480 seconds
- T_{max} 25,000 N per engine
- $mdot_{max}$ 5.2 kg/s per engine

Table 5 summarizes the CG location for different conditions.

Table 5. Center of Mass Locations

Condition	x (m)	y (m)	z (m)
No payload, No propellant	13.44	9.45	11.05
No payload, Full propellant	10.85	9.45	3.467
6,000 cargo, No propellant	19.44	9.45	6.24
20,000 cargo, Full propellant	13.00	9.45	3.413
40,000 cargo, Full propellant	14.4	9.45	3.37

Orbital Mechanics

Introduction

Program OM was developed to evaluate different trajectories that involve space vehicles with two disparate, primary types of propulsion. In this chapter, the evaluation of the baseline mission and an evaluation of the maximum cargo trajectories will be discussed.

Mission Assumptions

The LOCOST vehicle will rendezvous with the space station (orbital inclination of 28.6°), then transport the cargo to a GeoShack or a satellite cargo depot at GEO (0° inclination). The baseline mission assumes two Energy Relay Units (ERU), but a non-ERU mission will also be considered.

One laser station cannot provide continuous power to the vehicle because of, station-solar occultation and earth blockage (Figure 8).

Station-solar occultation occurs for 16.7 % of the laser station orbit. Earth blockage times are dependent on the specific trajectory and thrusting rules. A large percentage of the LOCOST vehicle in-flight time is spent on coasting.

Earth blockage occurs when

$$R < \frac{R_{earth}}{(\sin 150° - \delta)}$$

where δ equals the angular separation of the LPS and the LOCOST vehicle. ERUs are orbiting platforms that relay the power beam around the earth horizon. In order to completely eliminate the earth blockage problem, two ERUs are needed. Each ERU is located in the plane of the LPS. One ERU is positioned 120° behind the LPS and another 120° ahead.

Most low-thrust propulsion devices are power limited, and hence, when the mision requirements force the vehicle to conform to specific constraints, power-limited propulsion techniques must be supplemented by other more powerful, high thrust devices. The purpose of this section is to explain the strengths of a laser/chemical hybrid, how the hybrid vehicle utilizes the strengths of both types of propulsion devices and to justify the hybrid's strength based on mission analysis.

Program OM

Program OM was developed to analyze the trajectory of a vehicle with more than one type of propulsion device. The effects of earth blockage, station-solar occultation, and ERU placement were coded in the form of firing rules. A mission scenario can be analyzed by linking together several flight modules, each of which was given a special maneuver number. Information about payload mass and propellant starting parameters was obtained from an input file. A second input file described instantaneous orbit sampling parameters and other run parameters which helped fine tune the numerical routines.

Program OM used functions from the IMSL library to integrate the equations of motion. A figure giving some of the geometrical parameters is pictured in Figure 9. From this figure, equations of

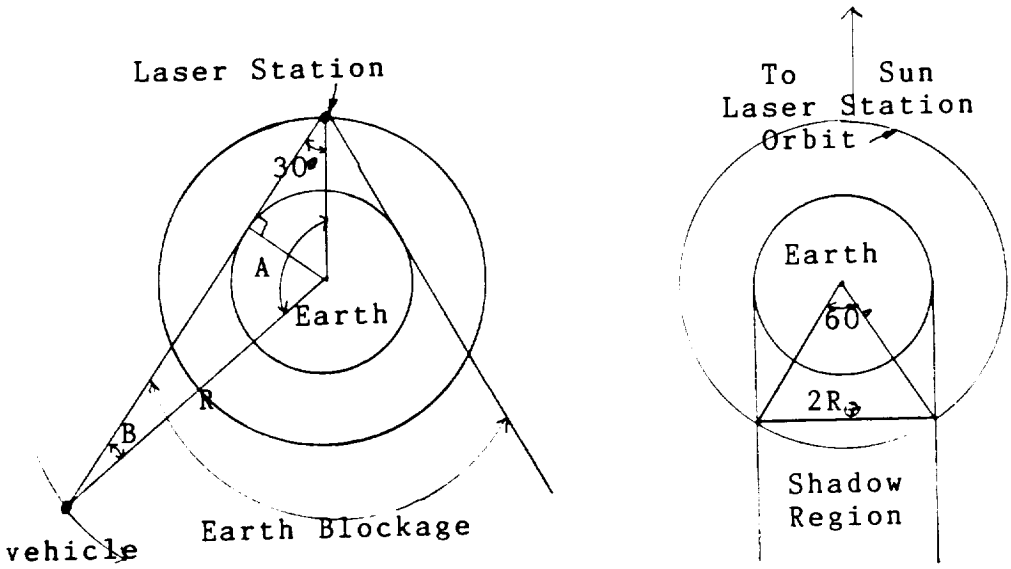

Figure 8. Station-solar Occultation and Earth Blockage

motion were developed. Additional equations of motion were added to the set for the LPS and the ERUs.

$$\dot{\theta} = \frac{v \cos \gamma}{r}$$

$$\dot{r} = v \sin \gamma$$

$$\dot{v} = \frac{T \cos \beta}{m} - \frac{\mu \sin \gamma}{r^2}$$

$$\dot{\gamma} = \frac{T \sin \beta}{mv} - \frac{\cos \gamma}{v}(v^{2/r} - \mu/r^2)$$

Where

Theta is the orbit path increment angle
v is the velocity vector
γ is the angle between the local horizontal and velocity vector

r is the radius vector
T is the thrust vector
β is the angle between the thrust and velocity vector
m is the mass of the orbiting object

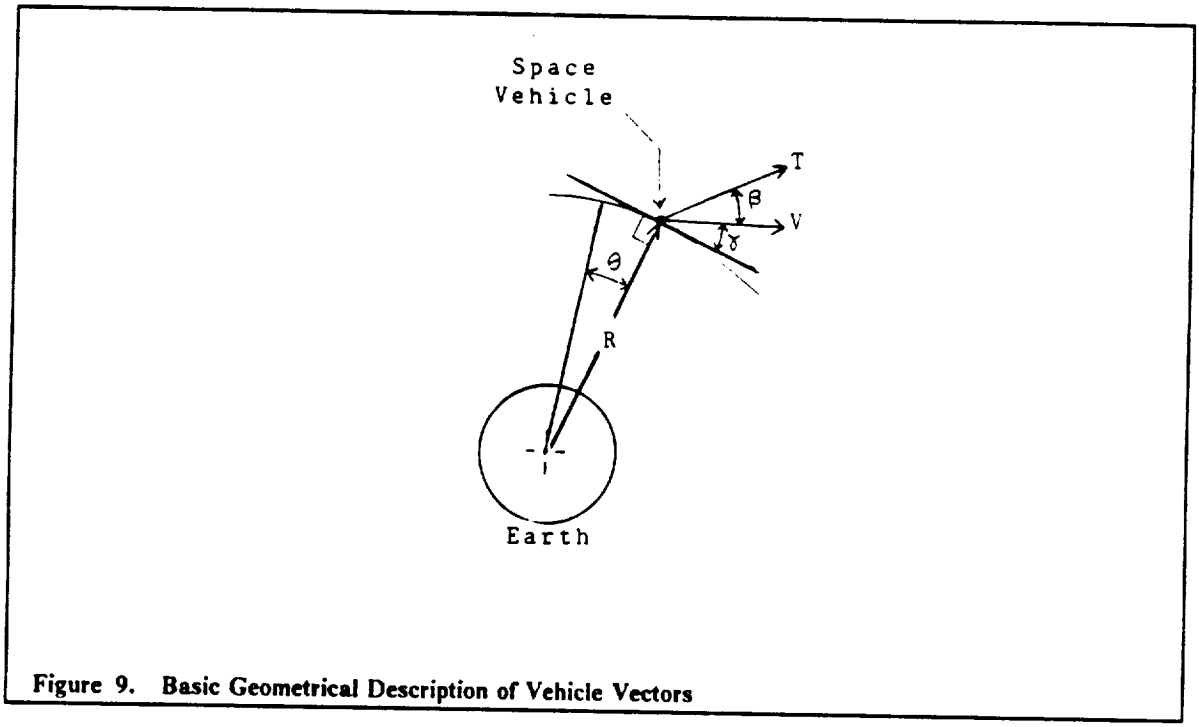

Figure 9. Basic Geometrical Description of Vehicle Vectors

A Runge-Kutta sixth order method was used to integrate the equations used in program OM. Subroutine IVPRT from the IMSL library was used. The time step used for this integration was part of an input file. Runs were made with time steps and sampling parameters on the order of 30 seconds to 10 minutes.

Output was collected in several files. Separate output files for plotting, sampling, logging and maneuver statistics were generated.

Station Solar Occultation.

Figure 8 shows station solar occultation. Station solar occultation is a function of the LPS's angular velocity and the starting position of the LPS. The occultation figure shows the range of angles, for the orbiting altitude of the LPS, that the sun can reach the LPS. From the simple relation

$$\theta_{LPS} = \theta_o + \omega_{LPS} t$$

it can be shown that the LPS is in the earth's shadow 16.67% of any trip TOF.

Because it is assumed that there is only one LPS, when station solar occultation occurs, it is impossible to fire the laser. During these times, the vehicle coasts.

The Baseline Mission

Table 6 shows some additional assumptions that were used when performing the trajectory analysis.

Table 6. Baseline Mission Assumptions

- Two ERU's are used, therefore, only sun occultation will prevent laser usage.
- Laser propulsion is used only for orbit transfers.
- Chemical propulsion is used only for recircularization and plane changes.
- The outbound cargo is 20,000 kg.
- The return cargo is 6,000 kg.

Using these assumptions, the baseline scenario was computed. It is presented in Table 7.

Table 7. Baseline Scenario Trajectory Analysis Results

Flight Segment	ΔV (km/s)	Time (days)	Propellant Used (kg)
Transfer	5.16	9.63	36,393
Recirc.	.00575	0.0011	1,018
Plane Ch.	1.52	0.025	22,879
Plane Ch.	1.52	0.0014	12,707
Transfer	3.17	1.74	6,522
Recirc.	1.52	0.008	7,414

Total Time 11.4 + 0.6 (Cargo Transfer) = 12 days
Total Propellant's Used 87,221 kg

Laser Propellant 43,202 kg
Chemical Propellant 44,020 kg

For a 6:1 oxidation ratio

LO2 propellant 38,310 kg
LH2 propellant 54,000 kg

Maximum acceleration .1 g's

Thrusting Times
Laser 83%
Chemical .4%
Coasting 17%

Residual Fuel ≃3,255 kg (3.5% residual)

A noticeable feature about the baseline scenario is the coasting time. The coasting time in this scenario is the lowest for all cases calculated. This figure indicates that the LPS was completely utilized. If the traffic between LEO and GEO increases, more vehicles will be needed or less power per vehicle and longer coasting times will result. This report assumes one dedicated LPS.

Table 8 shows various mass ratios characteristic of the vehicle.

Table 8. Mass Ratios

$\frac{payload}{propellant}$	0.28
$\frac{propellant}{vehicledrymass}$	11.6
$\frac{propellant}{1 - mass}$	0.92

The Maximum Cargo Scenario

The maximum cargo scenario involves moving the maximum amount of cargo to GEO and back. The cargo would be 40,000 kg out/ 40,000 kg back. It assumes two ERUs are in use.

Using program OM to analyze this scenario produces some interesting results. In order to move the maximum amount of cargo in the manner described, the TOF increases as well as the propellant consumption. Table 9 summarizes the extreme case.

Table 9. The Maximum Cargo Scenario—40,000 kg Out and Back

Total Trip Time	24 days (13 out/11 in)
Total Propellant Used	225,000 kg
Residual 3.5%	

Performance ratios are presented in Table 10.

Table 10. Maximum Cargo Scenario—Performance Ratios

propellant/LOCOST dry mass = 28.1

total payload/propellant = .36

Even though the trip time doubled, the amount of propellant needed for given unit mass was lower for the baseline scenario. The maximum cargo scenario provides better propellant efficiency at a cost of time flexibility.

In order to accommodate the extra propellant, tanks must be added to the LOCOST vehicle. The tanks attach towards the rear of the vehicle, and are placed in unit cells on the outer edges of the truss. The section on structures will give specifics.

Other Scenarios

To understand the effect that the ERU usage assumption has on trip time and propellant consumption, another scenario was computed. In this scenario, whenever station solar occultation occurrs, the chemical rocket is fired for ten minutes at 50% maximum thrust. Total propellants

consumed jump to 275,000 kg and trip time increases dramatically to 32 days. Payload loads are maximum.

While it takes 34 times the vehicle's dry mass in propellant to move the 80,000 kg total of payload, the payload over propellant ratio remains nearly the same as that for the baseline mission, in this case 0.29.

Conclusions

It was found that the assumption that there are ERUs in use can lead to significant time savings over a non-ERU scenario. While the ERUs do not provide drastically superior payload to propellant ratios, the ERU assumption introduces greater mission flexibility in the form of scheduling and diversity of payload transfer. The existence of ERUs is critical to the longterm logistical support of a SS or GeoShack dependent on laser based vehicles. It is suggested that ERUs be included in any such endeavors.

From the trajectory analysis, it is apparent that a 40,000 kg cargo presents difficulties for low-thrust vehicles. While the average mission can expect to carry masses at most half that size, the capability for the maximum cargo case should exist. A low-thrust all laser vehicle cannot provide the support for the extreme case. For the baseline case, the LOCOST vehicle yields significant savings in propellant usage, but not as good as an all laser vehicle. The vehicle provides, however, better time performance.

Optical System

The optical system provides a direct link between the power source and the laser engine. The objective of the optical system is to intercept the laser beam and redirect and focus the beam into the thrust chamber for any vehicle attitude orientation.

Optical System Evolution

The main goal of the optical system is to capture and direct the laser beam into the laser rocket chamber. A two laser rocket design was first proposed. Although it allowed for a symmetrical system it necessitated the use of a beam splitter and a larger primary mirror. The large increase in mass of the primary mirror and that the beam splitter may not be able to split the beam exactly (to provide equal power to the engines) motivated the search for other designs. The final design described below incorporates a one degree of freedom primary mirror and one laser engine.

The primary mirror was limited to designs which provided a very high reflectivity. This eliminated an inflatable mirror which, although light and easy to deploy, does not have high reflectivities. A polished metal mirror was investigated, but it, too, cannot achieve a desired reflectivity of over 99.0%. Finally, a dielectrically coated mirror was selected. This type of mirror offers very high reflectivity along with relatively low mass. Also the dielectrics can be applied to the substrate material on earth and then assembled in space.

Optical Train Geometry

The selected optical train geometry is shown in Figure 10 and Figure 11. Figure 10 shows the primary mirror assembly from a side view, while Figure 6 shows the path of the laser beam from the rear and side of the vehicle.

The optical system employed for the vehicle is similar to a true Cassegrain system. A small (r = .55 m) convex parabolic mirror is mounted on tripod legs extending from the large (r = 7m) concave parabolic mirror. The main mirror was sized to capture the beam at the maximum working distance of the vehicle. The beam size at a given distance is a function of the diffraction limited half angle, beam jitter, wave front error, and the separation distance.

$$S = \sqrt{(1.3S_d)^2 + (S_j)^2 + (S_w)^2}$$

Where

S is the divergence in radians
S_d is .4138 λ/D (diffraction limited half angle)
S_j is 0.05×10^{-6} (beam jitter)
S_w = λ/20 D (wave front error)
λ is 1.315 micrometers (wavelength)
D = 30 m (transmitting mirror diameter)

The spot size of the beam is found using the following relation

$$D = 4S \times R$$

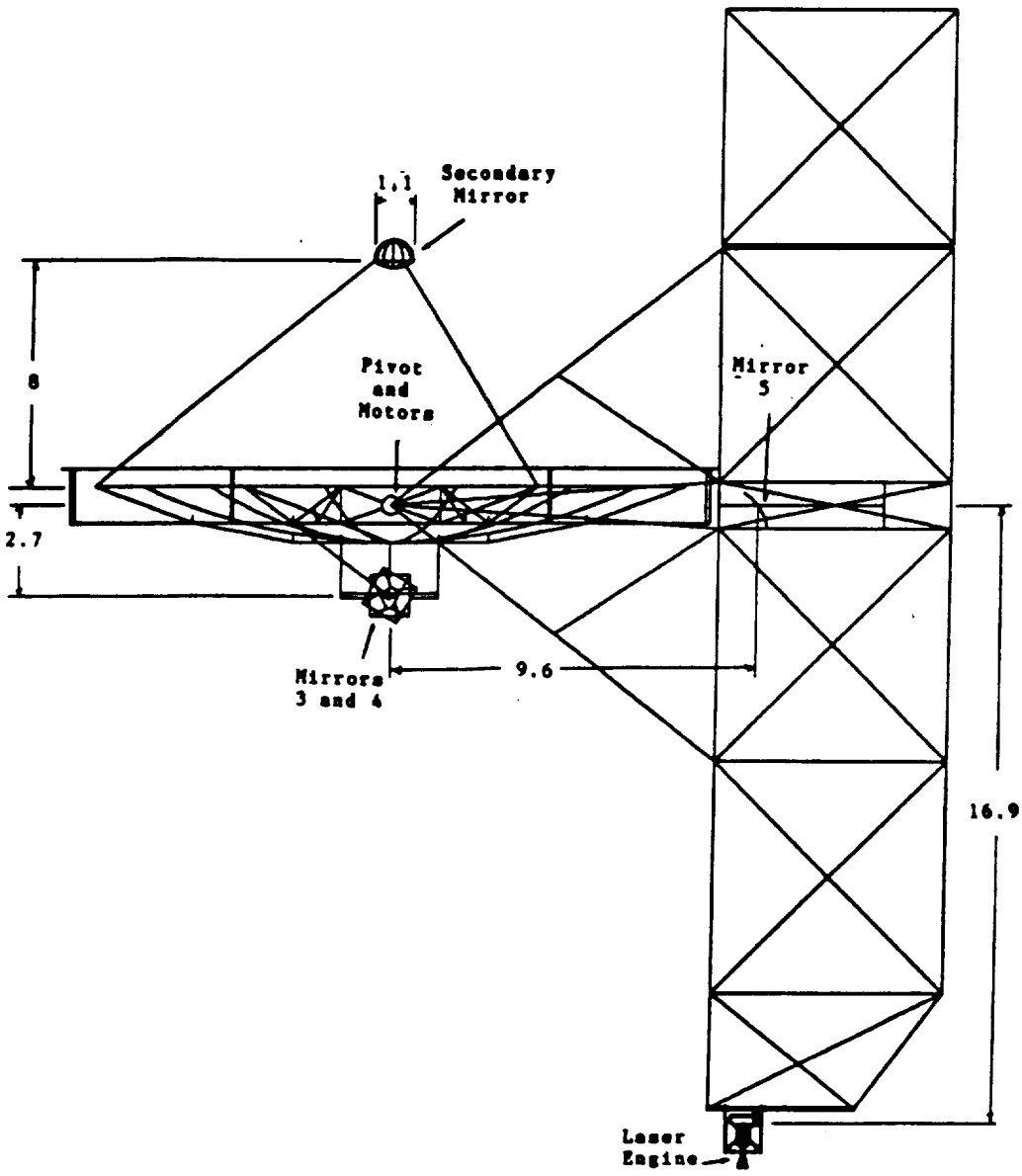

Figure 10. Optical System Configuration Side View

Where R = 52,300 km, the maximum separation distance. The spot diameter was determined to be 11.6 meters. The primary mirror was sized up to a diameter of 14 meters to allow for off-center capture of the beam (to reduce heating load on the secondary mirror housing) and to capture fringes of the laser beam. This adds to the power captured and reduces radiation degredation on the vehicle structure.

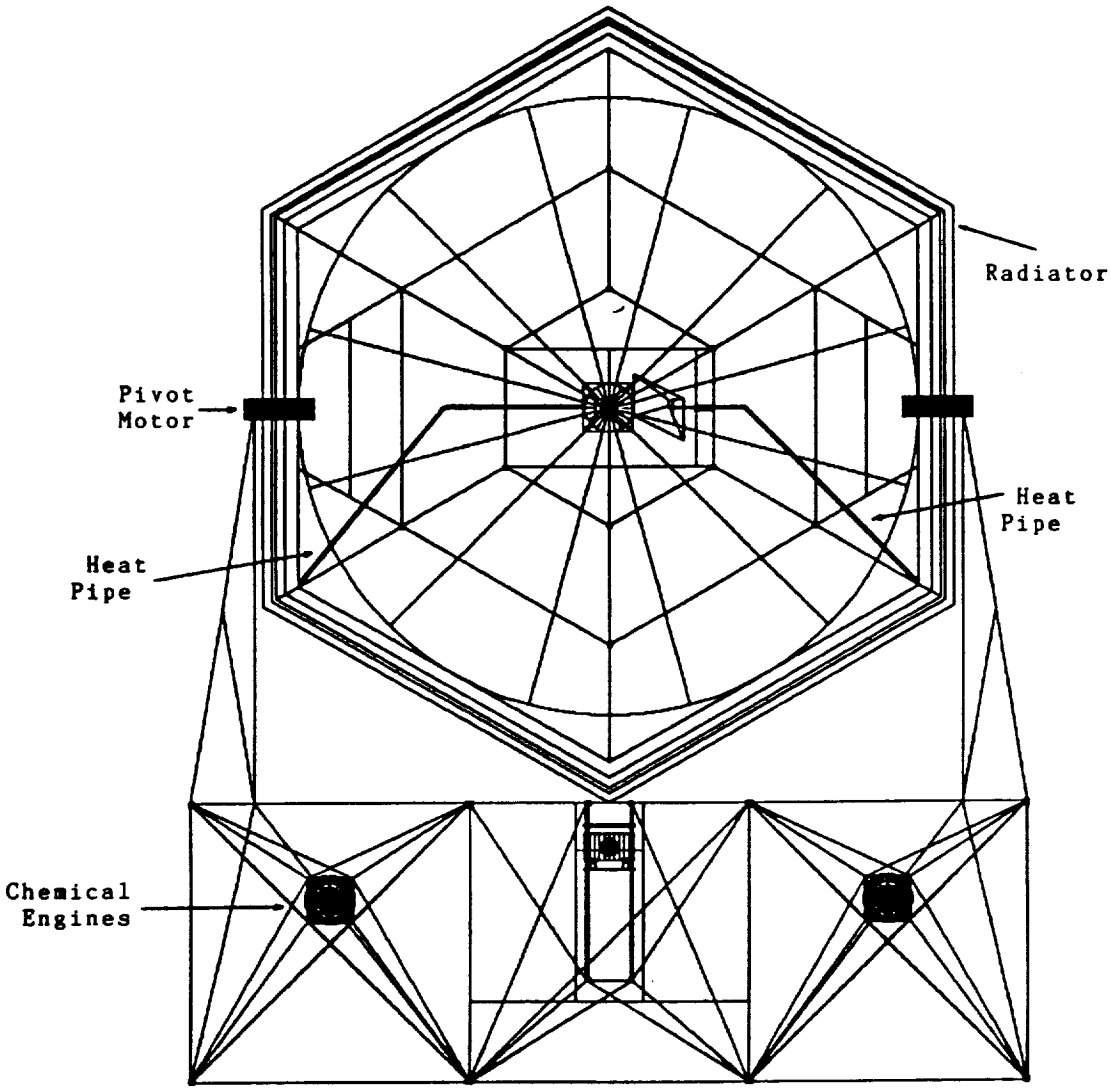

Figure 11. Optical System Configuration Rear View

Primary Mirror

The placement of the primary mirror is based on several criteria. First the effects of thermal and inertial loads on the structural members were considered. By analyzing these loads it was concluded that the mirror must be placed no more than 10 meters out on the tripod legs (below this maximum value, the vibrations and stability are well within the limits imposed by the power losses).

Using this maximum value and considering factors such as the desired final beam width and cooling of the secondary mirror, a focal length of 8 meters was selected for the primary mirror.

The primary mirror can be seen in Figure 12 (viewed perpendicular to the gimbal mountings), Figure 13 (viewed along the gimbal mountings), and Figure 14 (off isometric view).

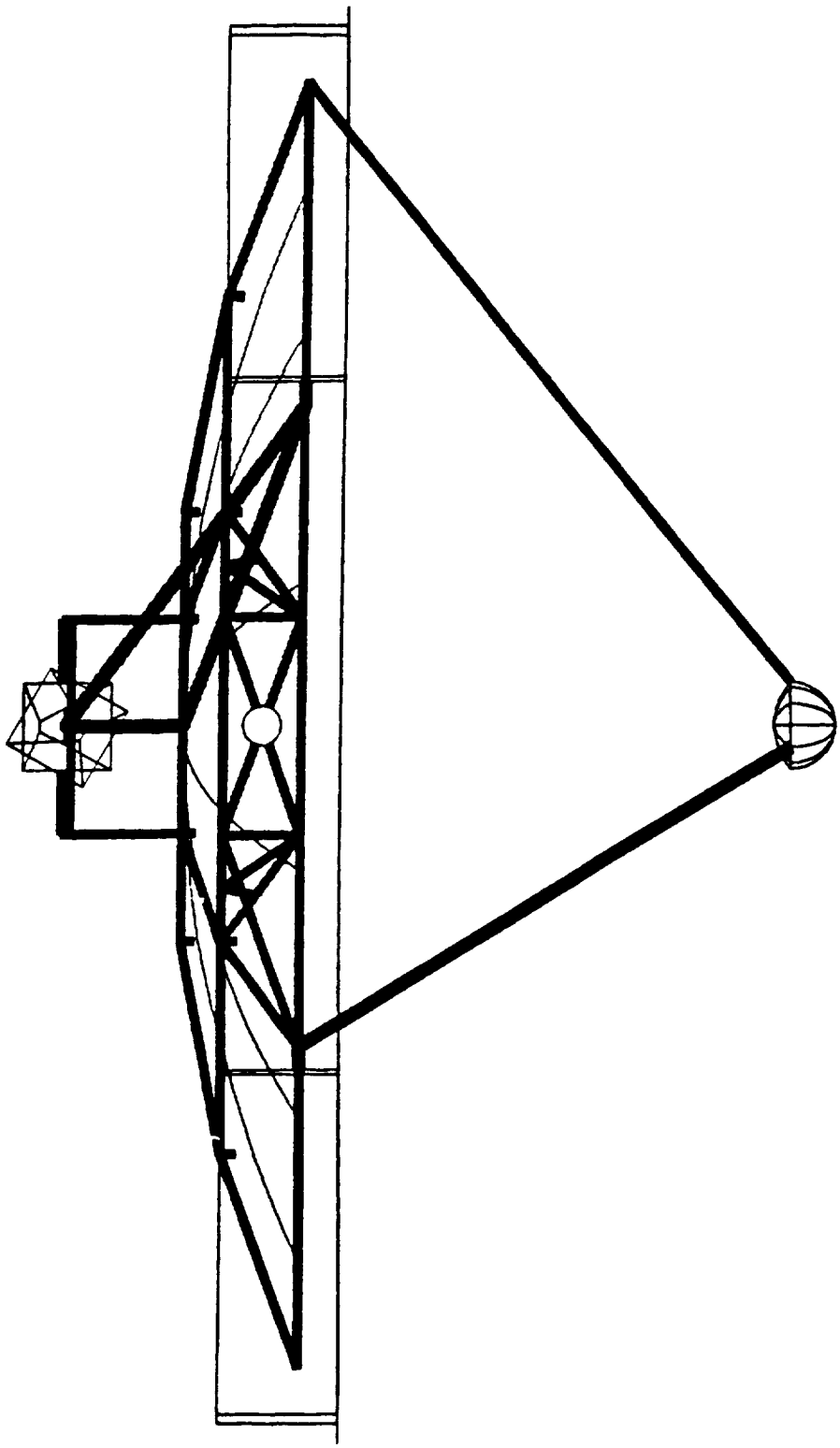

Figure 12. Primary Mirror View 1

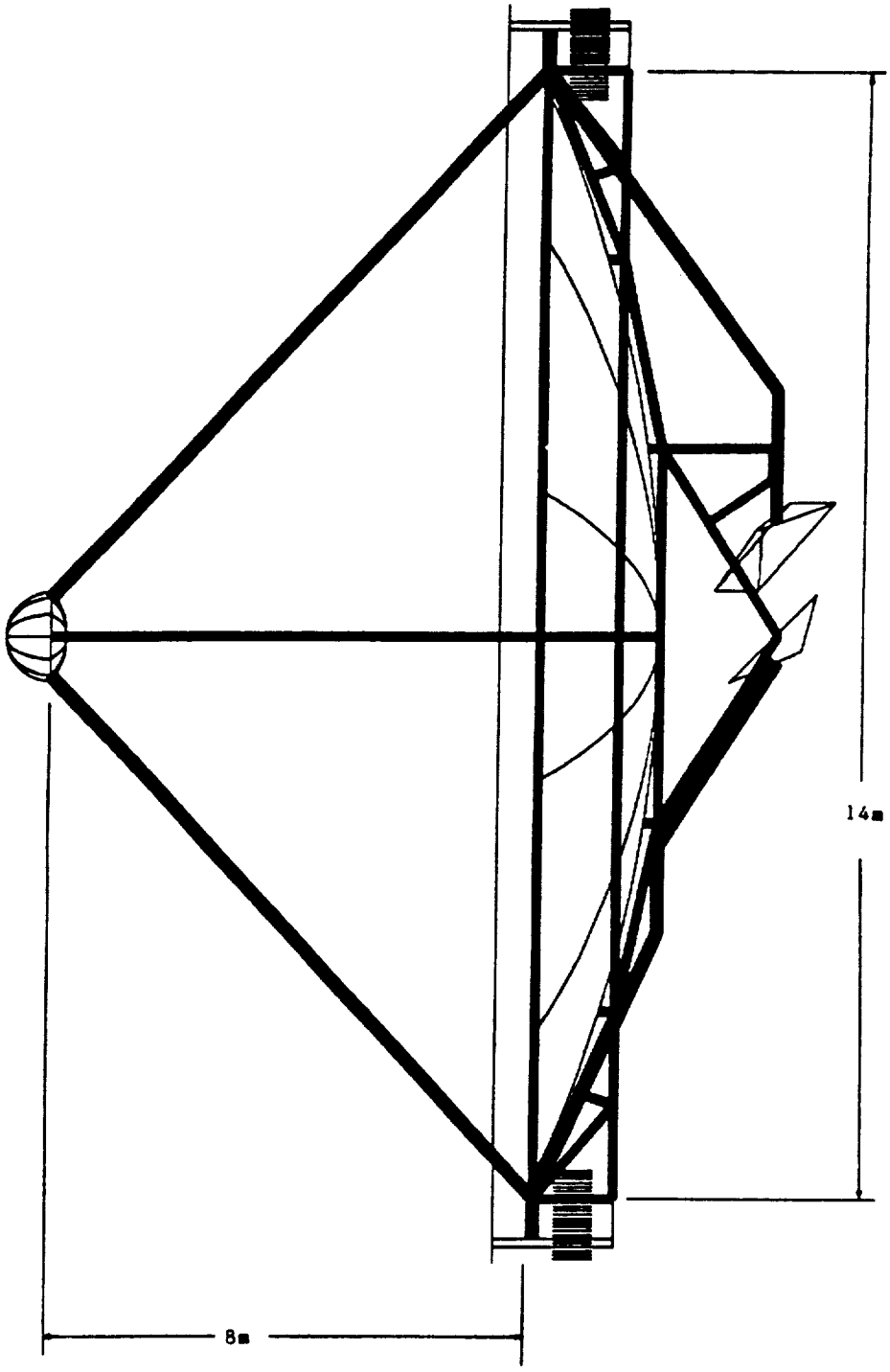

Figure 13. Primary Mirror View 2

Secondary and Third Mirror

The primary and secondary mirrors share the same focal point, one-half meter beyond the second mirror. By arranging the mirrors in this configuration one obtains a colimated laser beam with a reduced diameter which is parallel and traveling in the same direction as the incident beam. The beam travels through the small hole in the primary mirror and is redirected by a planar, rectangular mirror which is fixed at a 45 degree angle to the common axis.

The secondary mirror is shown in Figure 15, Figure 12, and Figure 13. The combination of the primary and the secondary mirror can best be seen in Figure 12 and Figure 13.

Fourth Mirror

The whole system described above can rotate with one degree of freedom about two pivot points on either side of the primary mirror (Figure 12). The different positions of the mirror assemblies due to rotation can be seen in Figure 17. To allow for this movement, the fourth mirror, a planar, elliptical mirror which is also at a 45 degree angle to the incident beam, is able to rotate about its center axis as shown in the diagrams. By rotating this mirror, the beam is always able to be directed to the fifth mirror regardless of the position the larger system assumes (Figure 16).

Fifth Mirror

The fifth mirror (Figure 18), a curved elliptical parabolic mirror, has one degree of freedom in the vertical plane in order to capture the beam regardless of the position of the mirror system and direct it on a straight line into the laser rocket. This mirror focuses the beam down to the size of the window opening in the laser rocket engine and then the window focuses the beam to a point in the laser engine.

To determine the surfaces of the parabolic mirrors the equation

$$X^2 + Z^2 = 4PY$$

was used with P = the focal point. From the geometry, it was determined that the 5th mirror needed to focus the beam by 2°.

Mirror Assembly

The assembly of the primary mirror is a concern in the design of the optical system. The method chosen was to divide the mirror up into 12 equal area wedges. The wedges will be "snapped" together once in space. All 12 wedges stacked together--with allowances made for packing materials--will fit into a rectangular box with dimensions 3.6×8×6.5 m. This box will fit into the cargo bay of the space shuttle.

Optical Train Control

The performance of the optical train is critically important to the performance of the ship as a whole. Small deflections in the optical train may cause a significant loss of power. For this reason, almost every optical component will be equipped with electrically controlled feedback sensors which will monitor the mirror at all times. The feedback system is described in the chapter on acquisition, tracking, and pointing. If the mirror deflections become to great in one direction these devices will sense this and correct the problem.

A deflection analysis was performed on the small secondary mirror in order to analyze a "normal" deflection. It was found that a power loss of 9.9 kW corresponds to a deflection of .00098 m from

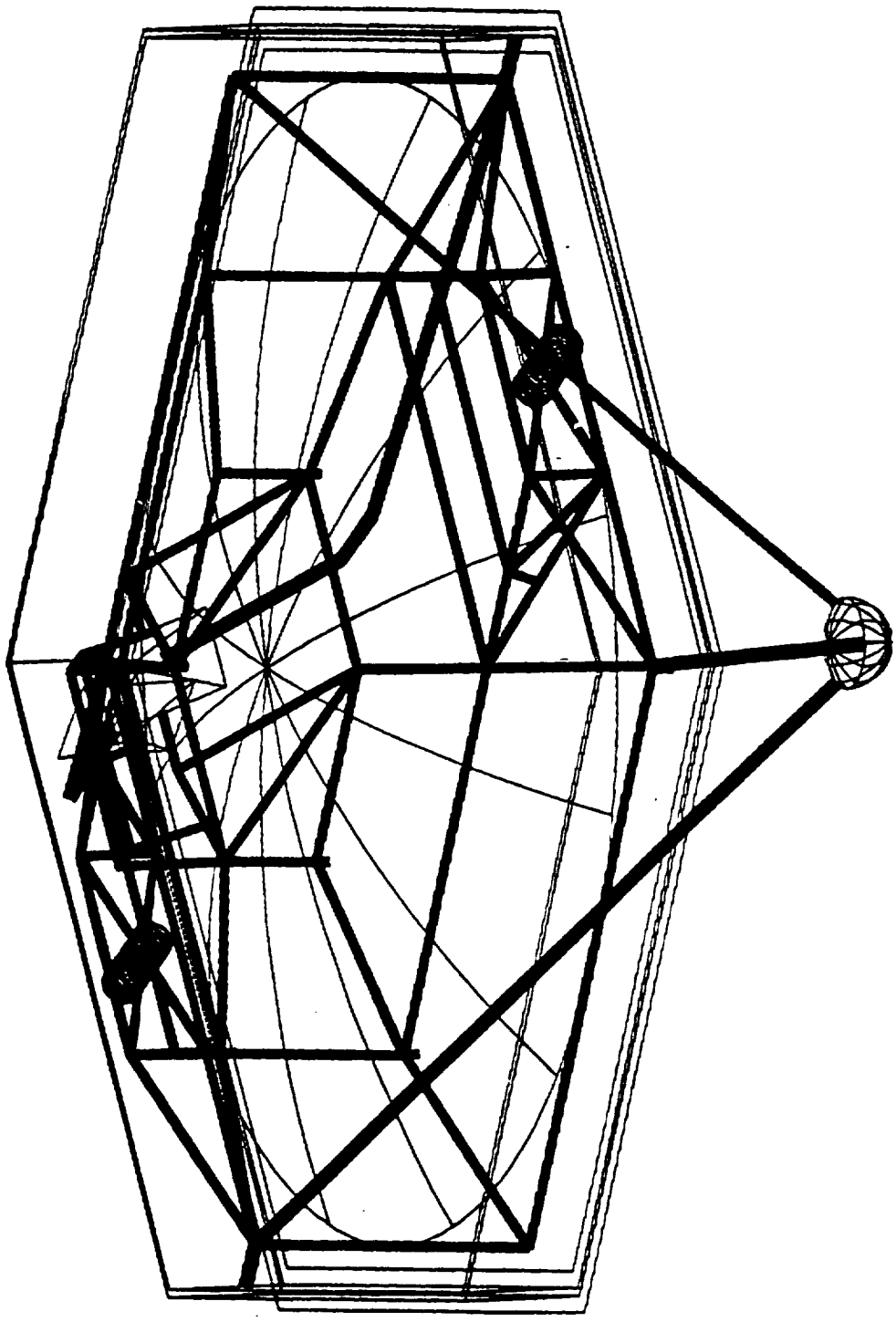

Figure 14. Primary Mirror Off Isometric View

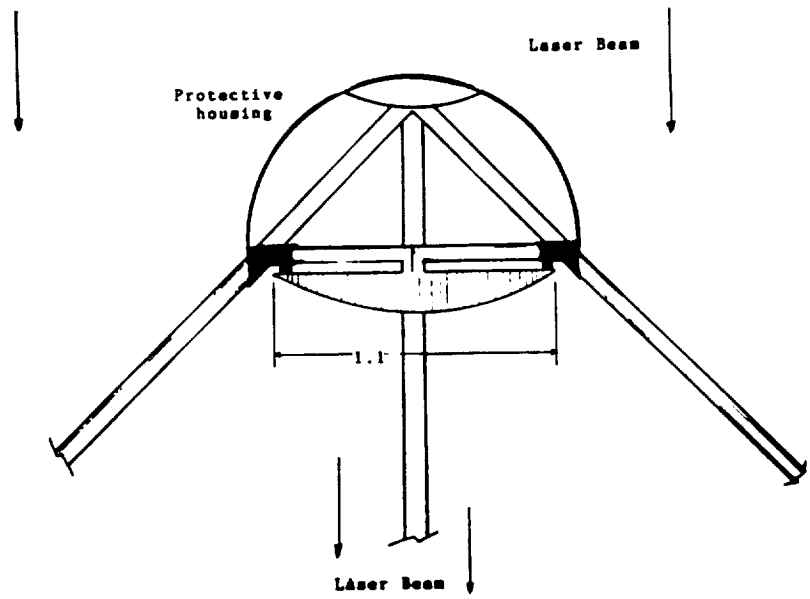

Figure 15. Secondary Mirror

the central axis. This deflection is much less than the deflection anticipated by the structural analysis. Therefore, the control system will most likely only be used for abnormal deflections.

Motors and Power Requirements

Some of the optical components require motors. In order to determine the power needed by these motors a future technology value of 0.2984 kW per pound of motor weight was used. The primary mirror uses two small motors at its pivot points in order to move the mirror to any desired position. These motors together require approximately 150 W. The fourth mirror has a torque motor mounted on the piece of the truss to which the mirror is attached. This motor requires 20 W to rotate the mirror. The fifth mirror uses a linear actuator to move on its vertical axis (Figure 19). This actuator is powered by a small 30 W motor mounted on the side of the actuator. Finally, the heat pipe system needs 1.4 kW of power for the auxiliary heating units. The total power requirements for the optical system is approximately 1.6 kW.

Dielectrics

The multi-layer dielectric coated mirror was chosen over other types of mirror schemes. First, the dielectric coatings offers a higher reflectivity (99.9%) with small mass compared to a metal (copper) mirror. Also, the dielectrics are becoming easier to assemble in space, and the degradation over time is reduced. Also, new techniques are making the application of the dielectrics easier and more precise.

Beryllium was chosen as the facesheet or substrate material onto which the dielectric coatings will be applied. Beryllium was chosen over silica and other materials because of its many attractive properties. These include, a low density which translates into a low mass per unit area, good

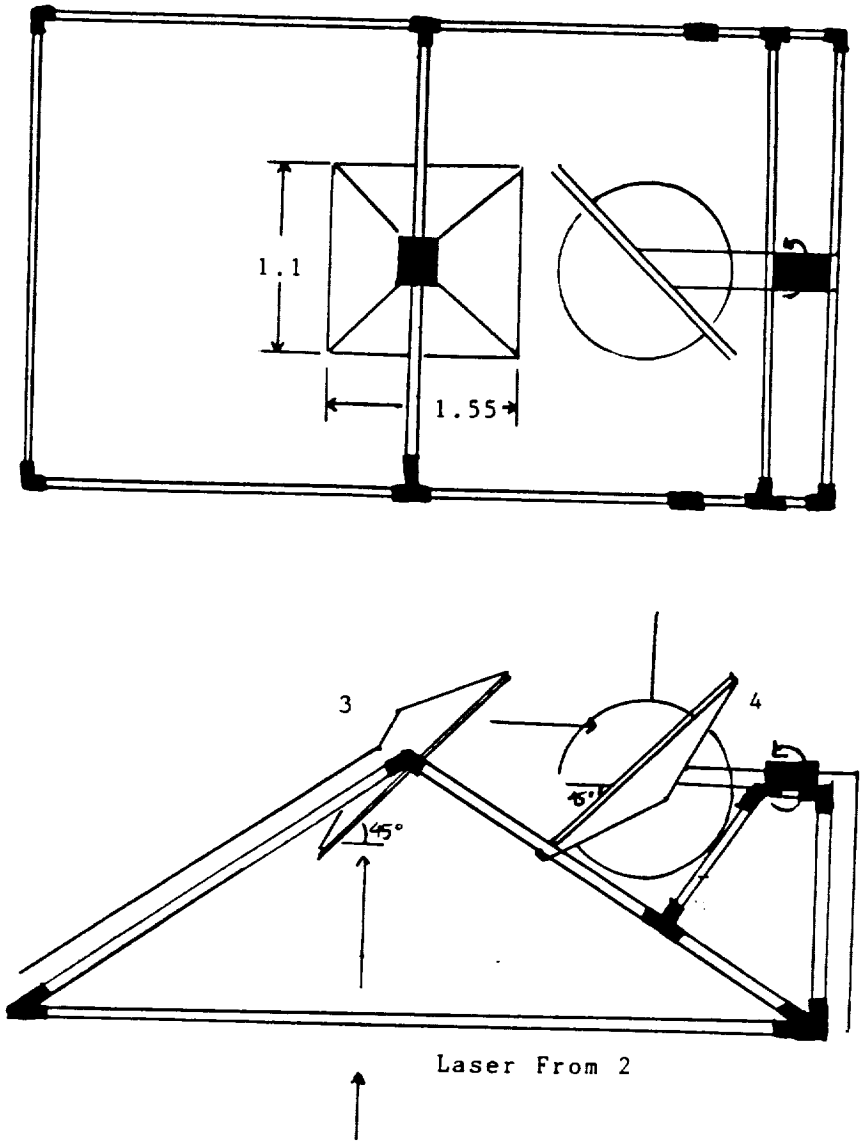

Figure 16. Third and Fourth Mirrors

thermal conductivity which makes cooling easier and good manufacturing tolerances which is important in applying the dielectric layers. The dielectric layers themselves were chosen to be silicon and magnesium oxide. The absorption for this pair in the laser beams wave length range is about .03%. This low absorption greatly reduces the cooling requirements for the mirrors. The dielectric layers are applied to the substrate in layers of alternating high and low refractive indexes with each layer .328 micrometers or 1/4 wavelength in thickness. The first layer, silicon, is applied directly to the beryllium facesheet. Then alternating layers of silicon and the low index material, magnesium oxide (MgO), are applied. To achieve 99.9% reflectance a total of seven layers of dielectric materials must be applied to the facesheet. The odd number of layers becomes necessary because, in order for the reflections to be in phase, the high index material needs to be last and first since its index is greater than beryllium. On top of the dielectrics, an outer protective layer, constructed from an oxide material, will also be added to provide environmental stability, thus increasing the useful life of the dielectrics. This scheme can be seen in Figure 20.

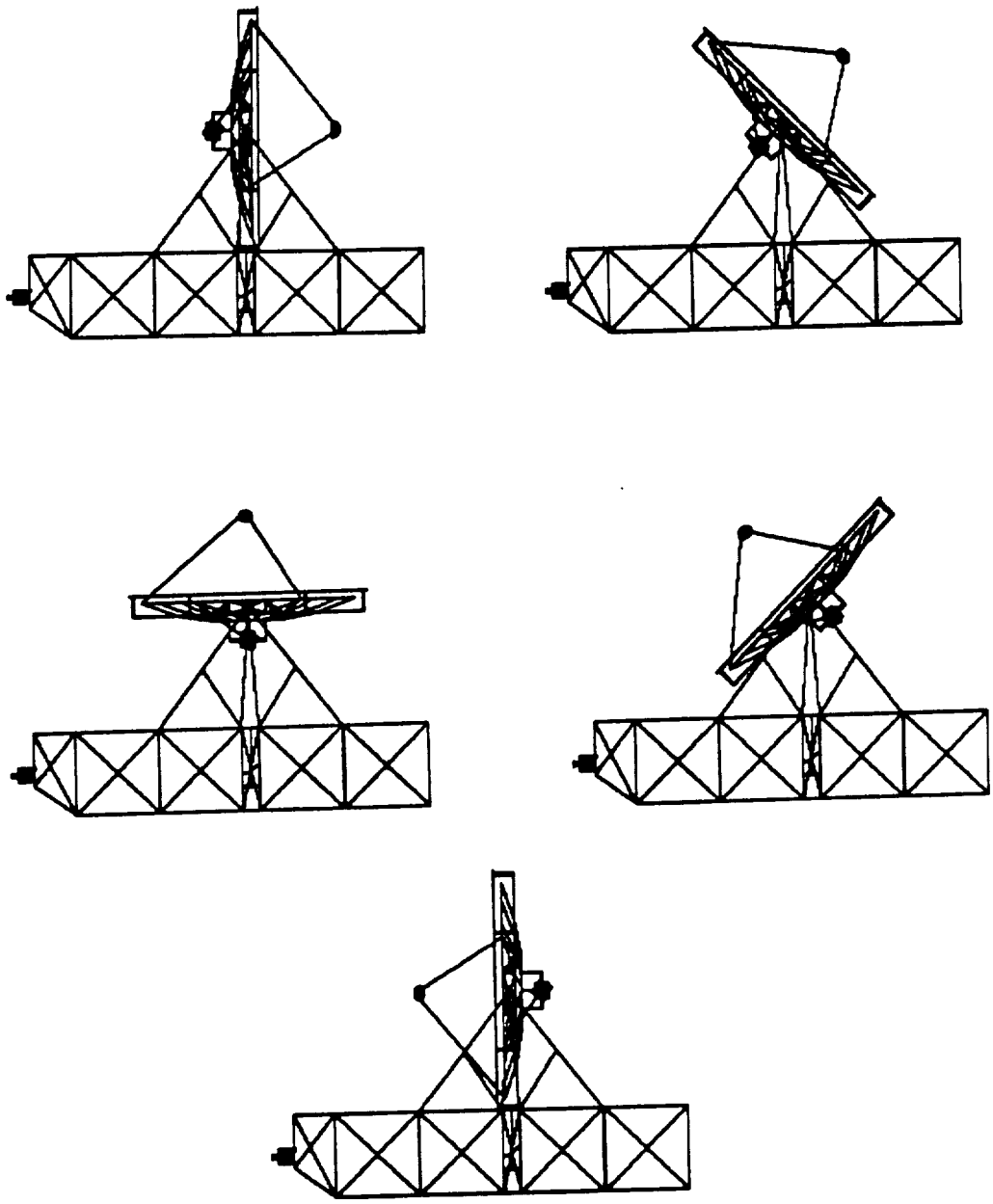

Figure 17. Different Positions Due to Rotations of Primary Mirror Assembly

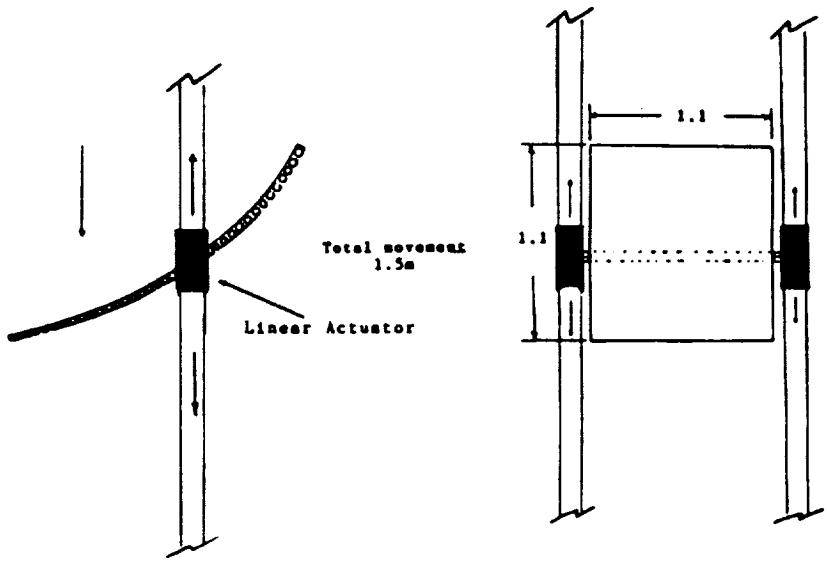

Figure 18. Fifth Mirror

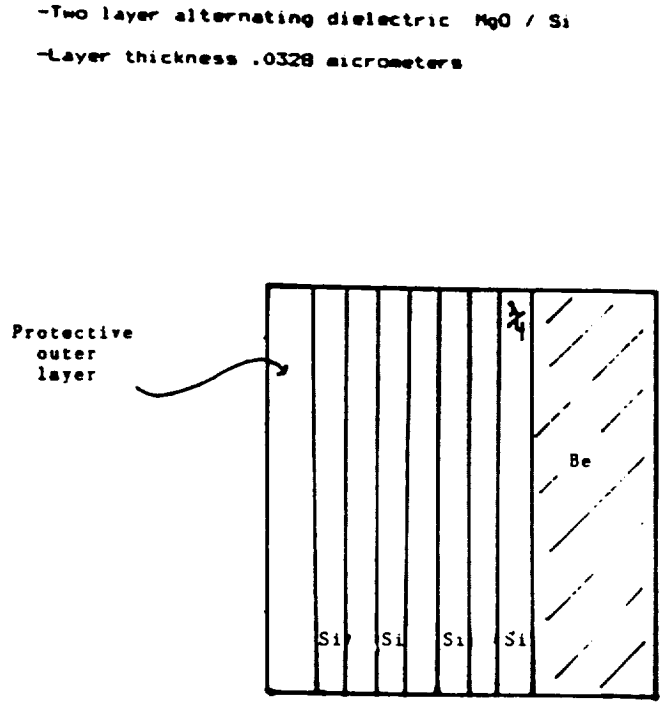

Figure 20. Dielectric Layering Scheme

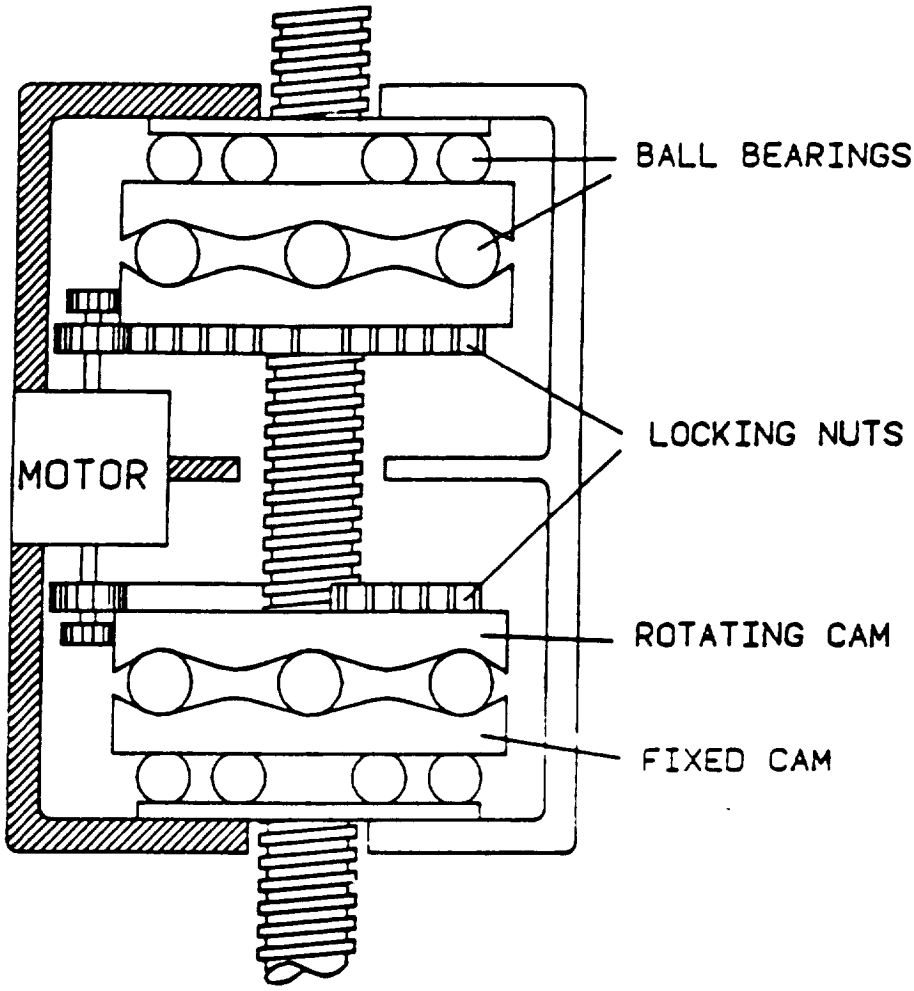

Figure 19. Linear Actuator Used to Move Fifth Mirror

A few areas of improvement for the dielectrics are anticipated in the future. This includes better compensation for strain, improved reflectance and increased useful life. In order to accomplish this the electric field inside the layers must be controlled. By deviating from the standard 1/4 wavelength design this can be accomplished. If possible, the maximum electric field should be positioned in the middle of the low index material (MgO). Also, the electric field should be minimized at the interfaces of the dielectric materials. This will reduce the absorption and increase the damage resistance.

Cooling

The cooling of the optical components is a important aspect in designing the optical system because of the high power of the laser. The first step in this process is to calculate the reflectivity of the optical components. These are shown in Table 11 with both beginning and end-of-life reflectivities.

Table 11. Mirror Reflectivities

Mirror	BOX	EOL
First	99%	97.5%
Second	99.9%	98.4%
Third	99.9%	98.4%
Fourth	99.9%	98.4%
Fifth	99.9%	98.4%
Window	99.9%	98.4%

From this data, the energy of the laser absorbed by each component was calculated. Using the absorbed power and accounting for the solar radiation in space, the Stefan-Boltzmann law, $\dot{q} = \varepsilon\sigma A T^4$, was used to calculate the steady-state temperature of each component. The thermal gradients were also calculated for the primary mirror. Using the thermal gradients and a thermal expansion coefficient of 0.04×10^{-7} per °K, the expansion of the front surface of the mirror was calculated (Appendix A). The expansion was on the order of 10^{-5}% during the three hour cycle. This does not represent a problem initially but, over time these stresses may cause degradation of the mirror surfaces.

A maximum temperature of 600 K was chosen for the dielectric surfaces, in order to insure their stability. So, as Table 12 indicates, the primary mirror does not need auxiliary cooling mainly because of its size and construction.

Table 12. Optical System Thermal Analysis

Optical Component	Steady State Temp. (K)	Energy Absorbed (KW)
Primary Mirror	430.08	255.25
Secondary Mirror	1370.33	161.5
Third Mirror	1179.76	159.8
Fourth Mirror	1279.3	156.2

Maximum temperature for dielectric surfaces is 600 K

However, the other components do need to be cooled. The design chosen specifies that the mirror closest to the engine and the engine window to be cooled by using the hydrogen fuel. This will eliminate the need of using heat pipes in the 5th mirror. The other mirrors will be cooled using a heat pipe system. A variable conductance heat pipe with an arterial wick (stainless steel) and active electrical feedback control was chosen (Figure 21).

The feedback design was chosen because of its ability to maintain a device mounted at the evaporator at a near constant temperature, independent of the power being generated by the device. The arterial wick is necessary for heat pipes in space because it provides a low pressure path for transporting a liquid. Other notable features of this heat pipe are: a heat source control, easy adjustment, minimum storage volume, and no moving parts. The only drawback to this system is that it needs auxiliary electrical power. This design also offers good reliability as it has been used on satellites in the past.

The first step in designing the heat pipe system was to determine the total amount of cooling capability needed. Considering all three mirrors to be cooled this value is 477.5 kW. Using this and Stephan-Boltzman law with $\varepsilon = .85$, the minimum area of the radiator, 76.5 m^2 , is obtained (see Appendix A). The radiator is placed around the primary mirror and radiates away from the mirror surface (Figure 22). A heat pipe cross-sectional radius of .05 m was calculated as the radius needed to facilitate the amount of cooling which was needed. The choice of a working fluid for the heat pipe system involved checking many different figures of merit. The two fluids that work well at high temperatures (1200 °K) are Li and Na. Li was chosen because it performs better in the heat transport category and it will not boil as quickly (see Appendix A). The fluid flow of the heat pipe can be seen on the mirror in Figure 22 and Figure 23.

Table 13. Optical Train Masses

Material	Mass (kg)	
Beryllium	577.2	
Dielectrics	1.447	
Gr/Ep (honeycomb)	1497.0	
Total Mirror Mass		2075.6
Truss Structure:		
Primary Mirror Truss:		
Tripod members:		
TOTAL PRIMARY MIRROR MASS	2132.7	
Secondary Mirror Mass	120.0	
Mirrors 3&4 Mass	200.0	
Mirror 5	100.0	
TOTAL OPTICAL SYSTEM MASS	2593	

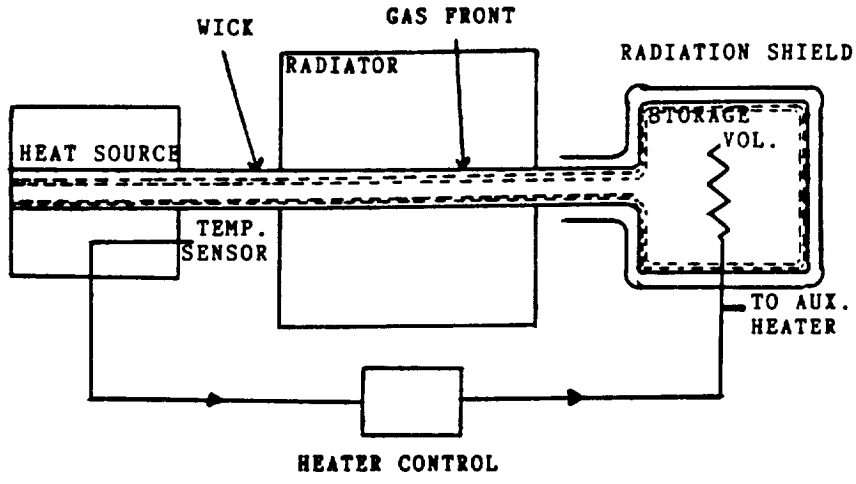

Figure 21. Feedback Control System

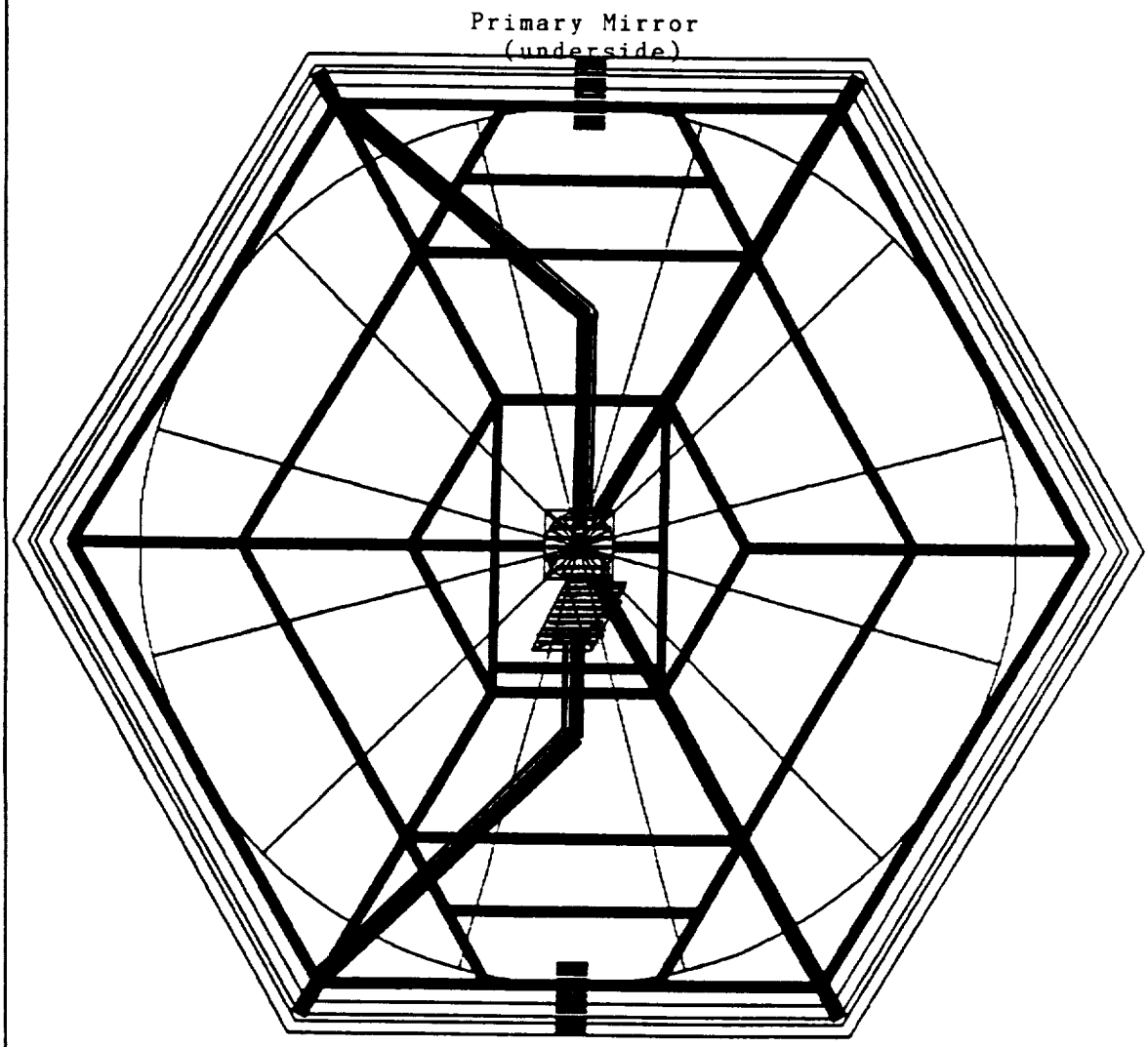

Figure 22. Radiator Placement and Heat Pipe Front View

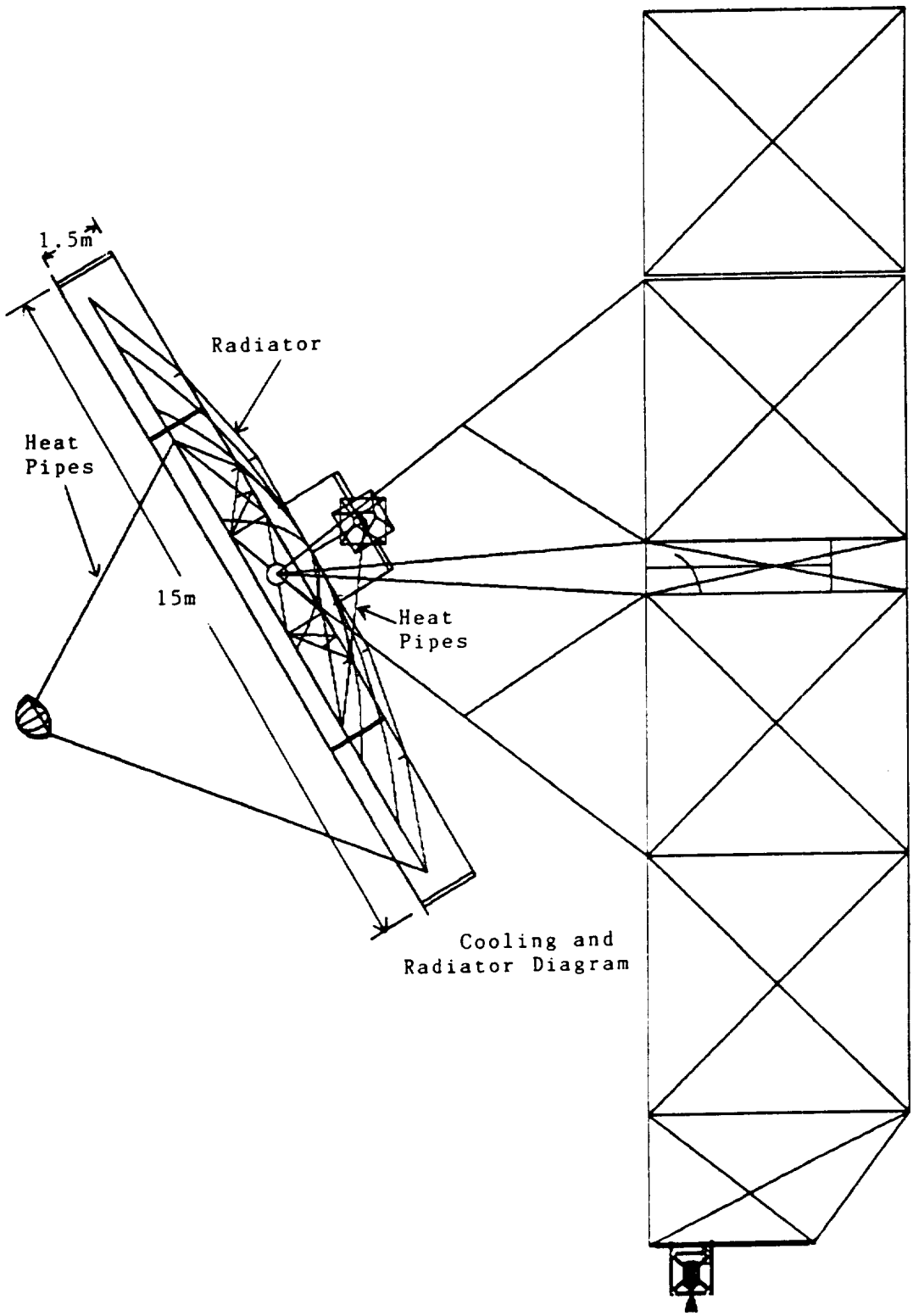

Figure 23. Radiator and Heat Pipe Placement Side View

Propulsion

Laser Propulsion

Introduction

The basic concept of laser powered propulsion is to transfer laser energy directly to the hydrogen propellant, thereby eliminating the need of carrying heavy oxidizers. There are four main methods of accomplishing this transfer. They are solid heat exchangers, molecular resonance absorption, particulate absorption, and the inverse Bremsstrahlung process.

Methods of Energy Transfer

The solid heat exchanger utilizes an absorber cavity to collect the focused laser energy and then transfer the energy to the propellant through a heat exchanger. Maximum operating temperatures of the engine limit the performance to well below the nominal 1500 second specific impulse assumed for this study. Thus this method of energy transfer was dropped from consideration.

In molecular resonance absorption, the hydrogen propellant is seeded with molecules. When these molecules absorb laser light, they undergo a transition from their ground state to a higher vibrational-rotational energy state. Molecular resonance absorption is very wavelength and seedant sensitive, and not enough research has been completed to justify near-term application of this method of energy transfer.

In the particulate absorption process, particles opaque to the laser light are injected into the rocket chamber. These particles absorb the laser energy, heat up, and form a plasma. They then transfer their energy to the propellant by conduction and convection. The particulate absorption process was chosen as the scheme to initiate the plasma at the beginning of each firing sequence of the rocket.

In the inverse Bremsstrahlung process, photons from the laser beam transfer their energy through inelastic collisions with the electrons, atoms, molecules, and ions of the plasma. In this process, the plasma is not self starting and therefore a scheme to initiate the plasma is needed. The inverse Bremsstrahlung process was chosen to be the main method of energy transfer for this vehicle.

Particulate absorption using carbon particles is chosen to initiate the plasma at the beginning of each firing sequence. Once the plasma is initiated, the carbon additives will be gradually decreased until the plasma is capable of sustaining itself by the inverse Bremsstrahlung.

Assumptions

Degradation effects of the reflective surfaces were considered to account for an approximate 6% power loss through the optical train. Previous studies (Ref. Frisbee) suggest that a 1500 second specific impulse is a realistic value for the laser engine. They also assume a nominal thermal conversion efficiency of 50%. The basic assumptions upon which the laser engine parameters were established are listed in Table 14.

Table 14. Basic Assumptions

Power of incoming laser (P)	12 MW
Iodide laser wavelength	1.315 micrometers
Optical train efficiency (OE)	94.14 %
Thermal conversion efficiency (TE)	50 %
Specific impulse (I)	1500 sec

Laser Propulsion Parameters

The thrust of the engine was determined from the energy equation

$$T = \frac{2P \times OE \times TE}{I\ g_e}$$

From this, the maximum thrust was calculated to be 768 Newtons.

The hydrogen mass flow rate is

$$\dot{m} = \frac{T}{I\ g_e} = .0522 \text{ kg/sec}$$

On the basis of the calculations performed in the aerospace department at Virginia Tech, increasing the chamber pressure from 1 atm to 10 atm leads to an increase in the absorption coefficient from .5/cm to 23/cm. This higher absorption coefficient will allow for full energy absorption within a shorter distance in the plasma and therefore a smaller plasma size. For this reason a chamber pressure of 10 atm was chosen. To obtain a specific impulse of 1500 seconds with a chamber pressure of 10 atm, the chamber temperature was established to be 4400 K. The nozzle area ratio was set at 80.

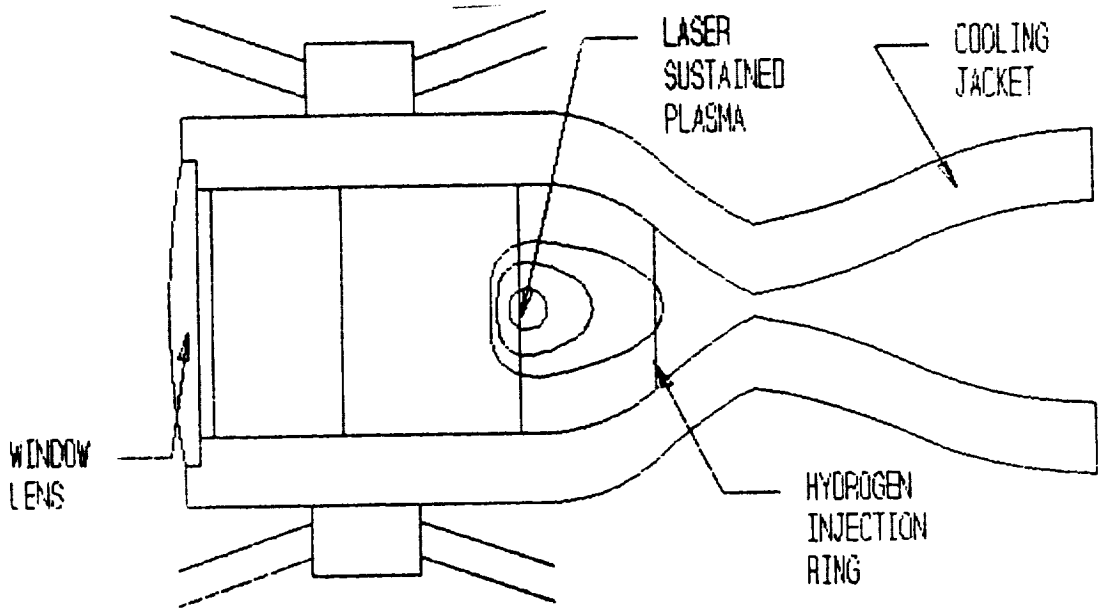

Figure 24. Laser Rocket Engine

The front of the laser engine will consist of a plano-convex window lens made of sapphire, which was chosen because of its high transmissivity and strength at high temperatures. The window will be anti-reflectively coated on the outside, to allow for maximum transmition of the laser beam. The window will also be reflectively coated on the inside, to keep the radiation emitted from the high temperature plasma inside the chamber. The spot size of the incident laser beam on the window was established from a desire to keep the power density below 25 kW/cm^2, which is the power density at which the laser supported combustion wave of the inverse Bremmsstrahlung process is capable of being sustained (Ref. Frisbee). This allows for less degradation of the window surface and keeps the plasma from forming next to the window. A spot size of 30 cm diameter was determined to be sufficiently large. The chamber diameter was then enlarged to 35 cm to allow for small off axis disturbances of the laser beam. The window lens has a focal length of 45 cm. The large focal length adds to greater plasma stability.

The throat characteristics were determined from a 1- dimensional model of the flowfield in the engine having a thermal efficiency of 50%, and producing a specific impulse of 1500 seconds. The main laser engine characteristics are summarized in Table 15.

Table 15. Laser Engine Parameters

Laser power entering the engine	11.3 MW
Thrust	768 N
Hydrogen mass flow rate	0.0522 kg/sec
Chamber pressure	10 atm
Nozzle inlet stagnation temperature	4400 K
Average chamber flow velocity	20 m/sec
Chamber diameter	35 cm
Throat diameter	3.2 cm
Nozzle area ratio	80
Window lens focal length	45 cm
Overall engine diameter	55 cm
Overall engine length	1.25 m
Total engine mass	150 kg

The hydrogen plasma has a core temperature of 20000 K. This leads to large radiative heat transfer to the chamber walls, which must be cooled to maintain engine integrity. The engine will be cooled by circulating the hydrogen propellant around it. After the hydrogen leaves the fifth mirror it will proceed to the laser engine where it will enter a cooling jacket surrounding the engine. One fourth of the total hydrogen mass flow will enter at the front of the engine to directly cool the window. The rest of the hydrogen will circulate around the nozzle and chamber before being injected into the chamber. The fuel will enter at the window port with a maximum temperature of 500 K and enter the chamber with a maximum temperature of 2300 K. The rocket basket is movable, therefore the hydrogen must flow through a flexible hose and not a rigid conduit. The flexible hose is attached to the adjacent strut by a spring. This keeps tension on the fuel line and keeps it out of the way of the incoming laser beam. A schematic of the engine mount is shown in Figure 25.

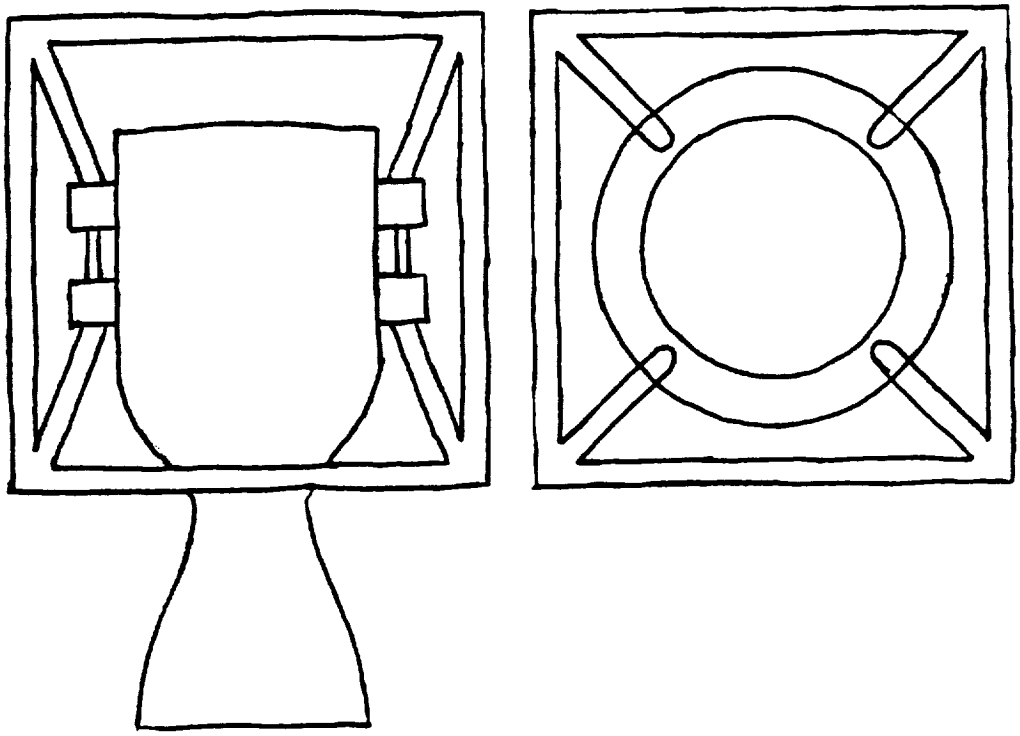

Figure 25. Laser Rocket Engine Mounting

Chemical Propulsion

Introduction

The first consideration in designing a chemical propulsion system is choosing a propellant. A bi-propellant scheme was chosen with liquid oxygen as the oxidizer and liquid hydrogen as the fuel. These were chosen because they offer high Isp, chemical stability, good pump properties and well proven performance in general.

Chemical Propulsion Parameters

Based on the mission specifications, a thrust of 25000 Newtons per engine with two engines located symmetrically on the vehicle was chosen. To calculate the properties of the flow in each engine, the computer code "NOTS" was used. The required input was the entering enthalpies of the reactants, the area ratio, the chamber pressure, and the oxidizer fuel ratio.

Table 16. Chemical Propulsion-NOTS Input

H (O_2)	-4300.00 kcal/kg-mole
H (H_2)	-212.46 kcal/kg-mole
Area Ratio	800
Chamber P	10.377 MPa
MR	6:1

The output of the program provides a detailed analysis of the flow in the chamber, throat, and nozzle of the engine. It uses a constant pressure heating then an isentropic expansion to the exit. The results are shown in Table 17.

Table 17. Chemical Propulsion-NOTS Results

	Exit	Throat	Chamber
Temperature (K)	702.43	3382.6	3602.1
Pressure (Pa)	507	5.7×10^6	10.377×10^6
Velocity (m/s)	4840	1616.1	91
Molecular Weight	14.1	13.6	13.4
K (Cp/Cv)	1.261	1.197	1.198

Max Thrust in Gs	.51 g
Mass Flow Rate	5.17 kg/s

Combustion Products

Name	Formula	Mole Percent of Gas Chamber	Throat	Exit
Hydoxyl	HO	4.6645	3.5238	0
Dydroperoxyl	*HO2*	.0028	.0013	0
Water	*H2O*	65.954	68.4085	75.6
Hydrogen Peroxide	*H2O2*	.0017	.0008	0
Monatomic Oxygen	O	.3982	.2536	0
Monatomic Hydrogen	H	3.6311	2.9616	0
Diatomic Oxygen	*O2*	.4124	.2779	0
Diatomic Hydrogen	*H2*	24.9354	24.5724	24.4

The specifications of the engine are shown in Table 18. The calculations involved in obtaining the dimensions of the engine are given in Appendix B.

Table 18. Chemical Propulsion Rocket Geometry

	Diameter (m)	Length (m)
Throat	.0398	.076
Exit	1.126	----
Nozzle	----	2.03
Chamber	.1244	.3731
Total	----	3

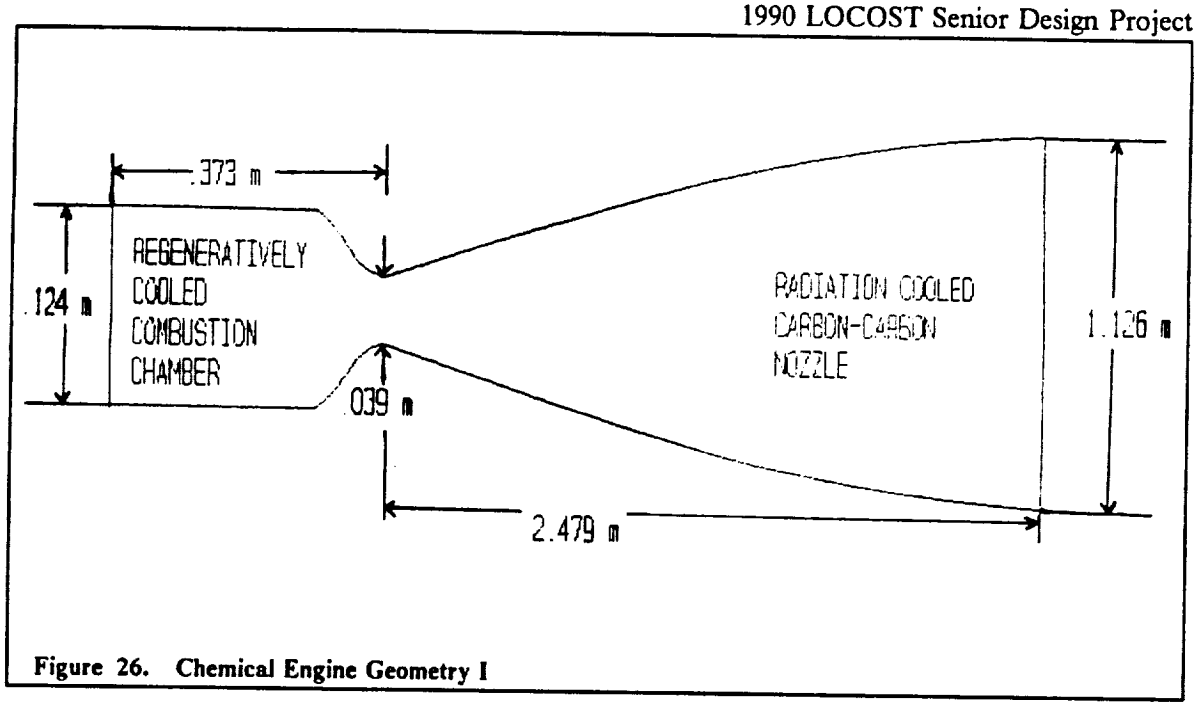

Figure 26. Chemical Engine Geometry I

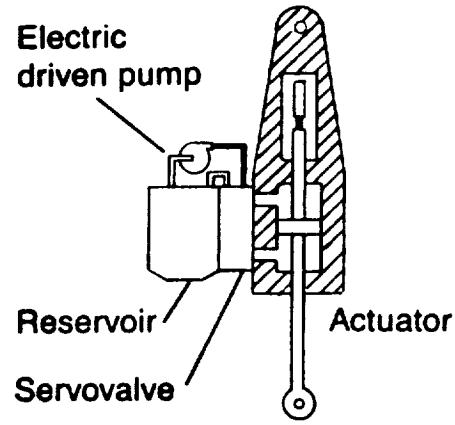

Figure 27. Gimbal Actuator

A schematic of the engine is shown in Figure 26. The gimbal mount for each of the engines will provide the capability to pivot the engine plus or minus six degrees to help keep the center of mass of the vehicle aligned. The motion of the gimbal is provided by a hydraulic actuator which uses an electric oxygen pump. Some advantages gained through the use of this system are a high frequency response, low power consumption, self containment, and easy checkout. A few potential problems are possible leakage, temperature effects, and it is comparatively heavy. A schematic of the actuator used can be seen in Figure 27.

Chemical Rocket Cooling

The engine is cooled using gaseous hydrogen. The engine is based on an expander cycle, which will be explained in greater detail. In an expander cycle engine, the cycle power depends on the turbine working fluid energy. Higher coolant exit temperatures are limited by the thermal conductivity of the wall material and the hot wall temperature of the thrust chamber as well as coolant velocity. The $H_2 - H_2$ regenerator utilizes energy from the turbine discharge flow to preheat the chamber coolant to approximately 705 °K providing hydrogen in its gaseous state for cooling.

The chamber regenerative coolant enters the inlet manifold located at the injector face plate and flows into and through the nontubular combustion chamber to the throat area. The maximum temperature of the engine is reached at the chamber wall on the interior. Gaseous hydrogen is used as the coolant because of its high specific heat, good stability, and low vapor pressure. The coolant passage in the nozzle is a double helix configuration. The average coolant velocity is 4.6 m/s, and the flow rate varies with the thrust.

Materials

The chamber utilizes electroformed nickel in the shell and copper- zirconium in the coolant barrier. The nozzle is constructed of carbon compounds which are highly heat resistant and very strong and light. The gimbal mount is made of an aluminum alloy. All materials used fall into the safe limit for performance at the temperatures predicted to occur in the engine. The thickness of the chamber and nozzle walls are approximately 3 mm, and the throat approximately 4 mm. A breakdown of the masses of the individual components of the engine are presented in Table 19.

Table 19. Chemical Propulsion Individual Component Masses

Component	Mass (kg)
Nozzle	69
Chamber + Cooling	101.1
Screw Jacks + Actuation	20.5
Gimbal Mount	4
Turbopumps	60.7
Heat Exchangers	54.3
Control Valves	54
Miscellaneous	63
Total	426.6

Injectors

The injectors used in this engine are multiple-hole impinging jet injectors, like the ones used in the S-4 engine. The injector pressure drop of the oxygen injectors is 0.74 MPa and the hydrogen is 0.48 MPa. The number of oxidizer orifices is approximately 432 and the fuel orifices is 668. The final velocity in the chamber after the propellants have been injected is approximately 91.4 m/s.

Pumps and Turbines

The pumps used in the engine are run off the gaseous hydrogen. To start the pumps and to get them up to speed, an electric motor is used. Details of how the pumps and turbines are interconnected will be given. The power of the hydrogen pump is approximately 0.11 kW and the oxygen is 4.7 kW.

The turbines used must achieve very high speeds of about 8376 rad/s. They are also very small, having a blade tip diameter of 2 cm and a blade root diameter of 1.5 cm. The power of the hydrogen turbine is 287.277 kW and the oxygen is 172.7 kW. The turbine efficiency is 0.8 in both cases and the pressure ratios are 7 and 3 respectively. The temperatures endured do not go much above 1500 K.

Expander

In an expander cycle, most of the coolant is fed into a low-pressure- ratio turbine after having passed through the cooling jacket where it picked up energy. Five to fifteen percent of the coolant bypasses the turbine and rejoins the turbine exhaust flow before the entire coolant flow is injected into the engine combustion chamber where it mixes and burns with the oxidizer.

The H_2 enters the engine through a ball type inlet shutoff valve mounted on the inlet of a low pressure pump that is gear driven from the main oxidizer turbopump shaft. From the low pressure pump, the fuel enters the first of two back to back shrouded impeller centrifugal stages. 5.8 percent of the fuel is used as a thrust-piston balancing flow for the high pressure pump. This flow is taken off at the second stage discharge, circulated to the thrust piston, and then injected back into the propellant flowpath at the high pressure pump interstage. The flow then moves from the high-pressure pump discharge and enters the H_2-H_2 regenerator which utilizes energy from the turbine discharge flow to preheat the chamber coolant. The flow is then routed through the turbines to provide the power to drive the turbopumps, and then through the hot side of the H_2-H_2 regenerator. After leaving the regenerator, the turbine bypass flow re-enters the mainstream and is injected into the throat chamber.

The oxygen enters the engine through an inlet valve similar to the fuel-side inlet valve and then flows into a low pressure pump. The discharge from the pump enters a single-stage, shrouded, centrifugal type, high pressure pump driven off a single stage, low reaction, full admission turbine. The flow continues to the oxidizer control valve, which is preset to give the desired mixture ratio. From the control valve, the flow enters the injector manifold and is injected into the combustion chamber.

Structures

Introduction

Many factors were taken into consideration before choosing the final structural design. Taken under consideration were the large payload mass and its placement, the amount of propellant needed for the mission, the placement of the mirror, time of flight, and space environmental effects. Even with an optimized design, a material that could withstand high stresses for long periods of time and numerous loadings was needed. The design and material must also resist large deflections to maintain accuracy in the optical train. Reducing overall structural mass was also an important design goal.

Truss Structure

The final main truss design is 29.11 m long logitudinally, 6.3 m deep (not including the mirror support structure), and 18.9 m wide. Individual truss members range in length from under 1.0 m to approximately 9.0 m with a characteristic length of 6.3 m. The members are made of graphite epoxy. They are cylindrical shells with a 5.4 cm outer diameter and a wall thickness of 0.16 cm. The vehicle is adaptable to carry extra fuel tanks when a greater than baseline payload must be transported (Figure 28).

Graphite/Epoxy (Gr/Ep) is one of the leading materials used in the construction of space vehicles. The composite material chosen was P75S/934 Gr/Ep with a ply orientation of $(0,\mp 20,0)$. Linear elastic behavior for tension loading and axial compression necessitates parallel arrangement of all longitudinal fibers to avoid plastic deformation. Compared to other alloys (Table 20), Gr/Ep displayed the highest modula of elasticity and lowest densities. Along with its high stiffness-to-weight ratio, it has an adequate crushing strength. Gr/Ep does not have a very high transverse strength, but the truss is designed to take its highest loads in the longitudinal direction, therefore alleviating the need for a large transverse Young modulus. These are not the only desirable properties of Gr/Ep. It is highly durable to the space environment with a favorable thermal stability, and it is easily available.

Table 20. Possible Materials for Space Truss

	Gr/Ep	Boron/Al	Al	Magnesium/Al
Ex(Gpa)	276	230	70	45
Ey(GPa)	6.9	160	70	45
Ult.Strength in tension long.(MPa)	660	570	110	380
tranv.(MPa)	18.7	380	70	165
Density (kg/m^3)	1165	2490	2710	1800

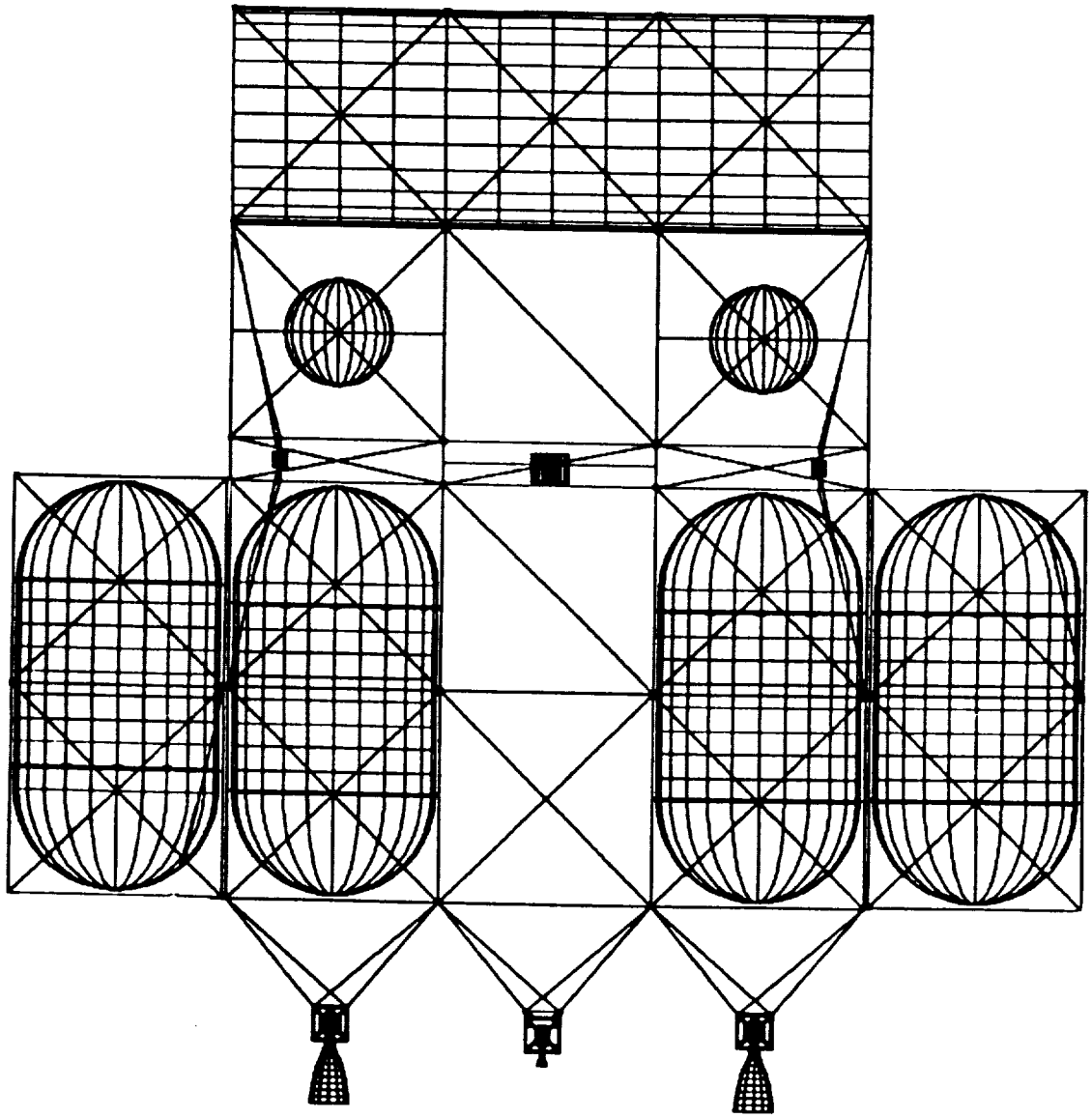

Figure 28. Scheme to Transport the Maximum Cargo

Environmental Effects

Atomic oxygen in LEO causes materials to deteriorate. Due to the fact that the vehicle orbits in and out of the earth shadow, thermal cycling occurs with temperature changes ranging from 120 to 400 degrees Kelvin (Ref. Dutta). Charged particle radiation and space debris cause material properties to degrade. Gr/Ep has been shown to have a long lifetime in LEO, but to alleviate some of the effects of the environment and to extend the lifetime of the structure material, a protective

coating is applied to the truss members. Aluminum foil with Ni electroplating, Teflon, and silver were studied. Chromic acid anodized Al foil appears to be the best choice for the following reasons:

1. High reflectivity and optical tailorabilty.
2. Resistance to atomic oxygen degradation.
3. Adherent to Gr/Ep and easy handling.
4. Affected minimally by abrasion.
5. Easy manufacturability and low cost (Ref. Dursch).

The foil surface is tailored during tube fabrication to increase diffuse reflectance of visible light so that the truss surfaces are not reflective. This makes working conditions more favorable for the astronauts during extra vehicular activities while only increasing absorptance to a minor degree.

Joint Design

The node design is similar to standard design used in space structures. The node elements are made of titanium alloy (Al6 V4), a material with a strength of the same magnitude as the Gr/Ep truss members, therefore ultimate load capability is not reduced by the joint construction.

Table 21. Possible Materials for Joint Design

Material	Ex & Ey (GPa)	Density(kg/m^3)
Titanium	114	4460
Aluminum	70	2710
Magnesium Alloy	45	1800

The titanium alloy is the only suitable choice for strut and node fitting design. Although using aluminum or Mg/Al would have resulted in significant mass savings, 39% and 60% respectively, titanium is the only material that tests up to the loads that the structure needs to withstand. In the construction of the mirror, however, the loads are significantly less so aluminum is used.

Some basic requirements in selection and design of the joints are:

- Adaptability to different payloads.
- Attachability to truss members from any angle.
- Maintainability of structural integrity.

The Gr/Ep members are fitted with two titanium end fittings. These are bonded using a cold hardening adhesive system. The adhesive is applied to the tapered contour of the composite material and inside the mating titanium groove. The adhesive layer thickness is applied uniformly except at the ends of the overlapping length. Increased adhesive thickness at the ends reduces the stress peaks at these locations. The stress distributions along the bonded sections are designed to be uniform (Ref. Franz). This bonded section is 50 mm long (Figure 29). After a destructive test program was conducted to ensure structural integrity, an ultimate load capacity of 167,000 N was found. The load capacity was not reduced by applied fatigue or temperature load cycles.

Seventy-five percent of the node elements are designed in an octagonal shape and are used in connecting 90 and 45 degree angle truss joints (Figure 29). The others must be made for specific angles. The outer nodes have payload attachment planes so that all additional equipment, payload, and propellant tanks can be mounted in various configurations. The sum of the combination of the titanium node elements and end fittings added a mass to the main truss main truss of almost 1300 kg.

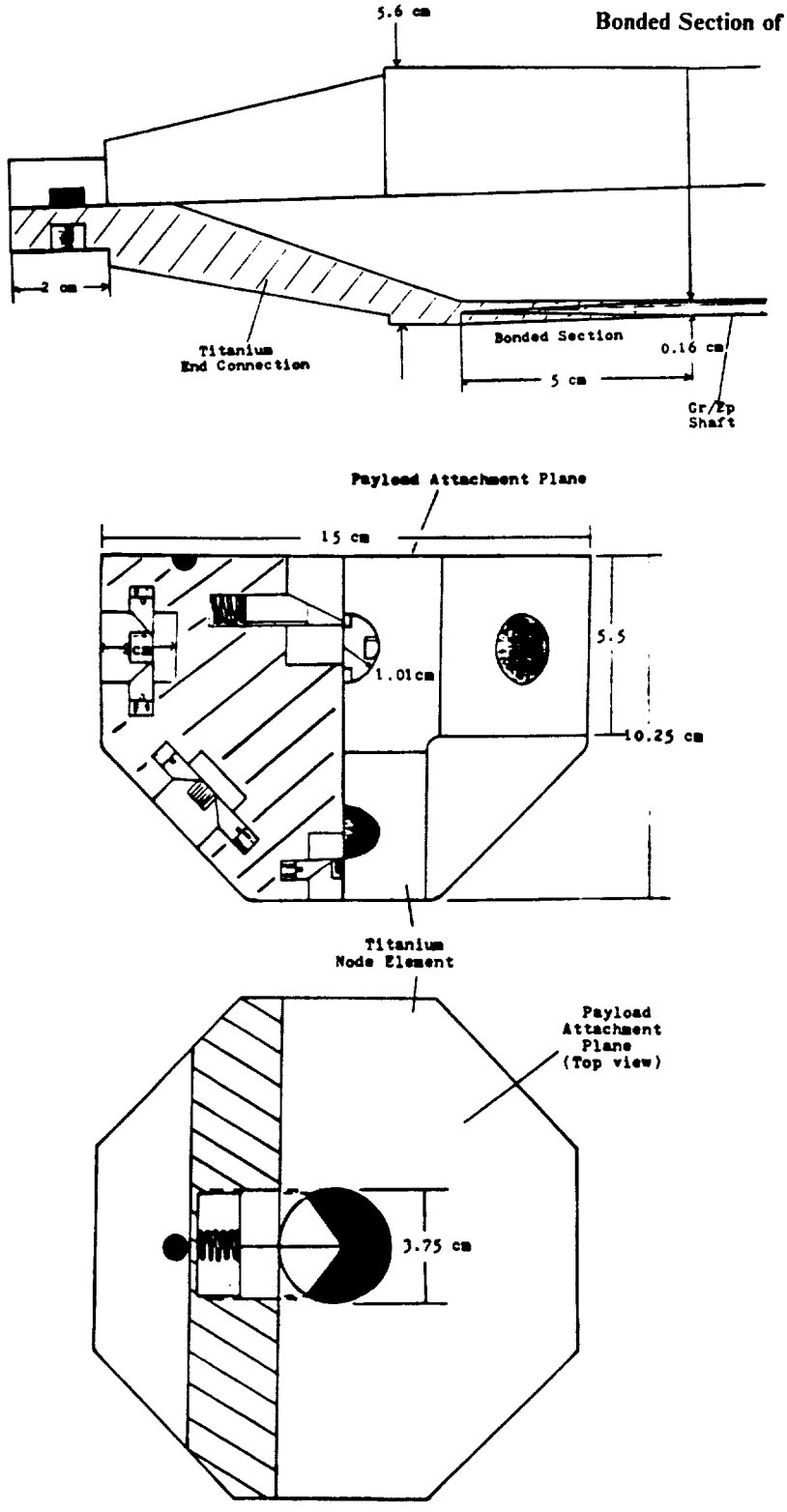

Figure 29. Titanium End Node Connector

Table 22. Main Truss Mass Breakdown

Material	Density	Cross-section	
Gr/Ep	1165 kg/m³	0.00025 m²	
Strut length	Mass	# Members	Total Mass
4.45 m	1.3 kg	166	215 kg
6.3	1.84 kg	100	184 kg
All Other			51 kg
Total Mass			450 kg

Table 23. Mass Breakdown of the Joints

Material: Titanium
Density: 4460 kg/m³

Element	Mass	# members	Total Mass
Node Element	4.5 kg	93	419 kg
End Fittings	1.5 kg	576	864 kg
Total mass			1283 kg

Structural Analysis

With our material selected and its properties known, a structural analysis was performed. The "Structural Software Analysis for Micros" (SSAM), a finite element computer program, performs a static analysis of all members of the space structure. Basic assumptions made in applying the truss to SSAM are as follows:

1. The nodes are considered as ball and socket joints and can sustain no moment force
2. The structure is statically loaded, so acceleration is constant and in the direction of thrust
3. The nodes connected to the rockets are restrained from motion in any direction
4. Inertial loads due to the payload, fuel tanks, and the mirror are applied at the nodes to which they are attached (Figure 30).

The program showed that the largest global loads occur in the members that support the rockets. This is as expected because the members toward the rear must support the load of all the components forward of it. Moving from the rear of the vehicle to the front, loads and stresses became progressively smaller. The forces and stresses in the rear members were on the order of 10^3 N and 10^7 Pa, respectively. The ultimate longitudinal tensile stress for this material is 0.66 GPa. This was not the restricting factor. The largest loads and stresses occurred in compression towards the rear. Using Euler's Buckling equation, $C_{cr} = \pi^2 EI/L^2$, Young's modulus, and the geometric properties of the strut, critical loads for each different length member were computed.

An analysis of the stresses was performed for the maximum acceleration case, 1.9 km/s^2 (during recircularization). The loads were calculated for full propellant tanks and a cargo mass of 40,000 kg. This is the worst case scenario and will never actually occur. At recircularization 40% of the fuel will already have been consumed which will cut the total mass and inertial loads by 35-40%. For the baseline mission the actual mass at recircularization was approximately 10% of the mass used for this analysis. Another analysis was performed for the actual recircularization case. In this case, the acceleration was 1.9 km/s^2 and the total instantaneous remaining mass was slightly under 20,000 kg.

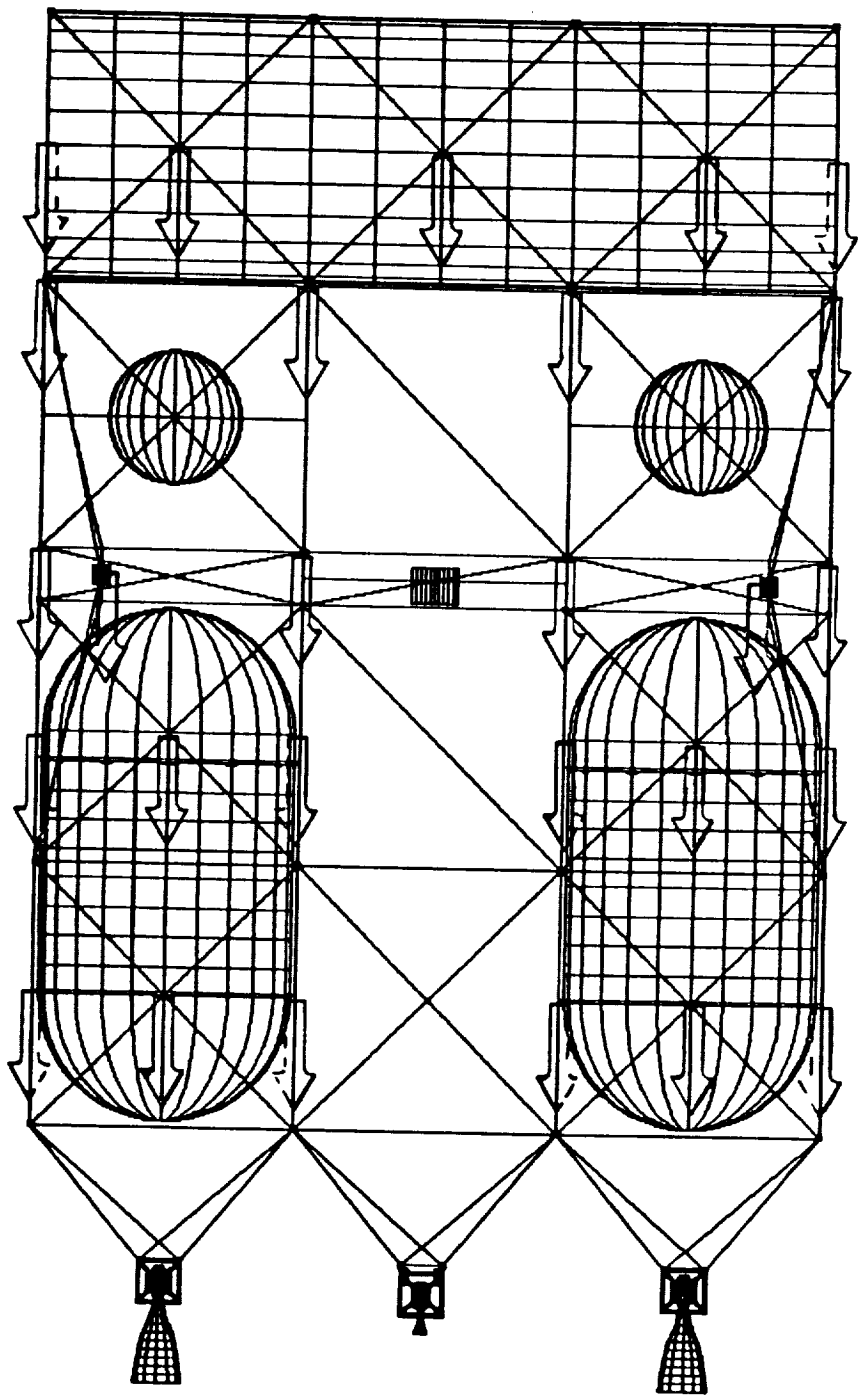

Figure 30. Inertial Loads on Main Truss

The smallest critical load occurs for the longest members because P_{cr} is inversely proportional to the square of the length. In addition to axial loading, critical stresses must be calculated. SSAM calculates the normal stress using loads and moments in all orientations to give the maximum normal stress.

Thermal Analysis

The temperature of the truss members are determined by a combination of three possible contributors (Ref. Van Vliet):

1. Absorbed heat from thermal radiation.
2. Heat radiated away by the exterior surfaces.
3. Heat produced by the space vehicle and its components.

The absorbed heat comes from three sources: the sun, the Earth, and the Earth's albedo (Figure 31). The energy not absorbed by the members could possibly be reradiated towards another member. This reradiated energy must be added to the total heat flux acting upon each member. The internal temperature determinant is in most cases negligible. However, since our mission involves the absorptance of a 12 MW laser beam, the heat due to the laser cannot be neglected. The sum of the heat which is absorbed by the primary mirror surface is reradiated out according to the mirror emmittance. Due to conduction, a percentage the radiated heat leaves the back of the mirror. This will constitute a heat flux almost twice that of the sun.

In order to do an analysis of thermal deflections with SSAM, five simplifying assumptions were made (Table 24) (Ref. Dursch).

Table 24. Simplifying Assumptions For Thermal Analysis

1. The top (mirror) side is shadowed by the mirror so external incident radiation is less than on the bottom.
2. The mirror radiates heat out of its backside which heats the top side truss members. The bottom side is almost completely protected from this heat flux by the fuel tanks, payload, and subsystems mounted inside the frame.
3. The expansion of the titanium joints is negligible compared to the strut elongation.
4. The orbits are considered circular.
5. The truss is assembled in LEO where the average temperature is 255 K

Where and at what temperature the structure is assembled influences the stresses and deflections the members will encounter. If deflections are assumed zero during assembly, then the temperature change each member undergoes is zeroed around the assembly temperature.

Using simplifying assumptions and the calculations in Appendix C, values for the extreme temperatures that the members would experience were found to be 435 K for the side exposed to the mirror heat, 395 K for the side exposed only to external radiation, and a cold temperature of 130 K. Applying these thermal loads, the total stresses and deflections that the Gr/Ep struts would experience due to heating was found.

As observed in Table 25 for the worst case, the maximum stresses are no greater than half the critical stress in any members. However, when a combined thermal and inertial analysis was performed, the maximum stresses were much closer to the critical stresses. When the inertial loads are reduced to realistic values and the truss is heated up to its most extreme temperatures, the maximum stresses are much greater. The thermal loads are of greater concern than the inertial. But the truss maintains its rigidity in these extreme cases. The highest strut temperatures are reached during operation of the laser rocket because of the heat contribution from the primary mirror. This is, however, when the vehicle is under the least inertial loading because the laser engine thrust is 98.5% less than both the chemical engines combined thrust. Therefore, the maximum stresses encountered in the combined analysis are greater than the stresses encountered during normal laser thrusting with maximum truss heating.

Table 25. Stress Analysis of Loads

Case: Worst with No Thermal Loads

Length(m)	σ_{crit}(MPa)	P_{max}(MPa)
9.0	11.8	4.5
6.3	23.5	9.3
4.45	47.1	13.6
1.26	568.0	9.5

Case: Actual Recircularization with Thermal Loads

Length(m)	σ_{crit}(MPa)	P_{max}(MPa)
9.0	11.8	7.3
6.3	23.5	18.9
4.45	47.1	45.6
1.26	568.0	203.1

The deflection analysis with no thermal loads showed that the truss maintains its structural rigidity with minor deflections. The maximum deflections occurred at the two nodes which connect the mirror to the main truss. These deflections were 1.86 mm and 1.67 mm. All other deflections were of the magnitude of 1 mm or less. For the case with thermal loading, the deflections were much greater. The members not protected from the mirror radiation had a magnitude of deflection on the order of 10^{-2} meters. This is not enough to disrupt the optical train, though. The maximum deflections of 3 cm occurred for members attached to the hydrogen fuel tanks which does not affect the transfer of energy to the laser engine.

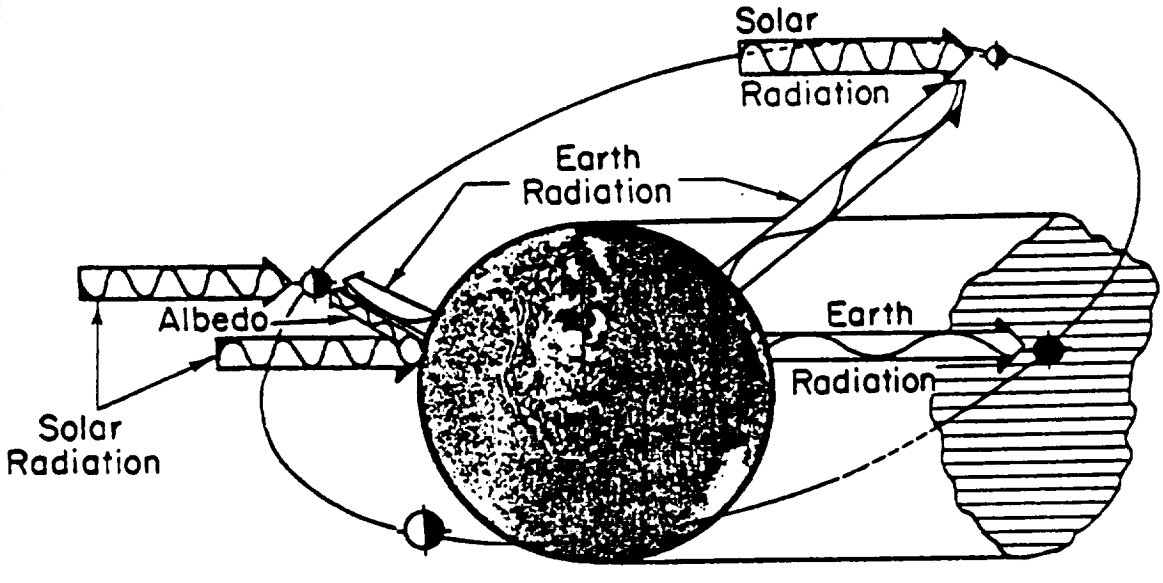

Figure 31. Thermal Contributors

Laser Rocket Basket Design

The LOCOST vehicle was designed to have the laser rocket thrust through the longitudinal axis. As fuel is consumed and the longitudinal centroid moves, the laser rocket must move. For this purpose, multi- directional thrusting rockets are needed. Since the laser rocket cannot be gimballed like the chemical rockets, another method to align the line-of-thrust with the center of mass was sought. A moveable rocket basket was designed to meet these criteria (Figure 32).

The longitudinal center of gravity moves a total 3.3 m from one extreme to the other, which is from full fuel tanks, full payload to empty fuel tanks, no payload. The laser rocket is mounted in a one meter cubed truss. The truss is moved using linear actuation with rubber friction wheels which roll along a truss member (Figure 32). The normal force between the wheels and the shaft must be kept large in order to maintain sufficient friction for movement. The force is generated using high tension springs connected to the axles of the rubber wheels (Figure 32). Natural rubber was chosen over other elastomers for these wheels. Although rubber does not have a large operating temperature range, it maintains its mechanical properties within its mechanical properties best within its range.

Table 26. Material Choices for Actuator Wheels

Material	Operating Range (°K)	Radiation Resistance	Important Properties
Natural	220-350	highest	good mechanically, durable in space
Silicone	190-560	poor	brittle, undergoes rapid degradation in compression, excellent heat resistance
Butyl	230-420	lowest	softens until becomes tarry fluid at high rad.

The inertial load of the vehicle is kept off the axles of the friction wheels with titanium rings. These rings are connected to the basket joints. The inside of the rings carry all the normal force. The rings are lined with molded nylon to reduce friction and abrasion to the shaft track. The total force of the laser rocket (768 N) is distributed over the four rings. The rocket basket makes its trip of 3.3 m over the entire trip time. The power required to move this basket comes to less than 10^{-3} Watts. The short analysis is given below.

$$P = F \times V$$

$$F = \mu_k \times N$$

Where μ_k is the coefficient of kinetic friction, N the laser rocket thrust, and V is 3.3 m/s (10 day trip time). The power required is 3 Watts.

This work is generated by electric actuator motors which are powered by the main fuel cells. The motors are connected to the rocket basket using aluminum bands attached to truss members with an epoxy bonding.

Cargo Bay

The cargo bay is designed for loading and detaching convenience. It is completely removable from the main space frame (Figure 33). Not only does this allow for the cargo to be dropped off quickly and easily, but the discarded truss can be used in the erection of a GeoShack. The vehicle is also not restricted to the single cargo configuration that is depicted in this report. It can carry any

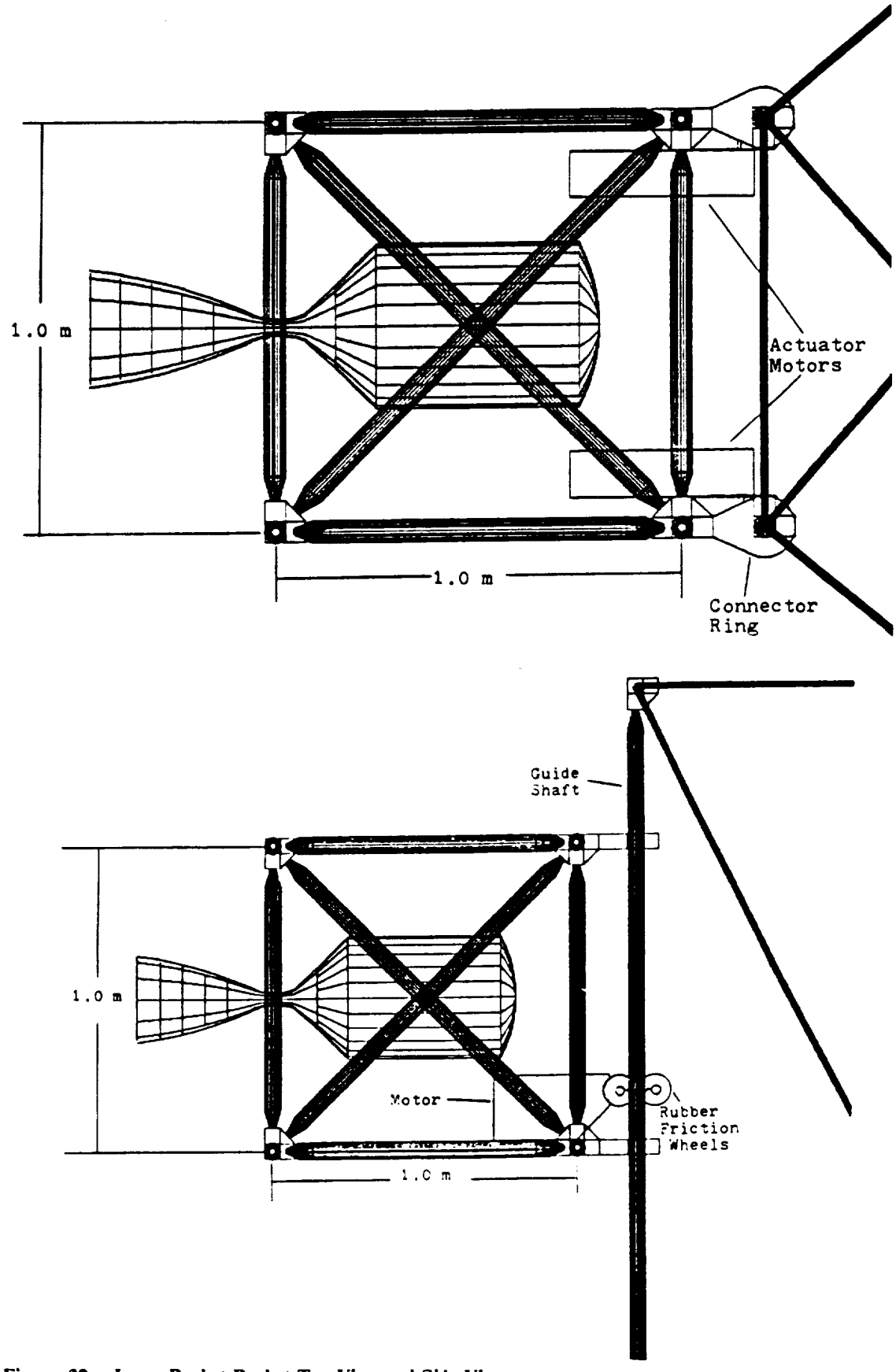

Figure 32. Laser Rocket Basket Top View and Side View

payload that can be attached to nodes and and which does not change the center of mass past certain bounds determined by the gimballing of the chemical engines.

The payload is stored in a cylindrical shell cargo bay which is mounted in a 18.9 m × 6.3 m × 6.3 m rectangular truss frame. In addition, the entire cargo truss being removable, truss members can be removed from the end so that the cargo bay cap unlatches and the payload can be unloaded. The cargo bay could then be reloaded and returned. The entire cargo truss with cargo shell need not be left behind at the GeoShack.

The longitudinal axis of the cargo bay is mounted transverse to the acceleration of the vehicle. Referring back to the materials table, magnesium alloy (8.5% Al) displayed the most desirable properties for construction of the cargo container. It can sustain the largest transverse loads and has a low density resulting in considerable mass savings. The shearing stresses on the walls can be greatly reduced using stringers which run along the longitudinal axis of the cylindrical shell. The wall thickness of the shell can be very thin with the use of stringers, because the stringers will carry the bending and shear forces. With a wall thickness of 2 mm and eight stringers (Figure 34), the cargo bay is capable of supporting the maximum payload of 40,000 kg. The only drawback of using Mg/Al is that it has low tolerance to the space environment. The outgassing losses are greatly reduced by applying a barrier coating that is only a few molecules thick of a material with a much lower evaporation rate (Ref. Parcel). As discussed earlier, aluminum used as protection against the space environment is suitable for this purpose.

The cargo bay has three Mg/Al hoops bonded to its outside. These bands have integrated nodes that are aligned with the titanium nodes used to assemble the surrounding truss frame. These nodes connect the cargo shell to the cargo truss.

Table 27. Mass Savings for Cargo Container

	Density (kg/m³)	Mass (kg)	% Savings
Mg Alloy	1800	1550	33.6
Bo/Al	2490	2150	8.1
Al	2710	2340	0

The attachment planes on the titanium joints need a supplementary latching device (Figure 35) to make the connection complete. The cargo attachment devices (CAD) are not autonomously operated, but they are simple enough to be actuated by robotics or the gloved hand of an astronaut. The CAD is a completely separable piece but can be left attached to either mating joint. It has a button, which when pushed, disengages the bearings that kept the CAD from rotating. To unlatch, the button must be pushed so the CAD can be turned 90 degrees in either direction. There are eight mating nodes between the main truss and the cargo truss.

Docking

The docking mechanism has the versatility to dock anywhere. This is done by limiting the number of interfaces, one being the smallest but more than one offering greater stability once locked in. The docking mechanism uses a modified CAD with an extra device for absorbing the shock of docking (Figure 35). These damping CADs are mounted on the eight joints of the corners of each 6.3 m square (Figure 33). This provides the flexibility to dock at a space station by latching on with any or all of the nodes of the visiting LOCOST vehicle.

A system is also needed to measure the distance and closing speed between the space station and the approaching vehicle. Two common methods for measuring range and range rates are laser and radar devices. Unfortunately, they both cause damage to the object to which the distance is being measured. The radar also has a limited minimum range. For these reasons, a range and range rate system was invented that would be suitable for docking and closing maneuvers. The video controlled solid state range finding system designed by Russell, Graham, and Epperly requires no radar or high power laser, has an effective range from less than a meter to thirty meters, and needs no sophisticated target on the object to which the distance is measured.

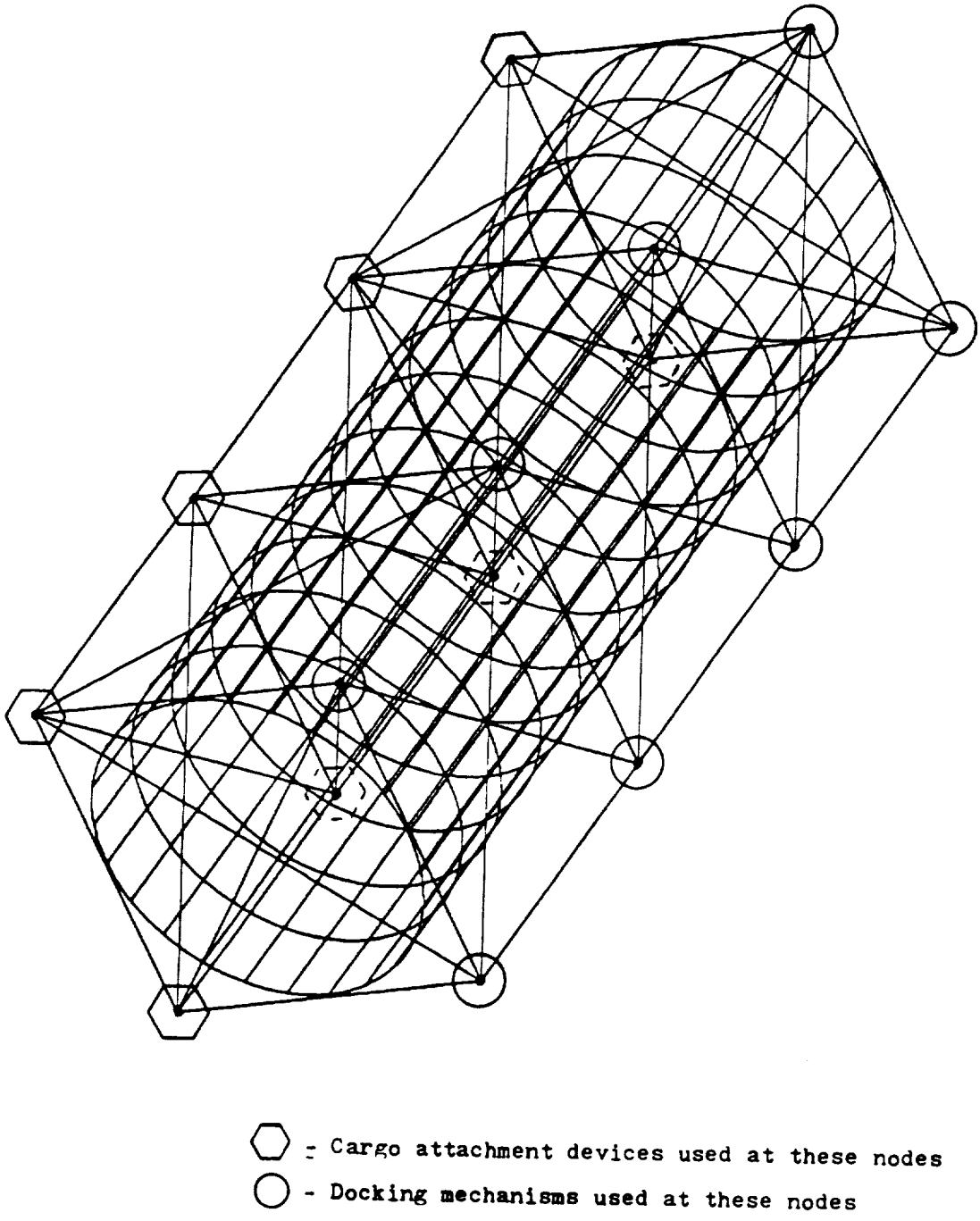

Figure 33. Cargo Bay

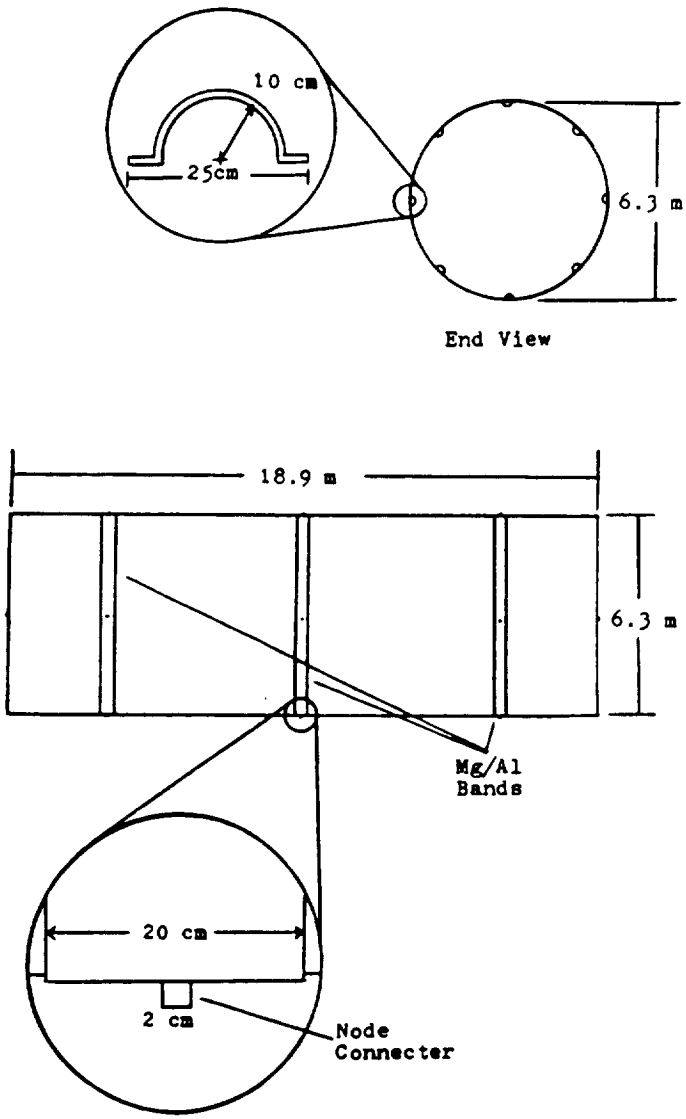

Figure 34. Cargo Bay Stringers

The system has an opto-electric camera and a helium neon laser which emits a source beam of coherent light. This light travels through a beam splitter which sends a reference beam back to the camera and sends an outgoing beam to the first angularly variable reflector which is then redirected to the distant object. An incoming beam is reflected from the object to the second angularly variable reflector which directs the incoming beam to the opto- electric camera by way of the beam splitter. The first and second reflectors are set up so that the distance D travelled by the outgoing beam from the beam splitter and the first reflector is equal to the distance travelled by the incoming beam from the second reflector to the beam splitter. The reference beam produces a reference signal in the geometric center of the camera. The incoming beam produces an object signal at the camera. The difference between the reference signal and object signal is used by automatic means to vary the angle A between the outgoing beam from the first reflector and the reference line between reflecting points of the first and second reflectors and the angle B between the incoming beam from the second reflector and the reference line. Angles A and B are kept equal. The difference between the reference signal and object signal is then used as input by a rotator driven circuit to change the angles of the first and second reflectors until the reference and object signals are coincident. The Range R can then be found by $R = D \tan(A)$ (Ref. Graham).

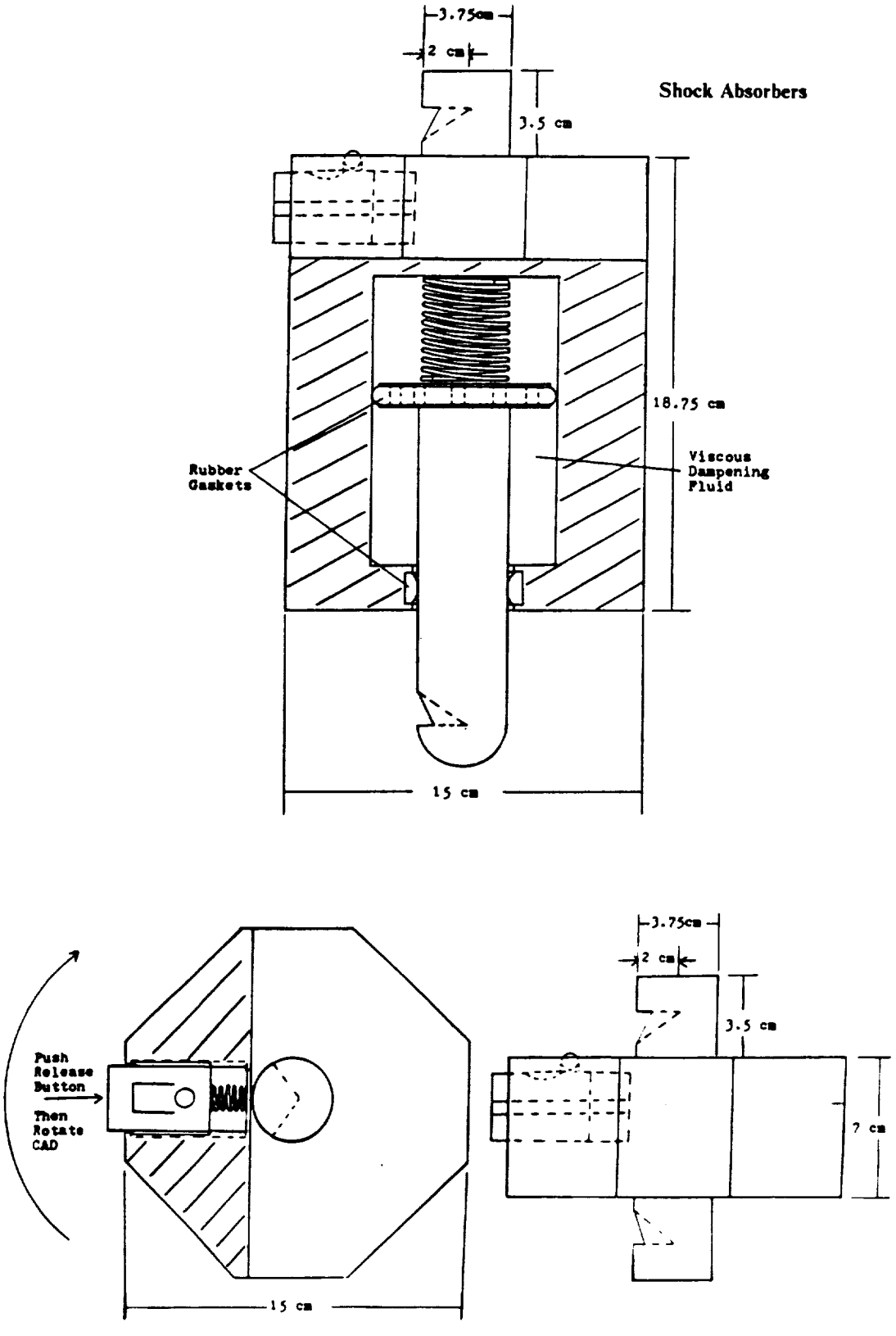

Figure 35. Attachment Mechanisms for Cargo Bay Shock Absorbers

Propellant Storage

Introduction

The scheme for the type, number and placement of the propellant tanks is based on the mass of propellants used. For the baseline mission, the total mass of oxygen required is 40,230 kg and the mass of the hydrogen required is 52770 kg. The vehicle configuration requires that the tanks fit in a fixed truss section of 6.3x6.3 m. Considering the restrictions put on size, spherical tanks were chosen for the oxygen and cylindrical for the hydrogen. The hydrogen tanks have a 6.3x6.3x12.6 area to fit into.

Tank Material

The material chosen for the tank skin is an aluminum alloy. It was chosen based on its high specific strength, high stiffness, low density, availability, low cost, and superior cryogenic toughness. A comparison to another common alloy is shown in Table 28.

Table 28. Comparison of Aluminum Alloys

Metal	AlCu Alloy (2219 T87)	AlLi Alloy (2090 T8E41)
Yield Strength (N/mm^2)	370	535
Ultimate Strength (N/mm^2)	440	565
Young's Modulus ($\times 10^5 N/mm^2$)	0.72	0.758
Density(g/m3)	2.82	2.55

The specifications for each individual tank are calculated in Appendix D. Relevant information is shown in Table 29.

Table 29. Tank Data

	Diameter (m)	Thickness (mm)	Mass(Shell-kg)	m (fuel-kg)
LOX	3.23	.067	5.6	20,115
LH2	5.3	0.135	138.62	26,384

The pressure maintained inside the tanks is predetermined to be 34.475 kPa. This is the lowest practical pressure that still provides a net positive suction head at the pump inlet. A NPSH is required to avoid cavitation at the outlet of the tank. This pressure is also desirable because it is above the triple point of cryogenic fluids.

The tank interior is designed to support slosh baffles and a liquid acquisition device. Some of the schemes examined to expel the cryogenic liquid in a zero g environment were to use the RCS, a wick, or a liquid acquisition device. The RCS scheme maneuvers fuel into the correct position to be siphoned out. Such a system was judged to be impractical for our vehicle. The use of a wick to absorb the fuel and lead it to the outlet was also discarded because of lack of sufficient information. The liquid acquisition device was finally selected. A stainless steel 325x2300 mesh is used. The most efficient way to provide total communication of the liquid is to use a device composed of individual flow channels. The channels are bolted to the wall with non-metallic, teflon spacers.

The cylindrical configuration uses four vanes. The operation of the device depends upon the interaction of the liquid/gas interface with the device. The device is configured to provide gas free expulsion of the fluid. The mass of the liquid acquisition system is approximately 300 kg for each oxygen system and 500 kg for the hydrogen.

The oxygen tank has an 800 micron screen at the exit to screen out impurities caused during storage. The hydrogen tank has a 400 micron screen. Hot wire sensors are used for loading control logic. Vent and relief valves in the nose cap of the tanks provide for gaseous propellant vent capability and for relief protection. Ullage transducers are used by the actuation of control valves to control ullage pressure in flight. Three to five percent space is left for ullage. The tanks stretch as a function of static head and shrink when the cryogenic liquid is loaded. (See Figure 36)

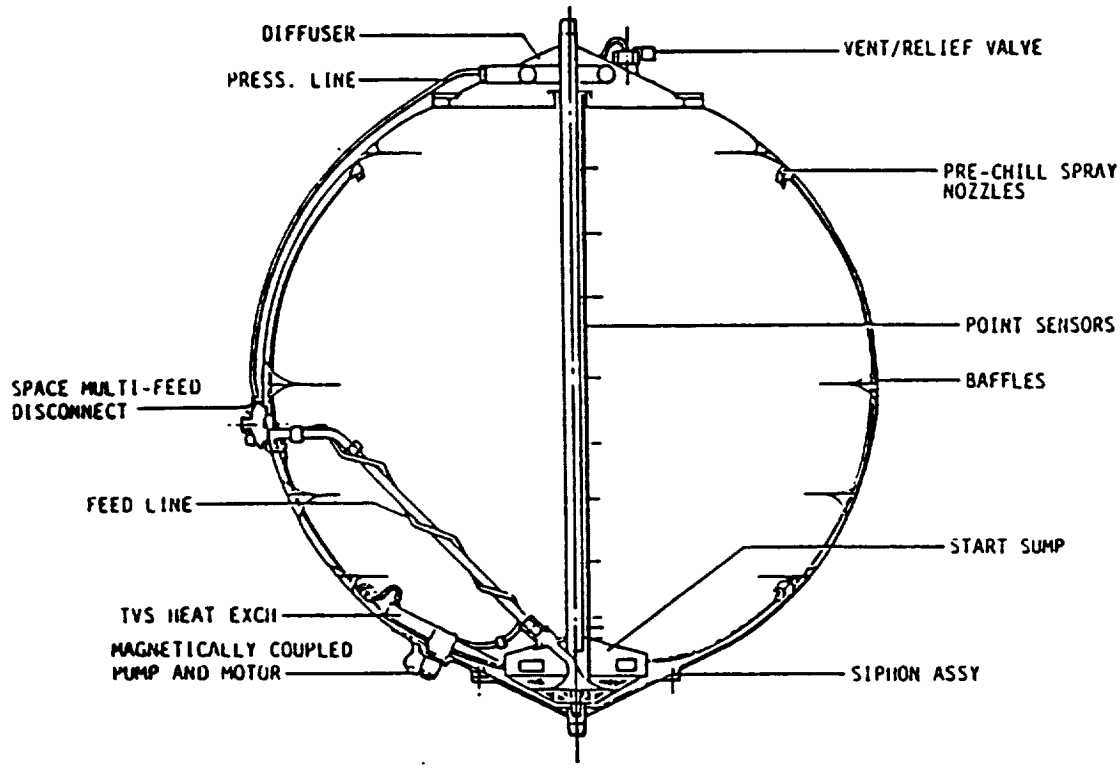

Figure 36. Spherical Oxygen Tank

Tank Insulation

The insulation chosen was a multi-layered insulation (MLI) layered with foam. This scheme has the lowest density and has proven to be a capable insulation scheme. The MLI is composed of alternating layers of metallized Kapton film and Dacron net spacers. Between the MLI and the foam is a gas-impervious aluminized Kapton barrier film which is bonded over the inside wall of the foam to keep degradation factors from reaching the MLI. The foam used is Rohacell 31. A comparison to other foams is shown in Table 30. Rohacell 31 is superior in performance. It is manufactured in sheets which are heat formed to the tank, then adhesively bonded to the surface using vacuum bagging. A layer of paint follows the insulation. The paint is silicate bonded and contains zinc othotitanate pigments (Zn_2TiO_4). An 8 mils thickness of YB-71 is then applied for reflectivity. A final layer of mylar is applied to protect against micrometeorites.

Table 30. Foam Comparison

Type	Material	Density (kg/$m3$)
Rohacell 31	Polymethacrylimide	30
Stephan Foam (BX25OA)	Polyurethane	37
CPR 488	Polymetirc Isocyanate	36

A picture of the insulation and a summary of the characteristics are shown in Figure 37 and Table 31, respectively. The outlet of the tanks is a contoured non-drop-out configuration with anti-vortex baffles at the exit.

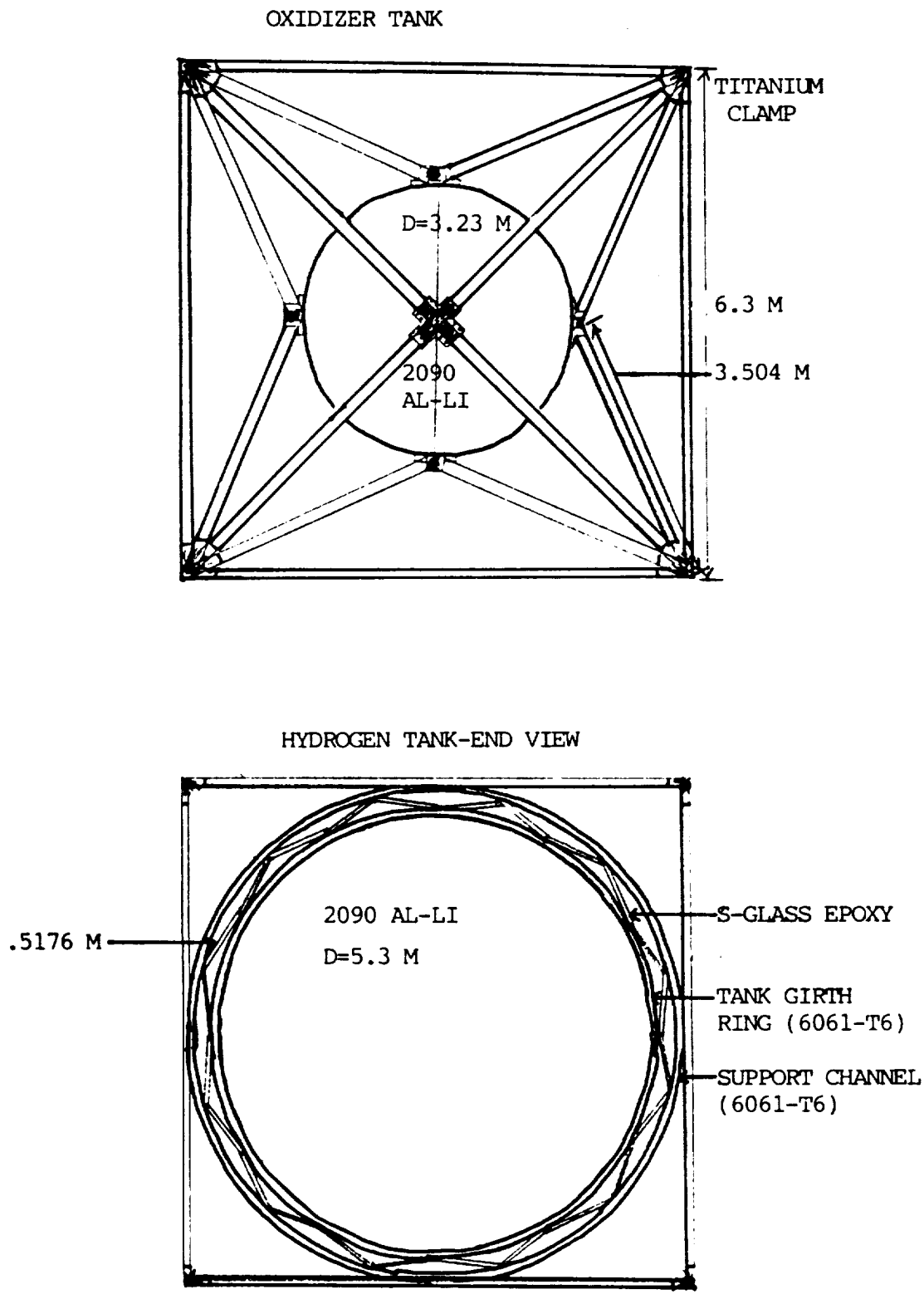

Figure 37. Insulation

Table 31. Insulation Summary

Qvf(W) = Venting Heat Flux
Qsr(W) = Solar Radiation Heat Flux
Ts(K) = Temperature On Tank Surface

	Qvf	Qsr	Ts	t(MLI-cm)	t(Foam-cm)	m (total-kg)
LOX	23.62	1374	196.9	1.86	.186	46.46
LH2	64.91	16901	196.49	1.86	.186	570.98

Tank Support Structures

The support structures for the tanks are made of composite materials. A comparison of basic composite materials is shown in Table 32. The structures used were chosen to minimize boil off from thermal conduction of heat to the tanks.

Table 32. Comparison of Composite Materials

	Ultimate Tensile Strength (MPa)	Modulus of Elasticity 10^6 KPa
S-Glass	1680	46.2
SP-250-52	1675	46.2
181 E-Glass	827	41.4
Optimum Composite	334	42.8
Lay-Up OF S-Glass/E-Glass	334	42.7

The spherical symmetric oxygen tanks have S-glass epoxy members attaches to the tank in 6 places. The S-glass attach to a graphite- epoxy frame which fits inside the basic truss. The frame is attached by titanium clamps.

For the hydrogen tanks, three 6061-T6 girth rings attach to 24 S-glass epoxy members which in turn attach to three 6061-T6 ring support channels. The ring support channels have longeron trunnion fitting interfaces which attach the whole structure to the main truss. The support structures are shown in Figure 38 and Figure 39. Mass breakdown of the tank support structures is given in Table 33.

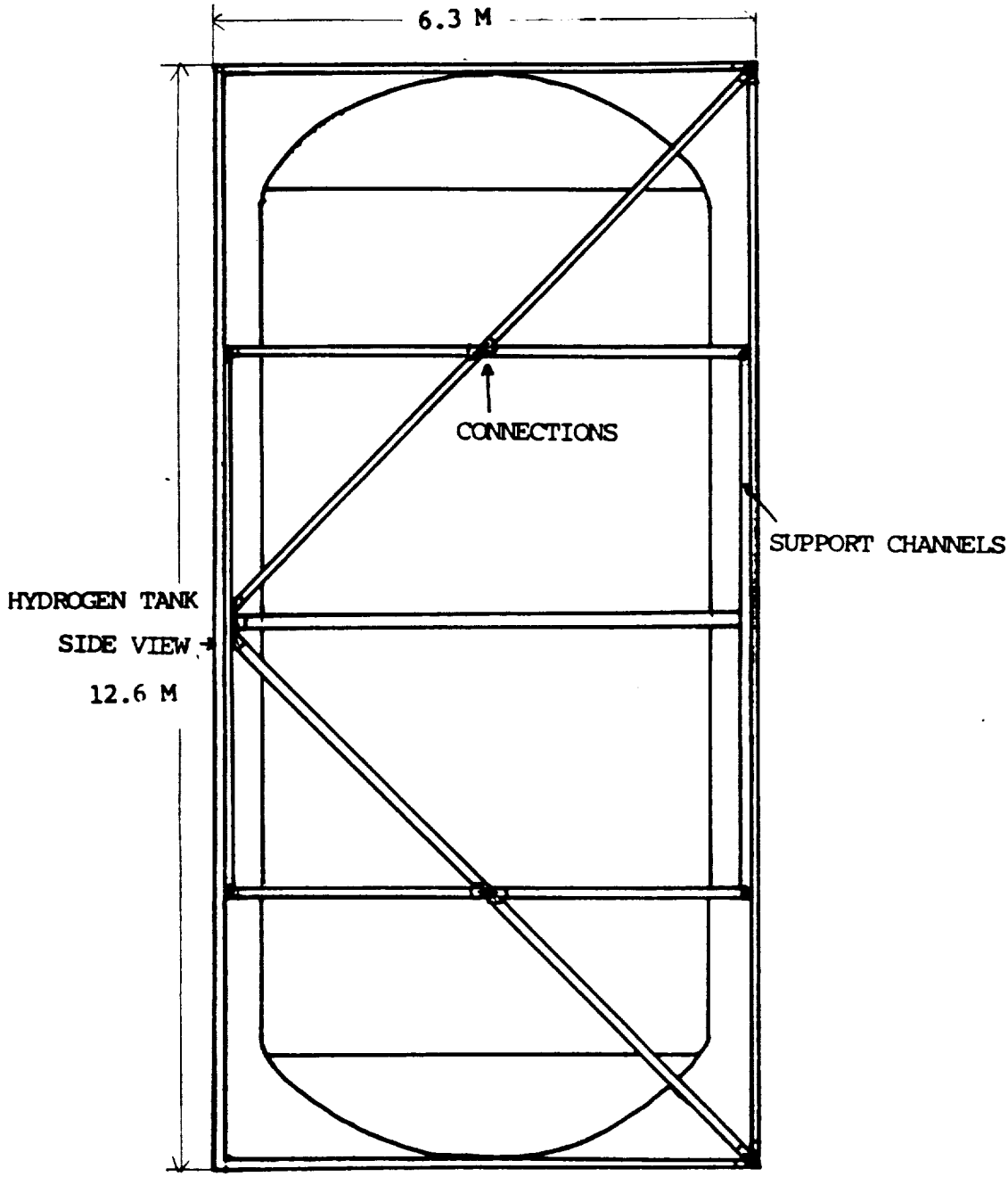

Figure 38. Propellant Tank Support Structure 1

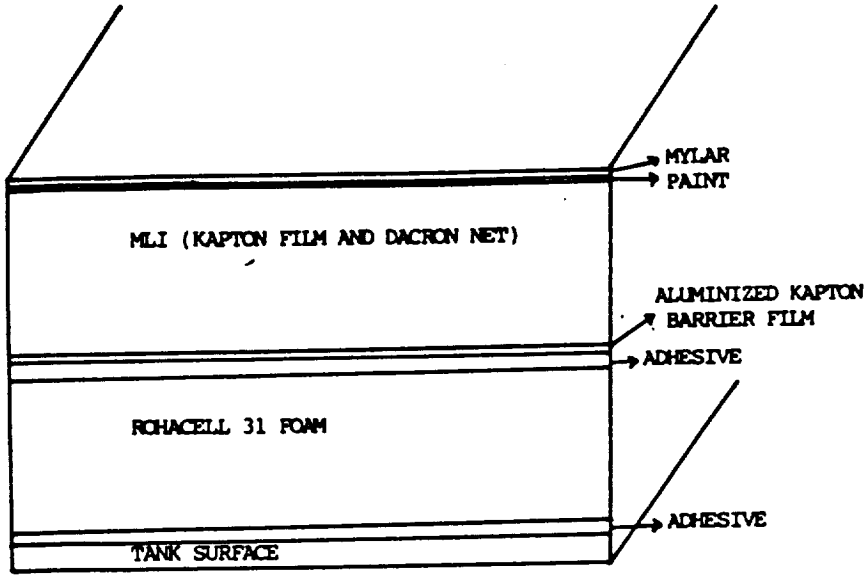

TANK CROSS SECTION

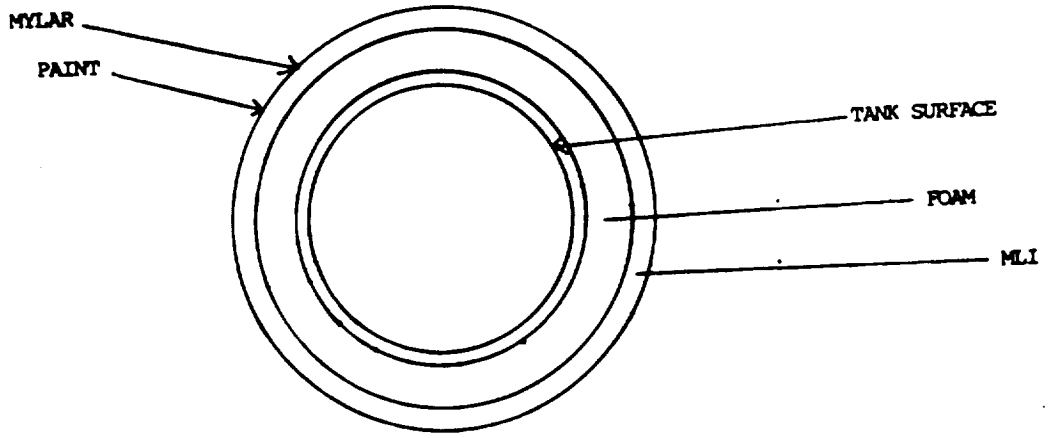

Figure 39. Propellant Tank

Table 33. Mass Breakdown of the Tank Support Structures

Oxygen-Spherical

	Density (kg/$m3$)	#			Mass (kg)
S-Glass/Epoxy	2490	24			601
Total Mass					601

Hydrogen-Cylindrical

	Density (kg/$m3$)	#			Mass (kg)
S-Glass/Epoxy	2490	24	.7	.5176	241.29
6061-T6	2550	6	1	19.761	94.98
6061-T6	2550	6	1	18.2	87.433
Total Mass					397
Total Support Mass					1996

Propellant Pumps

Electric pumps used to transport the oxygen towards the engine weigh 40 kg and require 1.04 kW. The Δp required for the oxygen is 1.9 MPa and that for hydrogen is 7.2 MPa.

The fluid flow lines have a total mass of 150 kg and are made of aluminum with insulation. Table 34 contains the diameters of the outflow, inflow, and pressurization flow lines for the oxygen and hydrogen tanks.

Table 34. Fluid Line Diameters

	Outflow (cm)	Inflow (cm)	Pressurization (MPa)
Oxygen	9	6	1.5
Hydrogen	5	6	4

Dynamical Control System

Introduction

A vehicle largely dependent on an incident power beam must have precise and accurate attitude control. For over 15 years, momentum storage devices have been successfully used to rotate space vehicles. Possible momentum storage devices are summarized in Table 35.

Table 35. Possible Momentum Storage Devices

- Fixed Momentum Wheels
- Reaction Wheels
- Gimballed Momentum Wheels

While these momentum storage devices all provide rotational ability, they are subject to saturation limits. When they become saturated, a non-conservative device such a gas-jet must be used to return the system to the initial state where it can, once again, receive angular momentum. This feature does not subtract from the great strength of the devices, which is the ability to store large momenta, and hence, instigate a high attitude stability.

To supplement the "flywheel" attitude control devices, a reaction control system (RCS) is utilized. A RCS is composed of small thrusting, low I_{sp} rockets. There are other methods of desaturizing the momentum storage devices, such as magnetic torques and gravity-gradient torques. The space station will use gravity-gradient torques (Wie, Byun et all). But these methods are too complex and not appropriate for the relatively small size of the LOCOST vehicle, hence an RCS will be employed.

The Hubble Space Telescope employs reaction wheel assemblies with integrated desaturation torquers and small direct drive motors to negate the effects of secular torques (see below). Additional study of this system could yield a scheme that is superior to the RCS system discussed below (Sevaston et al). Of course, a RCS system would still be needed for docking.

Discussion of Gyro Technology

A schematic of the vehicle's body centered axis is shown in Figure 40. This body axis orientation will be used in the remainder of the chapter. With this reference system, the yaw rate is rotation about the x-axis, slew rate about the y-axis, and the roll rate about the z-axis.

The most significant low frequency disturbances affecting spacecraft are summarized in Table 36 (Lademann).

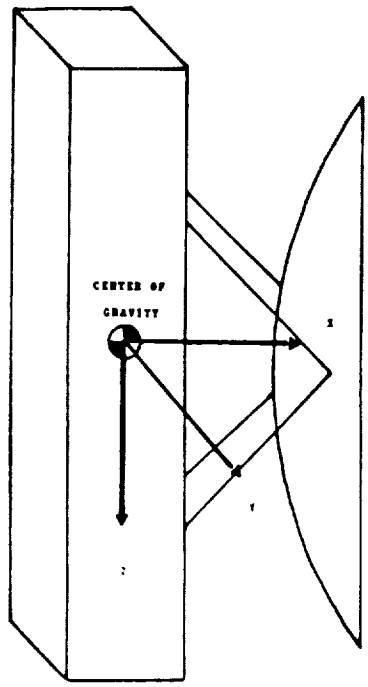

Figure 40. LOCOST Vehicle's Body Axes

Table 36. Low Frequency Spacecraft Disturbances

- Gravity-gradients
- Aerodynamic (especially near LEO)
- Solar radiation pressure
- Miscellaneous cyclic disturbance torques

Unless counteracted, these torques would cause the vehicle to tumble. Mass expulsion devices can be used to counteract these torques, but these methods suffer the obvious disadvantages of extra mission mass and mechanical accelerators. Momentum-exchange devices, such as flywheels and CMGs, utilize a recoverable (electrical) energy source to maintain the vehicle's attitude.

Some of the tradeoffs associated with different momentum exchange actuators are summarized in the Table 37 (Lademann). In this table the following acronyms are used: RWA for Reaction Wheel Assembly, SGCMG for single gimbal CMG, DGCMG for double gimbal CMG.

Obviously, pointing and tracking are a high priority, however as can been seen in the table, some desirable attributes are conflicting. Tolerable compromises of performance must be made with the intent of minimizing the impact on the design of any one particular parameter.

Note that the fixed momentum flywheel (RWA in the table) suffers the disadvantage of not being able to completely transfer its momentum to the vehicle. Gimballing of the flywheel offers the possibility of total momentum exchange between vehicle and flywheel (Schulz & Lange).

Some of the pros and cons of attitude control with momentum exchange devices are summarized in Table 38.

Table 37. Tradeoffs for Different Momentum Exchange Actuators

Device or Parameter	RWA	SGCMGs	DGCMGs	Comments
Hardware Complexity	Least	Intermediate	Most	RWAs require only speed control circuits. CMGs require additional gimbal servos
Control Law Complexity	Least	Most	Intermediate	RWAs usually require pseudo-inverse steering law. DGCMGs have few singularity problems while SGCMGs have severe internal singularity problems.
Torque Capability	Least	Most	Intermediate	RWAs require large power for high torque. DGCMGs transmit torque through tourquers and gear train while SGCMGs transmit torque directly vehicle.
Momentum Capability	Least	Most	Most	Generating torque by changing wheel speed at high speed requires excessive power.
Pointing Accuracy Capability	Most	Intermediate	Least	Since RWAs are not gimballed, torque is controlled more precisely. However, hardware anomalies associated with momentum exchange devices are usually not the main contributors to pointing errors since rate sensors close the loop around actuator errors.

Table 38. Main Points with Momentum Exchange Devices

- Momentum exchange devices may be control momentum gyros (CMGs) or reaction wheels (RWAs)
- Control System Reacts to External Disturbances Continuously
- High pointing accuracy is possible
- Momentum exchange device stores integral of external torques
- Since external torques have bias components, stored momentum tends to grow, leading to saturation
- Saturation of RWAs is reached at maximum wheel speed
- Saturation of CMGs is reached when momentum vectors are pointing in the same direction

Lademann offers three heuristics when selecting a momentum exchange device. They are summarize in Table 39.

Table 39. Momentum Exchange Device Selection Heuristics

1. Use RWAs if torque and momentum requirements are within RWA's capability.
2. Use SGCMGs when very large torques are required.
3. Use DGCMGs for large space structures with moderate torque requirements when momentum storage requirements may increase as additional modules are added.

The last selection criteria in Table 39 is the most important for the LOCOST vehicle because of the extra side propellant tanks to be added to the structure of the vehicle to fulfill the maximum cargo scenario. Hence, double gimballed CMGs will be used. Also, these tanks will cause large moments of inertias which must be counteracted by larger torques. As seen from Table 37, they suffer the disadvantage of being more complex and sustaining the lowest pointing accuracy capability. It is assumed that by 2010 the DGCMGs will have increased their pointing accuracy. The DGCMGs are housed in metal boxes roughly 1 m on a side. Gimbals are essentially large boxes with the rotor inside.

Nominally, three double gimballed CMGs are needed to provide rotation about all three body axes. If more than one plane of symmetry had existed, it would have been possible to reduce the number of CMGs. Each of the CMGs has an inner and outer gimbal ring. The outer ring allows rotation about the angular momentum vector, while the inner ring allows a precession of the rotor axis about the inner gimbal. The basic principle is that a torque (applied by an electric motor) about one axis causes a precession about a mutually perpendicular axis. Through conservation of angular momentum, the vehicle rotates. The precession rate is determined by the applied torque and the moment of inertia of the vehicle.

While the vehicle rotates, it is necessary to have some feedback of the rotation rate. Possible ways to gain information about the instantaneous angular rate of the vehicle include flywheels, star sensors, and gyroscopes. In most cases, a flywheel is a gyroscope, but the terminology used above was used to differentiate between flywheel technology and more advanced gyroscopes such as ring laser gyroscopes and fiber optic gyroscopes. Although the need for a star sensor will be established independently of the CMGs, the star sensor will not be used to obtain angular rate information.

As a final note on high accuracy pointing applications of which the LOCOST vehicle is one, a control law that is highly insensitive to errors must be used. Derivation of the control laws is an important step in the implementation of the CMGs and overall dynamical control.

Discussion of Gyroscopes

Gyroscopes give angular rotation information. There are many ways to implement a gyroscope, three of which will be presented.

Flywheel gyroscopes have the advantages of low noise, analog output, long life, high reliability, and extremely low bias. The flywheel suffers numerous disadvantages. Recent advances in gyroscope technology renders the flywheel gyroscopes obsolete.

Ring laser gyroscopes (RLG) appeared in the late 1960's (Lademann). RLGs do not have spinning flywheels, but use lasers and the time of travel between two points to determine angular acceleration. RLGs contain an optical cavity with mirrors at each corner. A shining incident laser is split into two beams. The beams are then collected at photocells after reflecting off the mirrors. During angular rotation, an apparent difference in path length is developed between the two beams. This directly translates into a frequency shift which can be detected. A fringe pattern created by the in-

terference of the two beams, one shining through partially silvered mirrors, yields directional information, while the frequency shift yields scalar angular rate. RGLs do suffer lock-up rate, a condition during low angular rotation rates that cause poor accuracy. Also, mirror surface erosion, outgassing of materials within cavity, path length control precision and mirror optical axis stability make RLGs an unsuitable choice.

A new type of gyroscope offers the potential for eliminating many of the problems associated with RLGs (Stokes). The Fiber Optic Gyroscope (FOG) is the newest generation of rotation sensor being developed. Both Bendix and Sperry have produced prototypes. The FOG has the advantage of the complete absence of moving parts. Basically, the FOG is a non-resonant ring interferometer. Only solid-state technology and fiber optics is used. This assures long life, high reliability and better performance. A semiconductor diode provides the laser light. The FOG uses a multi-turn fiber loop--sometimes over a kilometer of fiber. The longer the fiber path the better accuracy and precision. Rotation of the FOG causes a phase shift between counter-rotation light waves. The phase shift is given by the relation

$$\Delta\psi = \frac{2\pi DL}{\lambda c}\omega$$

With $\Delta\psi$ = optical phase shift
D = loop diameter
L = fiber length
λ = wavelength of light
c = speed of light
ω = rotation rate

A schematic of the FOG is shown in Figure 41. Also, the main advantages of the FOG are summarized in Table 40.

Table 40. Advantages of a Fiber Optic Gyroscope

- High reliability (no moving parts)
- Low environmental sensitivity (high-g applications)
- Low cost (no critical machining or assembly operations)
- Small size and weight ($\simeq$ 1 kg.)

FOGs are not yet perfected. In fact, they suffer from more noise then their mechanical counterparts. It is expected, however, that by the projected year of the LOCOST vehicle, FOG technology will have been reached a sufficient level to justify its use. The FOG requires 3 Watts per axis measurement and uses only low frequencies (Stokes).

Specification of CMGs

Specification of the CMGs requires the determination of angular rates, vehicle moments of inertia and the placement of CMGs relative to the the center of gravity (CG). If the CMG is not placed directly at the CG, inefficiencies occur. It is assumed that there is a 100% efficiency of momentum transfer for the following analysis. Angular rate information was obtained from the orbital mechanics calculations. The angular rotation rates were determined trigonometrically from vectors from the vehicle to the LPS and the desired angular attitude relative to the body fixed axis system. The torques necessary to generate the precessions are determined by multiplying the axes' moments of inertia and the angular acceleration required to achieve the desired final angle. The values for the moments of inertias used are summarize in Table 41.

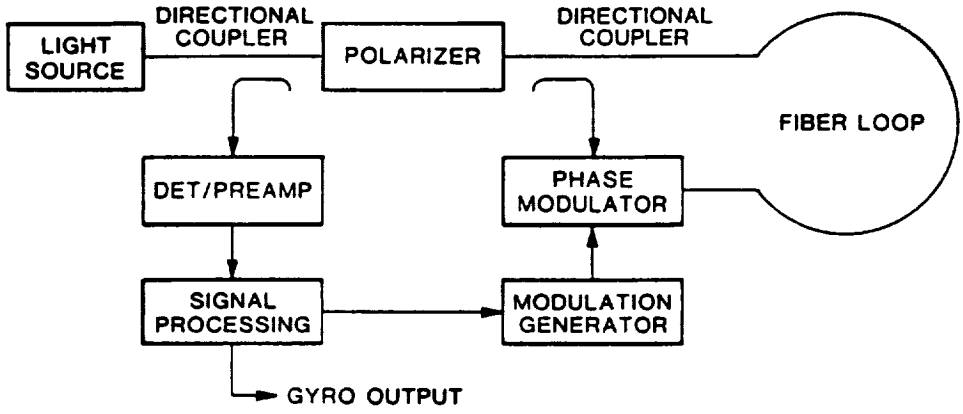

Figure 41. Fiber Optic Gyroscope (FOG) Schematic

Table 41. Moments of Inertia

Moment Type	Value ($\times 10^6$ $kg - m^2$)
Ix	.9
Iy	1.2
Iz	1.7

The maximum precession angles of the gyros and the angular rates that were used are summarized in Table 42.

Table 42. Maximum Precession Angle of Gyros and Angular Rates

$\left(\frac{rad}{sec^2}\right)$	Precession (°)	Angular Rate
Yaw	10	$< 1 \times 10^{-5}$
Slew	60	.001 (nominal)
Roll	15	$< 1 \times 10^{-3}$

In order to satisfy the torques involved a compromise was achieved. The torques needed for two out of the three axes is small compared to the third, therefore an array composed of two CMGs was used to satisfy the higher torque requirements. An analysis of single-gimballed CMG array's momentum envelope topology is performed by Meffe & Stocking. A similar analysis should be done for the DGCMGs because it is possible that the non-linear effects of the CMGs will cause the CMG's momentum contributions to be non-additive. Additionally, the topology should be explored because the arrayed CMGs might produce a surface where no additions of angular mo-

mentum can be stored or transferred. The analysis of such topology envelopes is beyond the scope of this design report. It is assumed that the CMG contributions to angular momentum can be linearly superimposed.

The CMG chosen is a Bendix developed, advanced CMG. It's parameters are summarized in Table 43.

Table 43. Selected Baseline CMG

Parameter	Capability
Wheel Speed	100 (Hz)
Gimbal Rate	2.0 $\frac{rad}{sec}$
Angular Momentum	2400 N-m-sec (minimum)
Rotor Inertia	3.54 N-m-sec^2
Output Torque	4700 N-m (minimum)
Mass	100 kg
Gimbal Rate Command	15 Bits Including Sign
Power (Zero G)	
Quiescent	50 Watts
Peak Power Capability	70 kWatts
Size $\cong$ 1 m on a side.	

The differences in the above specifications and those given by Lademann are due to predicted technology advancements. Figure 42 shows the placement of the CMGs on the LOCOST vehicle.

Desaturization Rocket System

Only a small RCS system is needed because the vehicle already contains a powerful chemical propulsion system which can account for large orbital corrections. Therefore, only small desaturizations and docking maneuvers must be performed via the RCS.

A 5 N thrust per rocket nozzle RCS system was chosen for the vehicle. Because of the impulsive nature of the RCS system, the RCS should not be used during laser firing because the perturbations developed can cause intolerable and disastrous errors in optical alignment.

For the baseline configuration, a hydrazine powered (oxygen oxidizer) rocket will be used. By 2010, other propellants will be accessible and a conservative estimate for the I_{sp} of the rocket is 260. The use of a monopropellant gives the system simplicity and reliability. Also, the small size of the rocket means that radiative cooling is sufficient. The hydrazine propellant will be stored with the clusters.

Placement of RCS

Clusters of three rockets are attached to each of the eight main corners of the vehicle. Figure 42 shows the RCS configuration chosen. Through this arrangement, it is possible to both translate and rotate the RCS through its three degrees of freedom.

The mass flow rate can be determined for each of the RCS nozzles from,

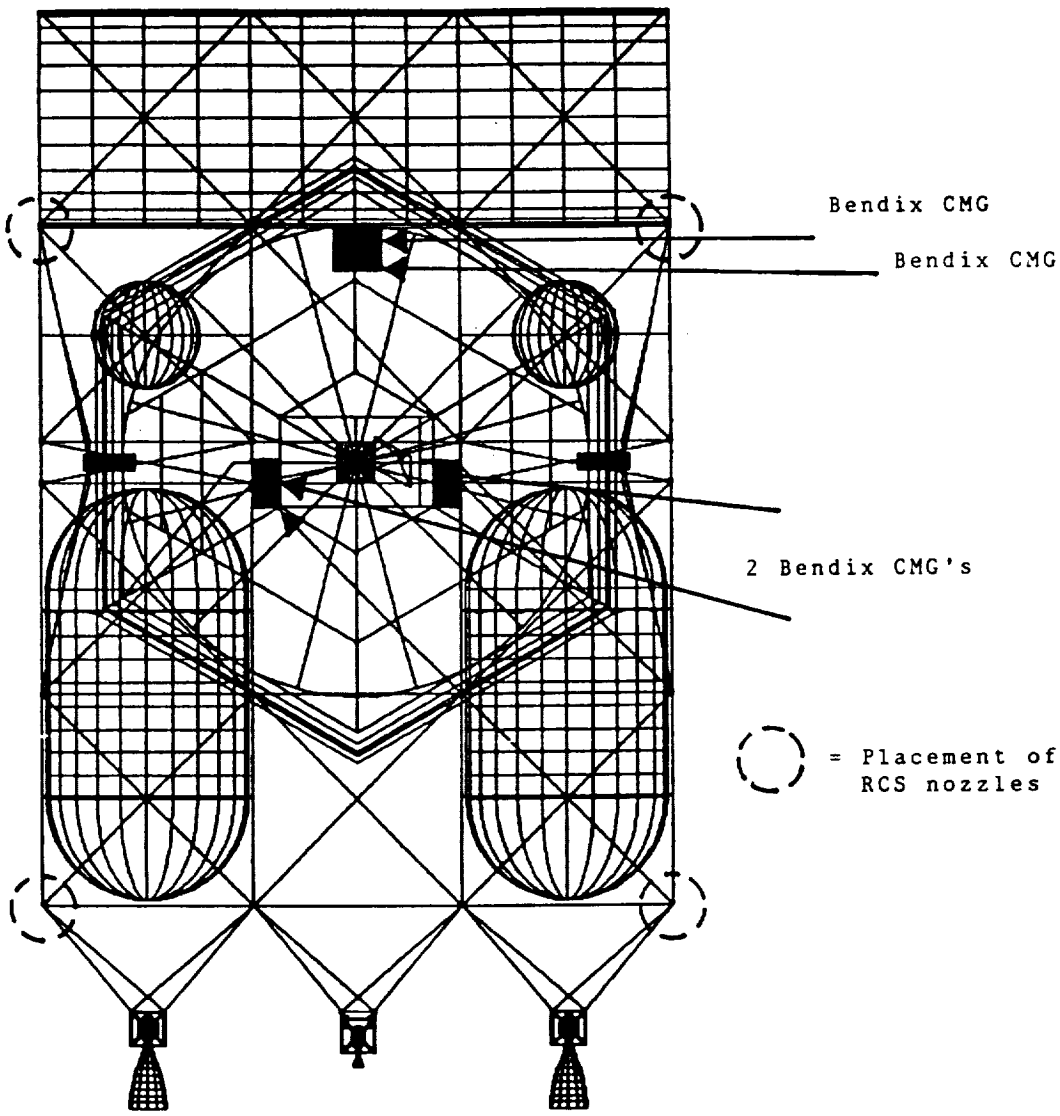

Figure 42. CMG and RCS Placement on the vehicle.

$$\dot{m} = \frac{T}{I_{sp}\, g_e} = .002 \frac{\text{kg}}{\text{sec}}$$

To account for the propellant needed to power the RCS for the baseline mission, it was assumed that desaturization could occur over a period of 800 seconds. This corresponds to the period in an orbit where the LPS is located. During desaturization four engines would burn. For the baseline mission, it is assumed that no more than 15 desaturizations will occur. For this, a total of 100 kg of hydrazine is consumed.

Docking requires the careful manipulation of the vehicle. Because of its large mass size compared to the total possible translational force in any of the three body axes directions, the RCS will need to burn much longer during docking. A ten minute burn per nozzle is assumed for any particular docking maneuver. For docking both at GEO and LEO, two ten minute burns are required. This will consume 2.4 kg of propellant per nozzle. During docking, it is assumed that two directions

of applied force will be needed, hence eight nozzles must fire. For all docking maneuvers then, only 19.2 kg of propellant will be needed. Including a 20% residual, the baseline mission requires 23 kg of propellant. The characteristics of the RCS and CMG system are summarized in Table 44.

Table 44. CMG and RCS Summary

Selected RCS Baseline Summary	
Thrust per nozzle	5 N
Specific Impulse	260 s
Mass flow per rocket	$.002 \frac{kg}{sec}$
Nozzles per cluster	3
No. of clusters	8
Propellant needed for both desaturization and docking in the baseline mission.	123 kg

Acquisition, Tracking and Pointing

Introduction

Acquisition, tracking and pointing is the process of acquiring the laser beam and subsequently continuously tracking it by pointing an antenna towards the beam direction of propagation. Laser powered vehicles require an accurate and dynamic system to insure the reception and control of the power beam. The LOCOST vehicle ATP system must be able to locate and maintain the laser beam link.

Pointing control is also needed to counteract the effect of external disturbances. External disturbances include gravity gradient torques, solar pressure torques, and collector motion coupled through the rotary joint. Also, changes in antenna attitude, thermal loading, aging effects, and structural deflections necessitate dynamic control of the power beam (Ref. NASA CR-3350).

Similar problems with the ATP for satellites have already been addressed in the field of laser communications (lasercom). Much of the design analysis and selection presented in this chapter is based on the design analysis for lasercoms.

The ATP system relies on three other subsystems of the vehicle: the communications system, the control computer, and the RCS & CMG system. The interrelationships are shown in Figure 43. The communication system establishes the initial link between the LPS and the vehicle, from which the entire ATP cycle is initiated. The control computer coordinates the interactions from the ATPs position and attitude demands to the appropriate subsystems. The RCS & CMG system fulfills the position and attitude demands of the ATP. All the systems work in concert.

ATP systems have also been developed for payload-experiments. Experiments often require continuous pointing, but on spin-stabilized satellites, continuous pointing presents many problems. Payload pointing mechanisms are usually employed. The Hubble Space Telescope requires a fine pointing mechanism to continuously track stars. Its system employs traditional techniques of attitude control and attitude determination. Through good design practices, its system is capable of high accuracy and precision (Sevaston et al).

The ATP System

The ATP system is composed of five major components. They are summarized in Table 45.

Table 45. Major Components of ATP System

- Tracking Laser
- Optical Receiver
- Optical Transmitter
- Fine Pointing Gimbal Assembly
- Mirror Alignment System

The mirror alignment system includes alignment control for the primary, secondary and fifth mirrors.

Tracking Laser

There are four types of lasers to choose from for the LOCOST vehicle tracking laser. The tracking laser must be power efficient, low in mass, and resistive to the space environment. The four types of lasers are presented in Table 46.

Table 46. Possible Lasers for the LCOTV

Laser Type	λ (micrometers)
AlGaAs	0.89
Nd::YAG	1.06
doubled Nd::YAG	0.532
CO_2	10.6

The AlGaAs diode lasers are efficient but of low power. Hence, a large array must be used. Large arrays, however, introduce beam-combining problems. Also, these diode laser suffer appreciable wavelength shifts from aging. The CO_2 lasers are reliable, but problems arise due to their sealed

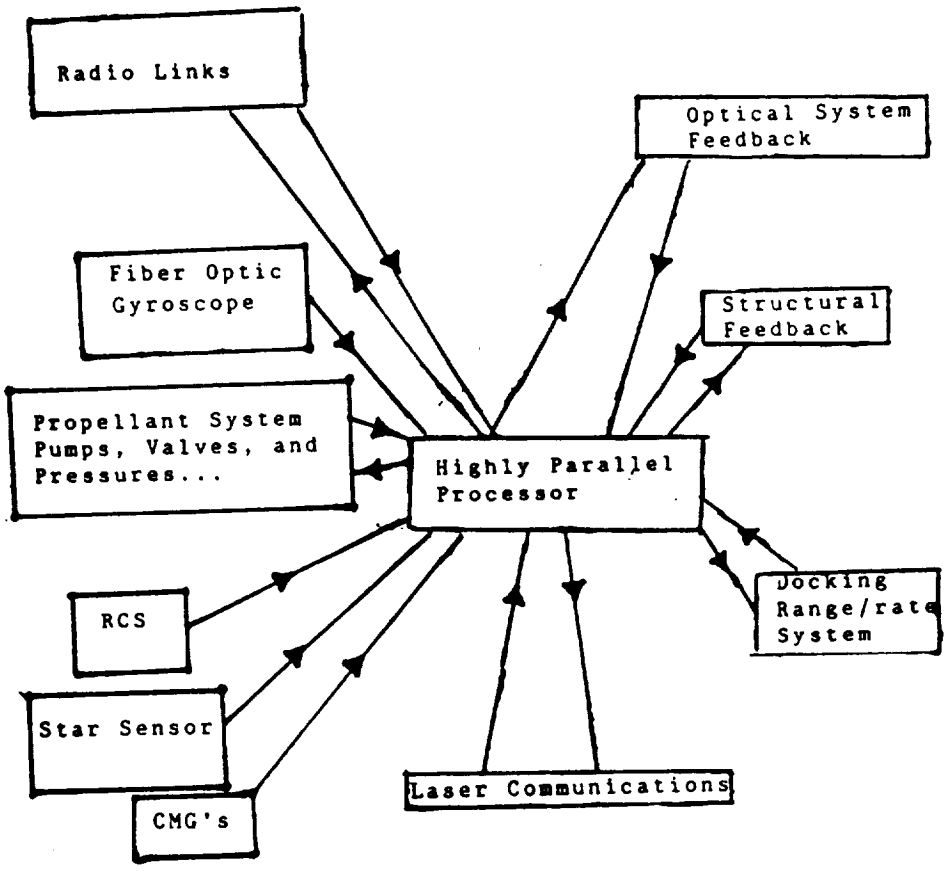

Figure 43. Interrelationships of ATP with Other LOCOST Subsystems

tubes containing the gases. Also, the carbon dioxide laser would need cryogenic cooling equipment. Both of these lasers were dropped from consideration.

The Nd:YAG (Neodymium: Yttrium, Aluminum, Garnet) lasers have become the workhorse laser for lasercom (Ref. Katzman). By using the doubled Nd:YAG laser, a direct detector can be used (discussed below). The Nd:YAG will be pumped with AlGaAs diode lasers. Because of the problems associated with the AlGaAs diode lasers, the design calls for a modular AlGaAs diode array. As the diode lasers suffer age effects, the pumping unit can be replaced with a new one.

The laser power can be significantly reduced by pulsing the beam. Pulsed power is 200 Watts at peak power for 1 microsec. The laser has a maximum of 1000 pulses per second. No modulation techniques are needed because no information needs to be coded into the beam. The presence, absence, or spatial shift of the beam from the receiver communicates the required information.

Optical Receiver and Transmitter

A receiver can utilize an independent antenna or share an antenna with the transmitter. If the receiver and transmitter antenna are independent, added complexity and mechanisms for accurate boorsighting must be utilized to maintain two lines-of-sight. Therefore, the transmitter and receiver will share the same antenna. This realizes a weight and volume savings and allows for easy alignment. However, this approach requires internal optics to separate the two signals. Also, a practical limit on the data transmission rate is introduced (<0.1 Mbit/s), but this does not pose a problem because the tracking system relies on the location and existence of the pulsed beam--not on the information modulated within (Ref. Katzman).

For lasercom, an antenna is actually a telescope. For the LOCOST vehicle, a Schmidt-Cassegrain telescope setup is used. The Cassegrain setup minimizes the effects of pointing jitter and misalignment bias (Ref. Katzman). The system is mounted on a two degree of freedom yoke and attached to a boom. The boom is located at the pivot point of the primary mirror. Figure 7 shows the configuration. Figure 44 shows a labelled schematic of the transceiver.

The telescope has several subcomponents which are discussed below.

The Telescope Shell:(A). The telescope shell is made from lightweight aluminum formed into a cylinder. The cylinder dimensions are 45 cm high with a 40 cm diameter. These dimensions are sufficient to catch a pilot beam from the LPS that has dispersed slightly. This aperture size also makes a sufficiently sized beam at the vehicle, so that a reasonably sized LPS telescope can capture it. The telescope shell is attached to a yoke. The gimbal axis of the yoke and the gimballing of the entire yoke comprise the two degrees of freedom needed for easier pilot beam acquisition. This yoke comprises the fine gimbal pointing assembly.

Both the azimuth and elevation are controlled by induction motors contained within the gimbal assembly. Each motor consumes 12 W of power (Ref. LPIV).

The Dielectric Filter:(B). The dielectric filter is placed over the opening of the telescope to reduce possible environmental damage to the multi-dielectric surfaces (discussed in element F). The filter also reduces the false alarm rate. There were two choices for the dielectric filter: fused silica or BK7 glass (Ref. Katzman). Both have good transmission in the wavelength being used (0.532 micrometers). However, fused silica experiences a significant decrease in transmittance under radiation bombardment. The BK7 glass was chosen.

Polarizing Beam Splitter:(C). The polarizing beam splitter splits a beam according to its polarization. As discussed above, the send and receive beam propagate at the same wavelength but have different circular polarizations. The utility of this scheme rests on the stable polarization characteristics of the Nd:YAG laser. Also inherent in this scheme is the assumption that free space will not alter the initial polarization.

The beam splitter is made of quarter-wave dielectric stacks, similar in design to the primary mirror of the vehicle. Figure 45 shows a schematic depicting the effects of the polarizing beam splitter.

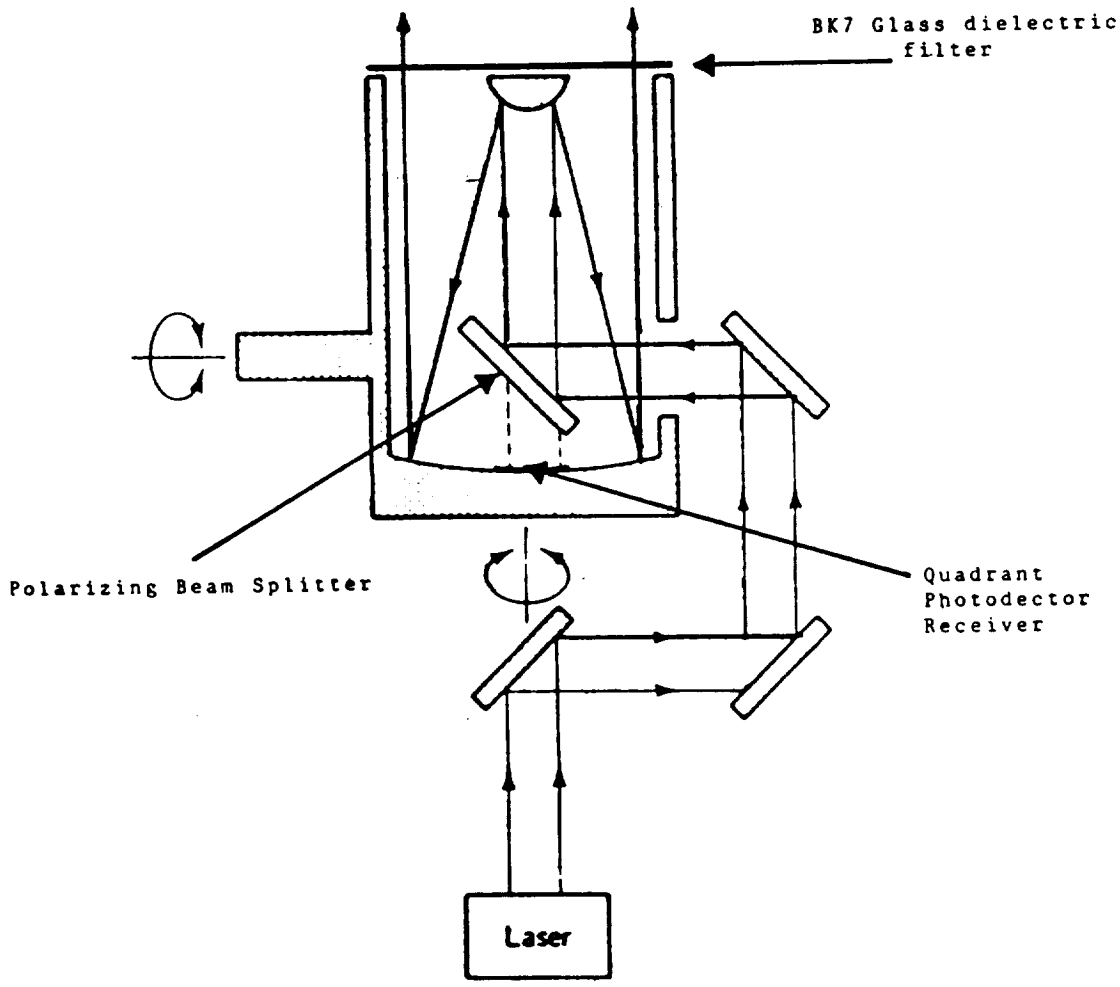

Figure 44. Optical Trasceiver Labelled Schematic

Receiver:(D). The receiver sits at the bottom of the telescope, beneath the polarizing beam splitter. Incident beams reflect off the small central obstruction, onto the beam splitter. The beam splitter is configured to allow a preset polarization through.

For laser acquisition, the dominant requirement is signal detectability. For laser tracking, high signal-to-noise ratios are needed for the angle output. A quadrant photodetector yields a high SNR and will be used in the vehicle's optical receiver. The quadrant protector is a direct detection detector. This type of detector is most efficient when large intrinsic gain is available and when the input wavelength is below 1 micrometer. Above one micrometer, thermal noise can dominate and systems such as heterodyne or homodyne detectors must be used.

There are three types of direct detector elements available: photo-voltaic, biased-photodiode, and avalanche photodiode (APD). The first has limited usefulness, but the last two are fast and accurate. The lower power requirements of the APDs and their smaller mass make it the device selected for beam detection.

There are four APDs--one in each quadrant. The basic detection operation involves the computation of the intensity of the beam in the quadrants, normalized with respect to the incident beam. By computing the change in intensity between the quadrants, it is possible to calculate the attitude change of the laser beam. This information is translated into the vehicle's attitude motions by the control computer.

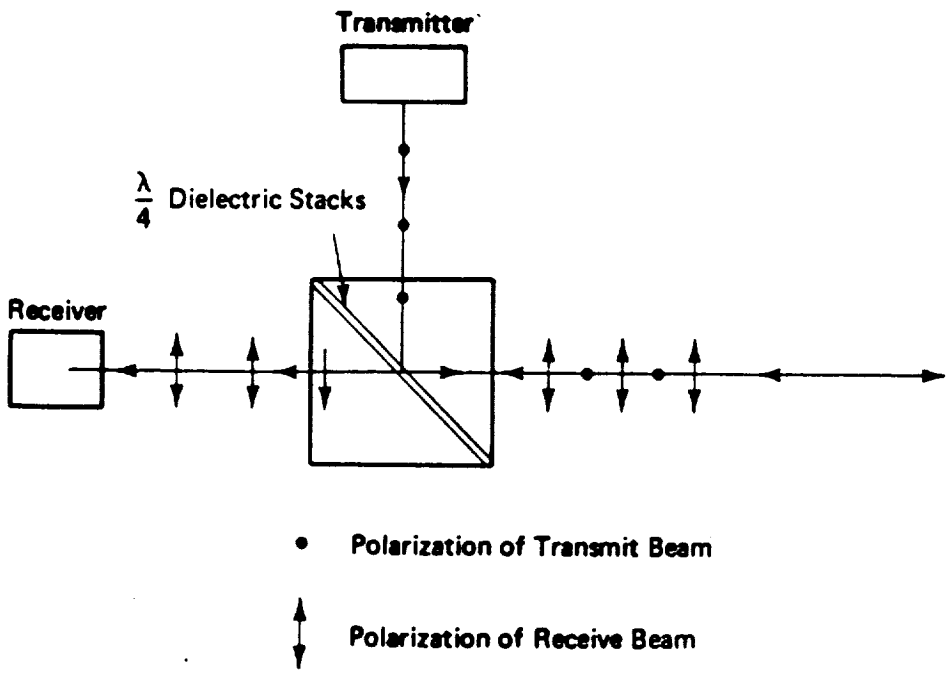

Figure 45. Polarizing Beam Splitter

Transmitter Path: The transmitter path is simply the path followed by the laser beam from the vehicle to the telescope. From the schematic of the telescope, it is obvious that the laser does not have to be contained on the gimbal platform, rather, it can be off-platform. However, for simplicity, the laser will be located on the platform.

Mirror Alignment System

A network of mirror alignment system is distributed among the primary, secondary and fifth mirror. Photodetectors are also placed about the circumference of the laser rocket. The purpose of this system is two-fold. First, it allows fine tuning of the optical path and second, it provides a redundant control (in addition to the laser tracking beam). The feedback system is described below for each mirror and the laser rocket.

Primary Mirror: The primary mirror has a system of APDs built into the dielectric surface. They are located on three rings centered about the center of the primary mirror. The three rings have radii of 6.0, 6.33 and 6.66 meters. The APDs are angularly spaced every 20°. The APDs contain dielectric filter windows tuned to the incident wavelength of the power beam. The inner most circle of rings corresponds to the actual beam spot size. The others are equidistant from the edge of the primary mirror and the edge of the spot (Figure 46).

Upon movement of the laser power beam, the APDs will trigger and the control computer will adjust the position of the main mirror via attitude mechanisms.

Secondary Mirror: The secondary mirror has four photodetectors situated around the mirror's periphery. These photodetectors detect focusing problems from the primary mirror. Due to mirror surface stresses, thermal gradients, and other surface altering disturbances, the surface of the primary mirror will not focus squarely on the secondary mirror. If the beam does not converge evenly on the secondary mirror, part of the main beam will be reflected back onto the primary mirror causing further thermal damage and poor laser rocket performance. When this mis-focusing occurs, the APDs will trigger, and slight focusing characteristics can be changed by moving four small, pneumatic actuators in contact with the backside of the mirror (Figure 46).

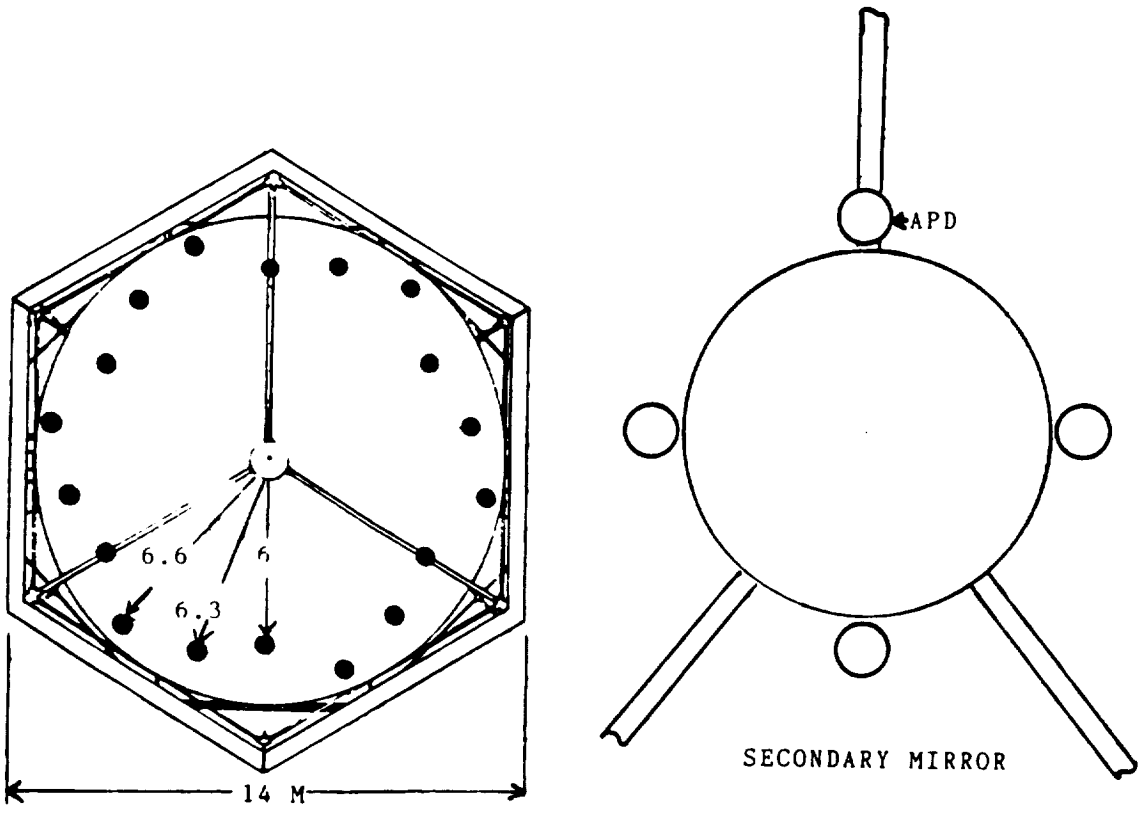

Figure 46. Mirror Alignment System for Primary and Secondary Mirrors

Fifth Mirror: The third and fourth mirrors do not need any mirror alignment management system because once the beam strikes the third mirror properly (with the help of the secondary mirror alignment system), the path from the third to the fourth is rigidly set. However, the fifth mirror must insure that the beam strikes the laser rocket engine properly. To insure this condition, APDs have been placed on both the fifth mirror and the laser rocket engine.

Four APDs have been placed on the fifth mirror on both the top and bottom edges and on the sides. Also, a small rotational mechanical transducer has been attached to the fifth mirror's pivot axis to allow for small angular rotations. This arrangement can be seen in Figure 47. When the APDs trigger the fifth mirror will rotate about the gimbal axis.

Laser Rocket: The laser rocket also has four APDs situated about it's outer edge. This arrangement is shown in Figure 48. If the APDs on the top or bottom of the rocket trigger, the laser rocket basket can move to correct the alignment. If the APDs to the right or left trigger, then modifications will have to made to the fifth and secondary mirrors because the laser rocket has no translational capability to move to the left or the right.

The block diagram shown in Figure 49 summarizes the basic interactions between different subsystems that comprise the ATP system.

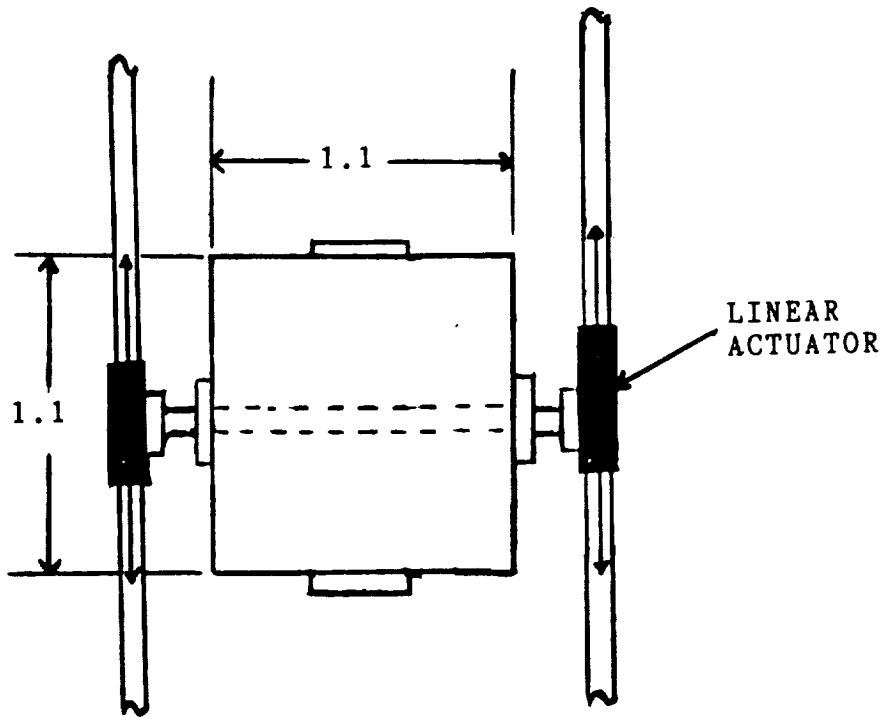

Figure 47. Mirror Alignment System for Fifth Mirror

Typical ATP Scenario

A typical ATP scenario consists of four distinct phases.

ATP Phase I--Aiming of the LOCOST vehicle

The vehicle uses its omnidirectional antenna to initiate the ATP sequence. The LPS responds using its RF antenna. The vehicle relays its attitude and spatial orientations to the LPS. The LPS sends out its position information. The vehicle aligns itself so that it is now capable of using its directional antenna for telemetry tracking and control. The vehicle orients its lasercom telescope in the direction of the LPS.

ATP Phase III--Acquisition of Pilot Beam

The LPS emits a defocused laser beam into the error volume. The optical receiver detects the defocused beam. The vehicle emits a return laser beam. The LPS detects the return laser beam. The LPS narrows down the error volume until a narrowly focused pilot beam is achieved.

ATP Phase IV--Tracking of the Power Beam

The vehicle continues to track the laser pilot beam. When the beam becomes misaligned due to vehicle movement, the attitude controllers onboard the vehicle activate. The directional antennas are used to relay telemetry and vehicle-health information.

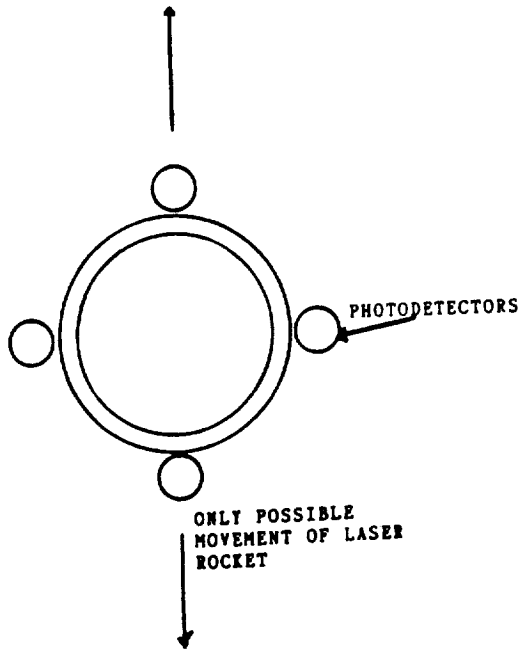

Figure 48. Laser Rocket Mirror Alignment System

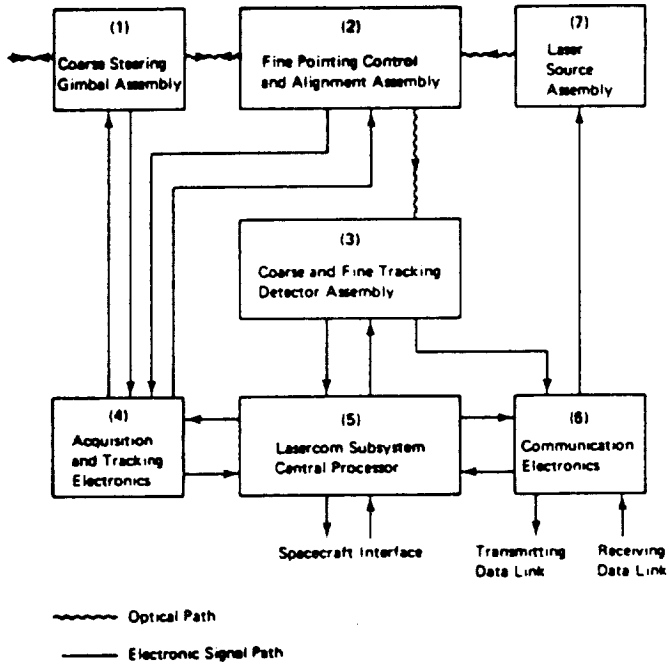

Figure 49. Block Diagram of Sub-System Interactions of the ATP System

Communications

Introduction

The communications system of any unmanned space vehicle is essentially the life line of the vehicle. Although the data transfer requirements are lower than that of a manned vehicle, the communications link must provide sufficient communications for control of the entire vehicle. This includes telemetry, vehicle control, and initial position tracking.

The communications system data load of the LOCOST vehicle is slightly reduced by the tracking done through the APT system. However, the initial link between the vehicle and laser station must be made through the communications system in order to provide the APT system with starting position coordinates and alignment parameters.

Communication system requirements

The communication system on a spacecraft such as the LOCOST vehicle must have high reliability low power consumption, high speed data transfer, and longevity in use. The system must transmit and receive signals efficiently if it is to have a low power consumption. This plus the great distances through which communication will be done necessitates the use of one or more highly directional antennas. Since the communications system must also provide the initial link from a possibly unknown position, an omni-directional antenna is also required. Redundancy in the communication system is important due to the dangers involved in a loss of communication. For this reason, two transmitters and two directional antennas will be used. The communication system must also include RF subsystems for communications between the craft and Earth and/or the space station (using S-band).

System Protocol and Coding

Although most of the sub-systems of the LOCOST vehicle will be controlled by the on-board computer, the communication system must provide constant status for the subsystems. In the event of a computer failure, the communication system must also be capable of handling the data needed to control all of the vehicle's sub-systems.

Normally the optical system will be controlled through the APT system. Thus, all non-optical systems will deliver system status and other information through the communications system. Some of these systems include: position/stability mechanisms (RCS/CMG), electrical power control, propulsion control, fuel storage monitors, structural monitors, and the docking system. The protocol of the communication system must handle the routine transfer of data from these systems and be able to handle emergency situations. One way of handling so many systems is to use a different radio frequency band for each sub-system. Because of the increasing number of communication links in space, and the possible crowding of radio frequencies in the future, the communication system of the LOCOST system was designed to use the least number of frequency bands. Only a single band is needed to relay the data for all the vehicle's subsystems if multiplexing is used. To facilitate the multiplexing of normal sub-system information along with emergency status information and commands, a coding system was developed which has been named Priority Interrupt Protocol (PIP). This system uses a digital signal carried by an analog wave. A sample of this protocol is shown in Figure 50.

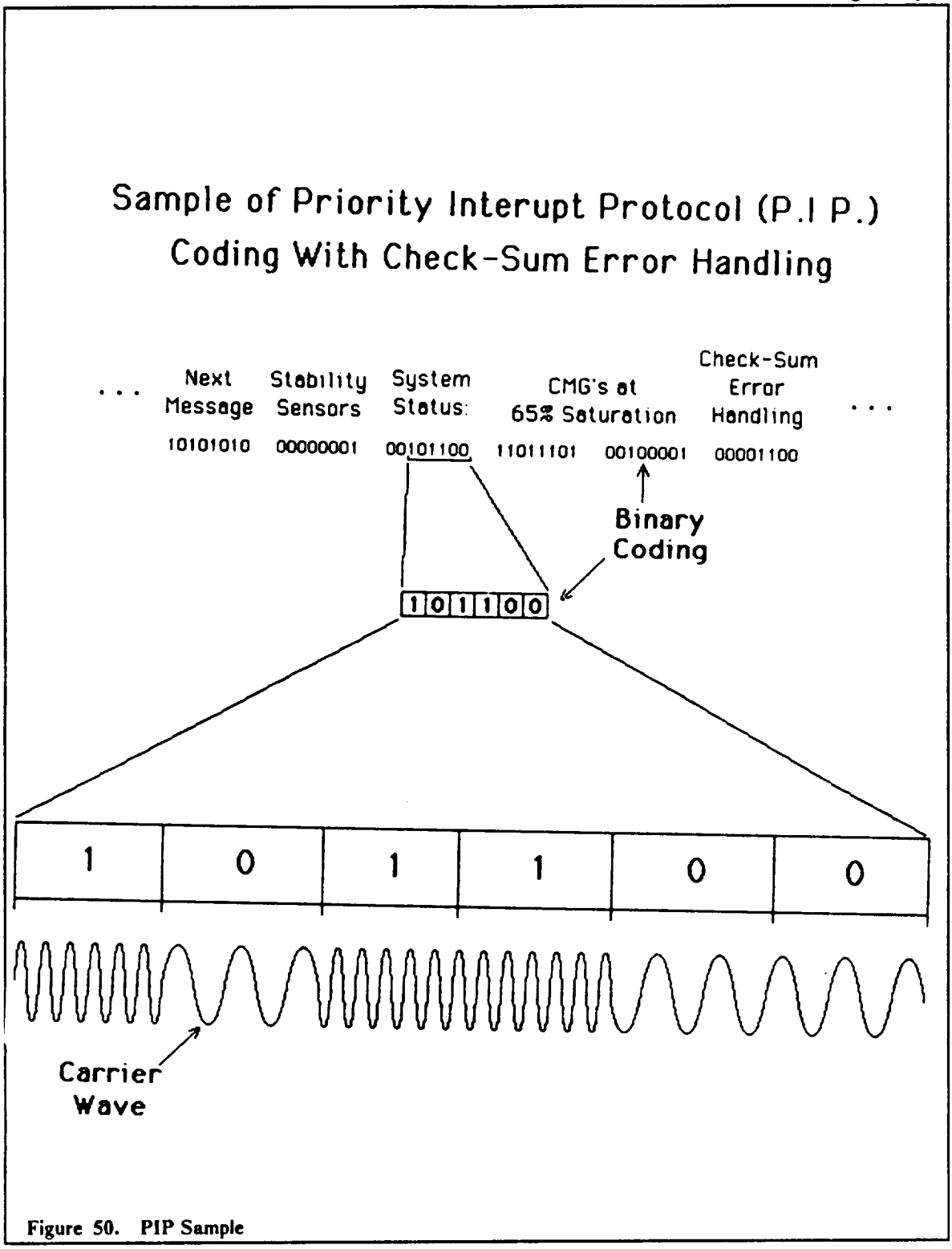

Figure 50. PIP Sample

The multiplexing done by the P.I.P. system is accomplished by sending data for each subsystem in an ordered sequence. The communications processor will send each set of data in the following format: new message flag, subsystem identification, message type, data, and a check sum error handling number. Since the entire message is coded in a binary digital code, the error handling is done by summing up the total number of binary 1's in the message and sending this number as the last part of the message. This is called check sum error handling. In the event of an emergency, a universal interrupt code can be sent by any sub-system to the communications processor. This interrupt code will override the normal sequence of messages and the critical sub-system wil be

given immediate communication priority. The actual modulation of the radio wave is done by Frequency Shift Keying. This simple technique is basically a binary frequency modulation, as shown in Figure 50. Each sub-system is linked directly to the communications processor, which sequencially sends each system's status to a coding modulator. The encoded signal is then sent to a transmitter, antenna switcher and then to one of the antennas. Signals sent back to the LOCOST vehicle will be collected by an antenna, amplified through a receiver, interpreted by the coding demodulator and sent to the communication processor.

Antennas

The size of the antennas on the LOCOST vehicle is primarily governed by the transmitter power and wavelength used. The required transmitter power and antenna diameter are estimated to be 150 W and 1.35 m, respectively (λ = 0.06 m). The placement of the antennas and communications system can be seen in Figure 50.

Since the vehicle will use the laser station for its communication link, the pointing of the directional antennas will be done throught the APT system. This can be done because the primary laser mirror and the directional antennas will be pointing in the exact same direction. This eliminates the need of an additional tracking and pointing system. Spacecraft status and performance will be monitored by various sensors. Data collected from these sensors will be transmitted to the ground control station by the communication subsystem using 2.3 GHz downlink frequency. The uplink frequency of 2.4 GHz will be used for command functions.

Summary

The communications system has a total mass of 200 Kg. The system uses two parabolic directional antennas, each with a diameter of 1.345 m. One omni-directional antenna with a length of 12 m is also used. The transmitter used has a power of 150 Watts, and operates at a frequency of 5 GHz with a wavelength of .06 m. The total power consumption of the communications system is 200 Watts.

Electrical Power Sytems

Introduction and System Comparison

The power systems considered for the vehicle were radioisotopic generators, solar collectors, and secondary batteries. reactors, radioisotopic generators, solar collectors, and secondary batteries. The necessary characteristics for the power system are light weight, dependability, high reliability and power density, long life, and maintainability. The average power requirements for the vehicle are summarized in Table 47.

For the length of mission specified, fuel cells and secondary batteries are the best alternatives. Longer missions would make the volume and mass penalties of these two systems too great. Solar cells must be connected in panels or arrays to provide a large enough power ratio to make them feasuble for use. For the power-to-mass ratio necessary for our vehicle, this array would be much too large. This system would also depend too much on solar energy since our vehicle is not always illuminated. Secondary batteries have high energy densities but are not a viable alternative because the capacity of a secondary battery is governed by the size and weight of electrodes which store chemical energy, which accounts for much of the size and weight of the battery. Radioisotopic generators do not have high enough power densities to be usefull because of the low efficiency of direct conversion processes which this system utilizes.

The fuel cell is a form of storage battery in which the chemical energy is stored as a fuel in a reactant tank outside the cell and is fed to, or removed from, the electrodes when required. The electrodes are not changed in any way when the cell is operated. The capacity of a fuel cell is governed only by the size of the fuel tanks and the battery size is related only to the rate of conversion of power output. Fuel cells were chosen because they are mass competitive with other systems, utilize readily available technology, are highly reliable, offer redundancy, have a high conversion efficiency over a wide output range and have zero fuel consumption during dormant periods. Four fuel cells will be used to power the necessary systems on the vehicle. One cell will be placed below the primary mirror on the support truss. Two will be in the truss section between the hydrogen and oxygen tank sections. The last will be at the rear of the vehicle on the lower part of the truss between the two chemical engines.

Components

The fuel cells that have been most extensively developed use hydrogen as their fuel and oxygen as an oxidizer. The main components of a fuel cell are the fuel supply system, regulation system (preheater and regulator), reaction cells, and the water bleed off system, as seen in Figure 51.

Table 47. Vehicle Power Requirements

System	Power (kW)
Communications	.2
Data Management	.5
ATP: Laser Peak Power	.2
Induction Motors (2)	.012
Propulsion: Start-up Motor	.1
H_2 Turbopump	.22
O_2 Turbopump	9.4
Gimbal Actuator	.01
Electric Fuel Pumps (2)	2.08
RCS: CMGs Quiescient Power	.5
Optics: First Mirror's Motors (2)	.15
Fourth Mirror Tourque Motor	.2
Fifth Mirror Linear Actuator Motor	.3
Heat Pipe System Aux. Heating Units	1.4
Structures: Rocket Basket Linear Actuator Motor	.003
Radiator Pumps	.15
Distribution Loss	.05
Gyroscopes	1.2
Total	16.44

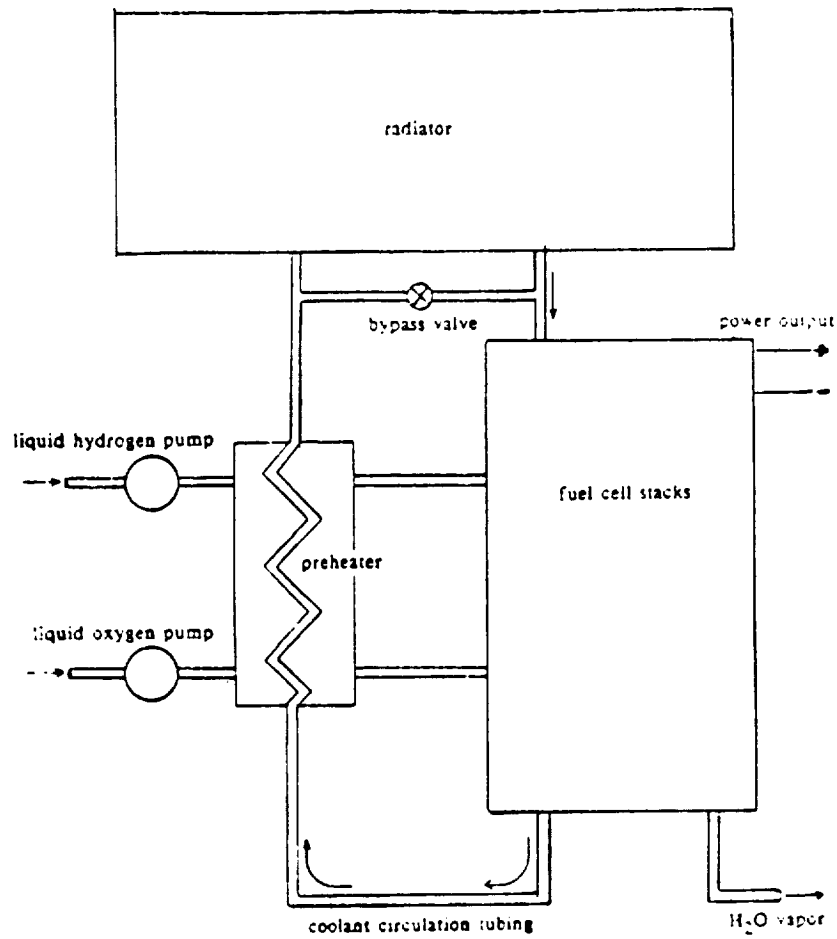

Figure 51. Basic Components of a Fuel Cell Power Generator

A "stack" of a number of cells connected in series is used in conjunction with other stacks in parallel to give the required power. The maximum current output of a stack depends on the individual cell membrane area and max. allowable current density of the membrane.

The reaction cell consists of an anode and cathode region, each filled with electrolyte, at which the ion exchange occurs. Three plates are needed. The hydrogen metering, oxygen metering, and sealed separation plates. The electrode support or current carrying plate is made of corrosion protected magnesium. This positions the electrodes, serves as a manifold to distribute the gas to the electrode area, and conducts current externally.

Preheater System and Cooling

A percentage of the waste heat will be employed in a preheater system which raises the temperature of the cryogenic fuel to the operating temperature of around 125 degrees celcius. A radiator will be used to cool the fuel cell. The mass of the radiator is approximately 50 kg.

Water Removal System

The components of the water removal system are water transport membranes saturated with 45% potassium hydroxide, two pourous support plaques, and a plastic water removal plate similar to the support plate. Two end plates and tie bolts complete a single cell.

Fuel Cell Housing

The fuel cell is housed in a double walled aluminum shell to provide protection from meteroid strikes and radiation. The walls are .15 cm thick and there is a separation distance of 10 cm between the inner and outer walls. The shell provides 99% particle protection and rejects or dissipates 97% of incident radiation. The inner shell has a 1 m diameter, is 1 m tall and weighs 118 Kg. The outer shell has a diameter of 1.2 m, is 1.2 m tall, and weighs 149.3 Kg. The mounting weighs 10 Kg. This system will provide a very long lasting, efficient supply of power for the LOCOST vehicle.

Appendix A. Mirror Cooling Calculations

The Heat Pipe

Figure of merit calculation for heat pipe fluids

Entrainment Limit:

$$\text{ent} = \pi r_v^2 L \sqrt{\frac{2ip\rho_v\sigma_l \cos\theta}{\lambda}}$$

Where

λ is the characteristic dimension of liquid/vapor interface for fine mesh (.036 m)
σ_l is 0.086 N/m

Hence, Q_{ent} for Na is 423,086 kW and for Li it is 455,243 kW. These are both well above the required heat transport capability.

Axial Heat Transport:

$$M = \rho_l \sigma_l L$$

Where

ρ_l is 430 kg/m^3
$sigmal_l$ is .275 N/m
L is 20,000 kJ/kg

At a temperature of 1200 K, M_{Li} is 10,282,608, while that for sodium is (M_{Na}) is 1,371,994.

Boiling:

Boiling which may result in vapor blocking in arterial heat pipes--bubbles in artery is a problem. Hence, a high superheat (Δ T) is needed to reduce change of nucleation.

$$M = \Delta T_s = \frac{\sigma_l}{L_{\rho v}}$$

At 1200 K, Na yields 0.0001 while Li produces 0.0049.

Radius of heat pipe

$$Q_{max} = .4\pi \times .73L \times \sqrt{p_E \rho_E}\, r_2^2$$
$$= 10 \text{ MW allowable heat input rate}$$

Where

p_E is 9.59 Bar = 9.59$\times$ 10^5 kg/m^2
L is 3,577,000 J/kg

Hence, r_c is 0.045 m $\simeq$ 5 cm.

Thermal gradients:

Sample calculations

10MW *times* how long beam on mirror (3 hr.) $= Q$ the total energy absorbed

$$\frac{Q}{m\,(\text{mass of mirror})} = q \text{ sepecific energy absorbed}$$

$$\frac{q}{\text{specific heat}} = T \text{ temperature difference at front of mirror from original state}$$

Using the heat conduction equation,

$$x = k \times A \times \left(\frac{T}{q}\right)$$

Assume linear distribution of temperature through mirror. This gives thermal gradient through mirror versus time.

$$E = \sigma \times a \times T^4$$

Radiator Size Calculations:

All cooling requirements (156.2 kW + 159.8 kW + 161.5 kW) = $\dot{q}$. Hence, $\dot{q}$ is 477.5 kW. Then

$$477500 = .85 \times 5.67 \times 10^{-8} \times A \times T^4$$
$$= 76.5m^2$$

Support Calculations:

Maximum allowable deflection of 2nd mirror. Assume

$$\Delta A < .1\ \% \times A$$

Hence, ΔA is 0.00095033 m^2

From

$$\Delta r(\text{avg})^2 + 2r\Delta r(\text{avg}) - \frac{2\Delta A}{\pi} = 0$$

Hence, Δr is 0.0012099 m.

Then, from

$$\Delta r = d\theta$$

θ is 0.00014068 radians. The deflection can be expressed as $\delta = \theta x$ = 0.00014068. For a 9.9 kW loss of power, δ = 0.000985 meters.

Appendix B. NOTS Input and Calculations

The following equations and numbers are required input for the NOTS program.

The entering temperatures are:

$T_{\text{entering } O_2} = 99.85°\text{K}$

$T_{\text{entering } H_2} = 267.07°\text{K}$

The entering enthalpy:

$$\text{H} = \text{H}_f + C_p\Delta T + H_{\text{fg}}$$
$$= O + .4(90 - 298) + (-50.9) = -4300\,\frac{\text{cal}}{\text{kgmole}}$$

The specific thrust:

$$\text{I}_{\text{sp}} = \frac{\text{T}}{\dot{\text{m}}_{\text{a}}}$$
$$= 5835.59\,\frac{\text{m}}{\text{s}}$$

The maxmimum thrust in g's where 1g = 9.8 m/s:

$g_{\text{max}} = \text{T}_{\text{Total/Empty mass}} = .51gs$

The thrust coefficient:

$$\text{C}_\text{F} = \left(\frac{2k^2}{k-1}\left(\frac{2}{k+1}\right)^{\frac{k+1}{k-1}}\left[1 - \left(\frac{P_e}{P_c}\right)^{\frac{k-1}{k}}\right]\right)^{\frac{1}{2}} + \frac{P_e}{P_c}\ \frac{A_e}{A_t} = 1.955$$

Geometry calculations:

$$A\text{T} = \frac{T}{\delta_F C_F P_c}$$

δ_F = Thrust Efficiency = .99

$$A_T = \frac{2500}{.99 \times 1.955 \times 10376975} = 1.24 \times 10^{-3}\,m^2$$

$$D_T = \sqrt{\frac{4A_T}{\pi}} = .0398m$$

$A_e = \varepsilon A_T$ where ε = Area Ratio

Chamber Calculations:

$$A_c = \frac{TgRT_c}{v_{\text{injector}} P_c V_c \overline{MW}} = \frac{25000 \times 9.8 \times 3602 \times 8314}{4840 \times 13.412 \times 10376975 \times 91.44}$$
$$= .012m^2$$

L^*(typical) = 1.016m

Volume chamber = $L^{*}A_t$
Nozzle half angle = 15°

$L_c = D_c$(Length Ratio) = $.3731m$

Wall thickness:
For a cylinder under radial pressure:

$\Delta p\, D = 2t_w S$

$$S = \text{working stress} = \frac{\text{yield stress}}{\text{factor of safety}} = \frac{25000}{2} = 125000\text{psi}.$$ Hence, $t_w = 3mm$.

Pump parameters:

Turbopumps

$$\text{Power} = \frac{\dot{m}H \times \text{SG}}{k}$$

For turbopumps, k = 1 in metric units.

$\dot{m}_{fuel} = .76$ kg/s
$\Delta P_f = 9.9$ MPa
H = 1.9 m = pumphead
P = .11 kW
$\dot{m}_{OX} = 4.55$ kg/s
$\Delta P_{OX} = 9.6$ MPa
H = .9m
SG = 1.139
P = 4.7 kW

Electric pumps

$P = \dot{m}\, H\, \text{SG}$

$\Delta P_{O_2} = 1.9MPa$
$\Delta P_{H_2} = 7.16MPa$
$P_{O_2} = 4.55 \times .2 \times 1.139 = 1.0365kW$
$P_{H_2} = .759 \times .72 \times .0708 = 38.69W$

Appendix C. Thermal Balance Calculations

The thermal balance for the structure is calculated using an iterative process with the following equations:

$q_A + q_I + q_R$

$q_A = A_S + q_a + q_e$

The heat due to the sun:

$$q_S = S\alpha_S A_S \frac{(P - t_S)}{\rho}$$

Where

S is the solar constant = 1350 w/m² (watts per square meter)
α_s is the absorptance of the exterior surface for solar energy = 0.25
A_S is the cross sectional area exposed to sunlight
P is the orbital period
t_S is the time in Earth shadow

The heat due to the albedo:

$$q_a = S_a \alpha_a A_e \frac{\cos \alpha}{\pi R^2} P$$

Where

S_a is the albedo = 0.345 × S
α_a is the absorptance of the exterior surface for albedo radiation
A_e is the cross-sectional area exposed to radiation from earth
cos α where α is 22°, the angle of the satellite's orbital plane
R is the arbital radius in earth radii

The heat to the earth's radiation:

$$q_e = \frac{PW_E \alpha_E A_E}{R^2}$$

Where

W_E is the average flux of earth generated radiation = 240 W/m²
α_e is the absorptance of exterior for Earth radiation = 0.20

q_I is the heat radiated from the back of the mirror. The internal heat:

$q_I = P \times M \times \alpha_m \times A_m$

Where

M is the heat flux from back of mirror = 2390 W/m²
A_m is the cross-sectional area exposed to radiant energy from mirror
α_m is absorptance of the exterior surface for mirror radiation = 0.30

The dissipated heat:

$$q_R = \sigma \times \varepsilon \times AR \times T^4$$

Where

σ is the Stefan-Boltzman constant
ε is the material emmittance at temperature T = 0.20
AR is the "effective" area for heat radiation
T is the absolute temperature in degrees Kelvin

The area for heat absorptance for a cylinder (A_S,A_s) is

$$A = D \times H$$

Where

D is the diameter of cross-section of individual strut = 0.00025 m^2
H is the sum of all strut lengths exposed to a particular radiation

The area for heat radiation for a cylinder (A_R)

$$A = (\pi \times D \times H) + \frac{(\pi \times D^2)}{2}$$

Where

H is the sum of all the lengths of all struts with incident radiation.

Appendix D. Propellant Tank Calculations

Mass of LH_2 required = 52769 kg
Mass of LO_2 required = 40231 kg
Density of LH_2 = 70.8 kg/m²
Density of LO_2 = 1139 kg/m³
Total volume required LH_2 = 749 m³
Total volume required LO_2 = 35.3 m³

Spherical LO_2 tanks

$V = 4/3\pi R^3$

$S = 4\pi R^2$

Per tank:

V = 17.66 m^3
R = 1.62 m
D = 3.23 m
S = 32.8 m

For Al 2090:

E = 7.584×10^4 MPa
$\sigma_{ult} = 2.237 \times 10^4$ MPa
e = 3547 kg/m^3

From

$$\frac{\sigma_{max}}{F.S.} = \frac{p_r}{2t}$$

Where

σ_{max} = max stress
p = tank pressure
r = radius
t = thickness

The thickness is t = .067 mm.

From, mass of tank = surface area (t) e, the mass of the liquid oxygen tanks are 5.6 kg.

Cylindrical LH_2 tanks.

R = 3.14 m
D = 6.28 m
S = 3.25 πD^2 = 402.67 m^2

Use the same calculation for the liquid oxygen tanks to obtain the mass of the hydrogen tanks.

Insulation Dimensions and Mass

The same calculations apply to both the liquid hydrogen and the liquid oxygen tanks. The liquid hydrogen calculations are shown below.

Given the condition of 1 percent total boiloff from 26384.8 kg of fuel, the heat flux $\dot{q}$ for this boiloff to take place is calculated using

$$M_{vf} = \frac{\dot{q}\theta}{h_{fg}}$$

Where

M_{vf} is the mass of fuel vented
θ is the the length of mission $\simeq$ 2 weeks
h_{fg} is the heat of vaporization of LH_2 (499 kJ/kg)
$\dot{q}$ is the total heat transfer

Then $\dot{q}$ = 64.857 W.

The heat flux due to solar radiation on the tank:

$$\dot{q} = Aq''\varepsilon$$

Where

$\dot{q}$ is the heat flux
A is the area exposed to solar radiation (201.34 m²)
q'' is the solar radiation constant (1400 W/m²)
ε is the emissivity of tank (.06 since paint is 94% reflective)

Hence, $\dot{q}$ is 16.91 kW.

Use the Stefan-Boltzman law to find the temperature on the surface of the tank:

$$\dot{q} = \sigma AT^4$$

Where

$\dot{q}$ is the total heat flux (16973.9 W)
σ is the Stefan-Boltzan constant (5.67×10^{-8} W/m²K⁴)
A is the area exposed to solar radiation

Hence, T = 196.4° Kelvin.

The MLI thickness can then bet determined from the equation:

$$\dot{q} = \frac{kA(T_1 - T_2)}{t}$$

Where

k is the thermal conductivity of insulation (.03 W/mK)
T_1 is the temperature of the tank surface
T_2 is the interface temperature of the MLI/foam (144 K).

Hence, t_{MLI} is .0186 m.

From

$$\frac{t_{foam}}{t_{MLI}} = .1$$

t_{foam} is .186 cm.

The densities of the MLI and foam are ρ_{MLI} = 35.08 kg/m³ and ρ_{foam} = 30 kg/m³.

Hence, the total mass for the liquid hydrogen per tank is

$$m = S(t_{foam}\rho_{foam} + t_{MLI}\rho_{MLI})$$
$$= 570.98kg$$

The mass of the support structures can be obtained from the relation

$$m = \pi(R_2^2 - R_2^2) \times 1 \times \rho$$

Where $\rho_{grap/epoxy}$ = 1685 kg/m^3, and $\rho_{6061-T6}$ = 2550 kg/m^3.

References

Aero Assisted Flight Experiment, NASA George C. Marshall Space Flight Center, May 27, 1986.

"Aerospace Vehicle Design, Vol. 2 Spacecraft Design," Johnson Publishing Co., Boulder Colorado, 1964.

Avollone, E.A., Baumeister, T.M., *Standard Handbook for Mechanical Engineers, 9th ed.*, McGraw-Hill, 1987.

Bate, R.R., Mueller, D.D., White, J.E., *Fundamentals of Astrodynamics*, Dover Publications, Inc., New York, 1971.

Boxenhorn, B., Greiff, P., "A Vibratory Micromechanical Gyroscope", *AIAA Gudiance, Navigation and Control Conference Part 2*, August 15-17, 1988.

Braunstein, Morris, "Infrared Coatings for High Energy Laser Reflectors and Windows," *SPIE Vol. 140, 1978.*

Dennison, E.W., Stanton, R.H., Shimada, K., "The Development of a Charge-Coupled Device Tracker for Spacecraft", AAS 87-007, *Guidance and Control 1987: Advances in the Astronautical Sciences Volume 63*, Culp, R.D. (ed), 1987.

DeYoung, R.J. (ed), *Second Beamed Space-Power Workshop*, NASA.

Dunn, P.D. and Reay, D.A., "Heat Pipes 3rd ed." *Pergamon Press, New York, 1982*

Dursch, H.W., Hendricks, C.L., *Protective Coatings for Composite Tubes in Space Applications*, NASA N87-18669, 1987.

Dutta, P.K., Kalafut, J.F., Lord, H.W., "Response of Advanced Composite Space Materials to Thermal Cycling", *Engineering, Construction, and Operations in Space*, 1988.

Franz, J. and Laube, H., "Design and Manufacturing Aspects of Tubular Carbon Fiber Composite/Titanium Bonded Joints," *Composite Structures, 1986.*

Frisbee, R. H., Horvath, J. C., Sercel, J. C., "Space-Based Laser Propulsion for Orbital Transfer," Jet Propulsion Laboratory, December 1984.

Goble, R.G., "Temperature Uncertainties Associated with Spacecraft Thermal Analyses", *Fundamental of Spacecraft Thermal Design*, The MIT Press, 1972.

Graham, O.L., Russel, J.K., and Epperly, W.L., *Range and Range Rate System*, NASA N87-22708, 1987.

Heard W.L., Busth, H.G., and Watson, J.J., "Space Truss Construction Studies", *Engineering, Construction, and Operations in Space*, 1988.

Hill and Peterson, *Mechanics and Thermodynamics of Propulsion*, Addison Wesley Publishing Company, Reading, Massachusetts, 3rd printing, Nov 1970, c. 1965.

Johnson, Stewart W. and Wetzel, John P., "Engineering, Construction, and Operations in Space," *American Society of Civil Engineers, Albaquerque, New Mexico, 1988.*

Jones, Hawkins, Wiley, "Engineering Thermodynamics 2nd Edition," P.E. John Wiley & Sons, Inc., c. 1986.

Katzman, M., (ed), *Laser Satellite Communications*, Prentice-Hall, 1987.

Keefer, Dennis R., Crowder, Herbert, Elkins, Rush, Eskridge, Richard, "Laser Heated Rocket Analytical and Experimental Support Final Report,", *Advanced Propulsion Systems* Lockheed Missles and Spacecraft Co., July 1981.

Keckler, C.R. (ed), *Integrated Flywheel Technology 1983: NASA Conference Publication 2290,* 1983.

Korsmeyer, David J., *Trajectory Determination & Characterization of Cislunar Low-Thrust Spacecraft*, Large Scale Programs Institute paper no. LBS-88-080.

Kubin, Robert F., Presley, Leroy L., *Thermodynamic Properties and Mollier Chart for Hydrogen From 300 K to 20,000 K,* Ames Research Center, 1964.

Lademann, E.E., "Gyro Technology", AAS 87-020, *Guidance and Control 1987: Advances in the Astronautical Sciences Volume 63*, Culp, R.D. (ed), 1987.

Laser Rocket System Analysis, Lockheed Missiles Space Company Inc., Sept 1978.

Laskin, R., Estus, J., Lin, Y., "NASA Office of Space Science and Applications Study on Space Station Attached Payload Pointing", *AIAA Gudiance, Navigation and Control Conference Part 1*, August 15-17, 1988.

"Lewis Structures Technology-1988-Vol. 2," *Structural Mechanics NASA-1988.*

Lubin, George (ed)., *Handbook of Composites*, Van Nostrand Reinhold Co., Inc., 1982.

Lunc, Michal (ed), *Guidance and Control*, Paris, France, 1965.

Malla, R.B., Nash, W.A., and Lardner, T.J., "Thermal Effects on Large Space Structures with Fixed Attitude", *Engineering, Construction, and Operations in Space*, 1988.

Marshall, I.M. (ed), *Composite Structures 5*, Elsevier Applied Science, London, 1989.

McCay, T.D., Toenes, J&adi.rgen, *Numerical Modeling of Laser Thermal Propulsions Flows*, NASA Marshall Space Flight Center.

Meffe, M., Stocking, G., "Momentum Envelope Topology of Single-Gimbal CMG Arrays for Space Vehicle Control", *Guidance and Control 1987: Advances in the Astronautical Sciences Volume 63*, Culp, R.D. (ed), 1987.

Meyer-Arendt, Jurgen, R., *Introduction to Classical and Modern Optics,* Prentice-Hall, New Jersey, 1984.

NASA Conference on New Technology, Lewis Research Center, Cleveland Ohio, June 4-5, 1964.

N.B.S., U.S. Department of Commerce, *JANAF Thermochemical Tables 3rd. Edition,* NSRDS-NBs 37, U.S. Government Printing Office, June 1978.

Naval Ordnance Test Station, *NOTS,* China Lake, CA.

Osgood, Carl. "Spacecraft Structures," *Technical Advisory Staff.* Prentice Hall, Inc., Englewood Cliffs, N.J. 1966.

OTV Concept Definition & System Analysis Study Detailed Presentation-Volume II, General Dynamics, Space Systems Division, July 2, 1986.

OTV Concept Definition & System Analysis Study Contract Extension Final Review, NASA-MFSC, Martin Marietta, July 1, 1986.

OTV Concept Definition System Analysis Study, NAS8-36107, presented to NASA by Boeing Aerospace Company, July 1, 986.

OTV Concept Definition Study, Report No. GDC-ASP-80-012, General Dynamics Convair Division, Contract NAS8-35333, Feburary 1981.

OTV Technology Items, Rockwell International, Rocketdyne Division, October 1984.

Pratt & Whitney Aircraft Government Products Division, "Orbit Transfer Rocket Engine Techonolgy Program--Final Report," *NASA Contract NC.3-23171*

Project SLICK, NASA/USRA Advanced Design Program, Department of Aerospace and Ocean Engineering, VPI & SU, Blacksburg, VA., 1987.

Quasius, G, McCanless, F., *Star Trackers and Systems Design*, Macmillian and Co., London, 1966.

Ring, E., *Rocket Propellant and Pressurization Systems*, Prentice Hall.

Saxton, D., *OTV:Concept Definition & Systems Analysis Study Final Report-Phase I Volume V*, Boeing Aerospace Company.

Schulz, G., Lange, Th., "Attitude Control of Geostationary Satellites with Double Gimballed Momentum Wheels", *AGARDograph No.260: Spacecraft Pointing and Position Control*, van den Broek (ed), 1981.

Sevaston, G.E., Lchier, J.A., Iskenderian, T.C. et al., "A Precision Pointing System for Space Telescope Class Optical Trackers", *AIAA Gudiance, Navigation and Control Conference Part 1*, August 15-17, 1988.

Shaw, R.H., Thompson, R.A., "Hydrogen-Oxygen Fuel Cell System for Space Vehicles", *Power System For Space Flight: Progress in Astronautics and Aeronautics-Volume 11*, 1963.

Shuttle Propulsion Systems: ASME, United Engine Center, 345 East 47th St., New York, N.Y. 1007, Nov. 14-19,1982.

Stephenson, L.D., Smith, A., Hock, V.F., and Rigsbee, J.M., "Containerless Coating Processes for Large Space Structures", *Engineering, Construction, and Operations in Space*, 1988.

"Space Systems Technology. SP-593", Society of Automotive Engineers, Inc. Warrendale, Pennsylvania 15096, Dec. 1984.

Status of Advanced Propulsion for Space-Based Orbital Transfer Vehicle NASA Lewis Research Center, Cleveland, Ohio, 1987.

Van Vliet, R.M., *Passive Temperature Control in the Space Environment*, The MacMillan Co, New York, 1965.

Wie, B., Geller, D., et al., "A New Momentum Management Controller for the Space Station", *AIAA Gudiance, Navigation and Control Conference Part 2*, August 15-17, 1988.